Simultaneous structural and dielectric measurement of ammonia storage materials

By

Jon Robert Hartley

**A thesis submitted to Cardiff University
for the degree of Doctor of Philosophy**

September 2015

Abstract

The principal aims of this thesis are to design, build and experiment with simultaneous measurement systems, designed to measure ammonia adsorption in a wide range of sample materials. These simultaneous measurement systems will integrate dielectric spectroscopy methods with structural analysis techniques in order to obtain a more complete understanding of the dynamic adsorption processes that occur. Some of the new and most promising materials for ammonia storage applications are tested in this thesis in order to understand the possible strengths and weaknesses that these materials have in becoming used in real world applications.

Dielectric spectroscopy in this thesis is achieved by using microwave resonant structures. These devices measure permittivity, dielectric losses and electrical conduction by way of the cavity perturbation technique. Structural analysis is conducted by way of neutron and X-ray diffraction, both of these measurement techniques give insight into the crystal structure of materials. With these two measurement techniques, changes in bulk material properties (measured from the dielectric spectroscopy) can be compared and contrasted with changes in the crystal structure (measured from the diffraction techniques).

The materials tested within the simultaneous measurement systems were alkali earth and transition metal halides. On introducing gaseous ammonia to these materials, the dielectric properties and molecular structure changed. Using the combined information from multiple measurement techniques, a wide range of physical phenomena was able to be observed and analysed. This included assessment of the total amount of ammonia adsorbed, the amount of chemisorbed ammonia to physisorbed ammonia and if the ammoniated material was stable after the ammoniation process. Phase transformations involving coordination geometry were observed, as well as suppression of hole conduction processes due to ammoniation.

Acknowledgements

1 Contents

Nomenclature

DSC   Differential scanning calorimetry

EM   Electromagnetic

IF   Intermediate frequency

MCR   Microwave cavity resonator

MFM   Mass flow meter

MOF   Metal organic framework

MS   Mass spectrometer

ND   Neutron diffraction

NPD   Neutron powder diffraction

PTFE   Polytetrafluoroethylene

RF   Radio frequency

S_{11} Reflection coefficient

S_{21} Transmission coefficient

SMA   Sub miniature A

SNR   Signal to noise ratio

STP   Standard temperature and pressure

TE   Transverse electric

TGA   Thermogravimetric analysis

TM   Transverse magnetic

VNA   Vector network analyser

XRD   X-ray diffraction

1   Introduction

1.1   Scope

In recent years the scientific and industrial community have been working to develop reliable and sustainable energy sources to replace the carbon-rich fuels of today. No more so than in the context of energy storage, which has its main applications within the automotive industry as a replacement for petroleum and diesel energy sources. Also gas is currently one of the main energy storage methods for energy security within the UK. But with the North Sea's fuel reserves dwindling the need for a non-imported energy source is becoming more necessary (EDF energy, 2015). One of these options is hydrogen which can be burnt in the same way as oil and gas fuels. Hydrogen is particularly attractive due to its high energy density of 120 MJ/kg compared to current energy sources like petroleum at 45 MJ/Kg. (Brown et al., 1991) (Zittel et al., 1996). Hydrogen, being the most abundant element in the universe, is also a sustainable fuel source through production methods such as electrolysis. Such processes are not cost effective presently but are likely to become so as they become massively scaled and efficiencies are improved (Turner, 2004). Hydrogen does come with a significant disadvantage, in that it is a gas at room temperature with a volumetric density of 0.08988 g/L (Weast et al., 1983). Therefore, pressurised and liquefied hydrogen storage solutions are needed to approach the volumetric density of current fuel sources (Schlapbach & Züttel, 2001) (Zhou, 2005). But in doing this there are inherent problems with achieving high pressures and low temperatures, and furthermore with the release of hydrogen through the storage medium (Von Ardenne et al., 1990) (Züttel, 2003). One solution is to use ammonia instead of hydrogen. Ammonia is a non-carbon fuel, has 17.8% hydrogen by weight and can be stored using methods comparable to those used for hydrogen storage (schuth et al., 2011) (Klerke et al., 2008).

Ammonia storage techniques have only been recently considered as an alternative to hydrogen storage techniques. Therefore, research into many different forms of ammonia storage is being conducted and the strengths and weaknesses of these possible solutions need to be assessed (Lan et al., 2012), as will be discussed in more detail below. There are a variety of assessment techniques to quantify ammonia storage, such as thermogravimetric analysis (Jones et al., 2013), Raman spectroscopy (Reed & Book, 2011), neutron and X-ray diffraction (Chieux & Bertagnolli, 1984). However these measurement techniques come with some inherent drawbacks. Most notable are the difficulty in performing in-situ analysis, the invasive nature of measurement and the inherent high cost of performing measurements. Microwave spectroscopy methods can solve these experimental issues. Microwave measurement techniques are non-invasive (Choi et al., 2014) , can be used for in-situ analysis (Marand et al., 1992) (Eichelbaum et al., 2012) and can be considerable cheaper than other measurement techniques. Microwave measurement techniques in the context of ammonia storage look at the bulk dielectric properties of a material (Kaatze, 2010). Measuring permittivity and dielectric loss of a material in this way can give insight into chemical changes in a material, such those that occur during ammonia storage methods, owing to the large intrinsic electric dipole moment of the ammonia molecule.

1.2   Thesis overview

This thesis is broken down into five main chapters (after this introduction); each of these will be briefly detailed here.

Chapter 2 – This chapter gives an overview of the measurement techniques used in the project, their general operation, background and theory. This chapter also details the current possibilities of ammonia storage methods that are currently being investigated and focuses in more detail on the specific materials used in this thesis.

Chapter 3 – This chapter describes the design, construction and testing of a microwave cavity resonator for use with powder neutron diffraction measurements, and also a hairpin resonator for use with X-ray diffraction measurements. The specific design considerations needed to develop these integrated measurement systems are discussed in detail. Also explained is the system used to capture the microwave sensor data and the calculations needed to convert them into the dielectric properties.

Chapter 4 – This explains the setup used for simultaneous measurement of dielectric and structural proprieties via microwave cavity resonance and neutron diffraction. It also details the preliminary experiments that have been performed to understand and refine the measurement process. This chapter also discusses the results and analysis of alkali earth halides and transition metal halides obtained by the simultaneous measurement techniques. It concludes by discussing the extraction of the physical properties and describing the dynamic processes of ammonia adsorption of the materials tested.

Chapter 5 – This details the experimental setup used for conducting simultaneous measurement of dielectric and structural proprieties via microwave cavity resonance and X-ray diffraction. It also discusses the results from these experiments and analysis of the features observed. Also, the measurement technique is compared with the measurements taken in chapter 4.

Chapter 6– In this chapter conclusions on the outcomes of the results in chapter 4 and chapter 5 are discussed, as well as future improvements to these experimental setups. A new experimental design is laid out in this chapter, which will provide heating of the sample to allow simultaneos dielectric and structural characterisation during unammonation. The design of the experimental setup is discussed in detail, together with the expected outcomes that the new experimental rig will be able to provide.

1.2.1 Original contributions

- Design and construction of microwave cavity resonance structures that integrates into neutron and X-ray diffraction experimental setups, for use in dynamic and simultaneous measurement of gas flow experiments.

- Measurement of dielectric and structural properties in alkali earth and transition metal halides under ammonia gas flow. Showing changes in material properties as ammoniation occurs and relating dielectric changes in the material with structural changes.

- Performing thermogravimetric and differential scanning calorimetry techniques on the alkali earth and transition metal halides to analyse their ammoniation and unammoniation properties.

- Design of an experimental setup for simultaneous dielectric and structural measurement while being able to heat the sample and cycle the uptake and release of ammonia of the sample.

1.2.2 Publications

Hartley, J., Porch, A. & Jones, M., 2015. A non-invasive microwave method for assessing solid-state ammonia storage. Sensors & Actuators: B. Chemical, 210, pp.726-30.

Hartley, J., Jones, M. & Porch, A., 2015. Simultaneous structural and dielectric measurement of ammonia storage materials. UK Neutron and Muon Science and User Meeting. Hinckley.

Hartley, J., Lees, J. Cuenca, J. & Choi. H., 2014. Assessment of Machine Oil Quality by Microwave Cavity Perturbation Method. International Symposium on Information Technology Convergence. Jeonju.

Hartley, J., Jones, M. & Porch, A., 2013. A Non-Invasive Sensor For Assessing Solid-State Ammonia Storage. H2FC Supergen Researcher Conference. Birmingham.

Imtiaz, A., Hartley, J. Choi, H. & Lees, J., 2014. A High Power High Efficiency Integrated Solid-State Microwave Heating Structure for Portable Diagnostic Healthcare Applications. IEEE Int. Microw. Workshop Series on RF and Wireless Technol. for Biomedical and Healthcare Applications. London.

Jones, M., Hartley, J. David, W. & Porch, A., 2014. Investigating and Understanding Ionic Ammine Materials. 11th Annual NH3 Fuel Conference. Iowa.

Cuenca, J., Choi, H. Hartley, J. & Porch, A., 2014. Microwave Detection of Photodielectric Effects in Antimony Tin Oxide. International Symposium on Information Technology Convergence. Jeonju.

Choi, H., Cuenca, J. Hartley, J. & Porch, A., 2014. Observation of Change in Microwave Properties During Solid to Liquid Phase Transformation of Gallium. International Symposium on Information Technology Convergence. Jeonju.

2 Background

The main areas of work for this thesis come from three distinct fields of research: X-ray and neutron diffraction measurement techniques, where the principles were developed by Bragg (Bragg, 1913), microwave measurement methods which are based on the theoretical work of Maxwell (Maxwell, 1873) and the use of complex coordination structures to store ammonia, based on the work of Werner (Werner, 1913).

2.1 Ammonia storage methods

A typical fuel tank today (50 L) can hold approximately38.5 Kg of petrol or 49.9 Kg of diesel fuel compared to ammonia fuel at 0.038Kg under the same atmospheric conditions (STP) (Air Liquide, 2013). Ammonia is approximately 17.8% hydrogen by weight. Therefore the available energy of the ammonia fuel in a fuel tank compared with conventional fuel sources is approximately 0.047%. To achieve a commercially viable ammonia fuel source its volumetric density must be greatly increased, so that the available energy of an ammonia fuel source can compete with current fuel sources. Ross has detailed the requirements of a hydrogen storage method to adequately compete with current fuel sources (Ross, 2006), the details being:

- Gravimetric energy density: 2 kWh/kg.
- Volumetric energy density: 1.5 kWh/L.
- Hydrogen storage capacity (mass fraction) of 6 wt% (on a system basis).
- Operating temperature: −30 to +50 °C.
- Re-fuelling time <5 min.
- Re-fuelling rate: 1.5 kg H_2/min.
- Recoverable amount of hydrogen: 90%.
- Cycle life: 500 times (requirements for the physical properties of storage material).
- Cost target: US$5/kWh (storage material only, without peripheral components).

There are many possible solutions to storing ammonia, such as in liquid form, under high pressure, in nanoporous materials and in metal hydrides materials. All these methods improve both the gravimetric and volumetric energy density of ammonia storage but are yet to be commercially viable.

2.1.1 Liquid storage

Liquid ammonia is already the primary storage method for transport within the agriculture industry, with 13.2 million metric tons being produced and transported in the U.S per year (Hattenbach, 2006). There are two main methods of achieving liquid ammonia storage; at normal atmosphere pressure and -33°C, or under pressure at 8 bar in stainless steel containers (Lan et al., 2012). Both methods increase the density of ammonia, which can be seen from Figure 2.1, which considers a range of hydrogen-containing materials which are candidates for energy (hydrogen) storage media. Liquid ammonia does have some drawbacks in its application as a fuel. The use of liquid ammonia as an energy storage medium faces considerable challenges, most notably the high coefficient of thermal expansion, high vapour pressure and high reactivity with water and container materials (Thomas & Parks, 2006). Furthermore, ammonia has a high toxicity.
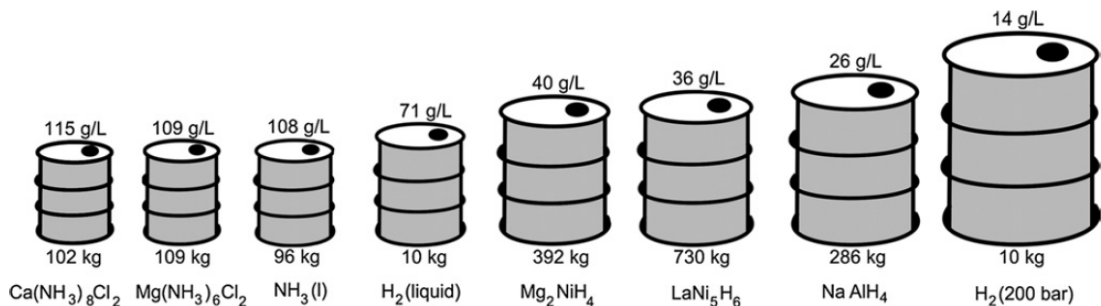
Figure 2.1 – Mass and volume of 10Kg hydrogen stored reversibly by eight different methods, based on the best obtained reversible densities reported in the literature without considering the space or weight of the container (Klerke et al., 2008).

2.1.2 Physisorption

Physisorption (or physical adsorption) is the process of gas molecules binding to solid materials via Van der Waals interactions. An example of the physisorption process is shown in Figure 2.2 for hydrogen gas adsorption, where the amount of adsorption being dependent on the surface area of the material.

Porous materials that have shown to display physisorption properties for use in gas storage include metal organic frameworks (MOF) (Collins & Zhou, 2007), (Thomas, 2009), carbon nanostructures (Darkrim et al., 2002) and zeolites (Langmi et al., 2003). The disadvantages of physisorption, like those for liquid storage techniques, are that most materials need to be maintained at low temperatures (typically <77 K) due to the weak forces involved. Also, the materials in question can experience chemisorption (as described in the next section) instead of physisorption so that the ammonia cannot be released unless high temperatures are applied, which can damage the porous structures.
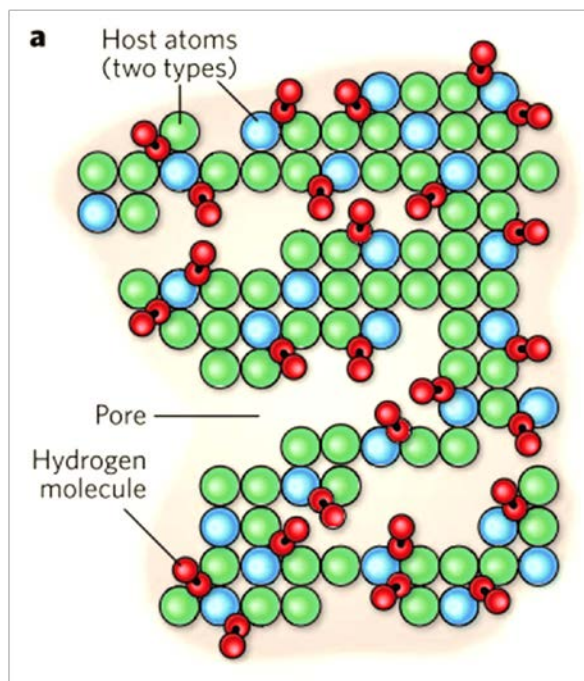
Figure 2.2 – Materials that have high porosity store hydrogen using physisorption, in which the gas molecules accumulate at the surface of the material, but don't react chemically with it (Getty & Schlapbach, 2009).

2.1.3   Chemisorption

Chemisorption, as the name suggests, is the adsorption of species through chemical reaction. This process will result in changes in the materials crystal structure and heat exchange from the reaction, as shown in Figure 2.3 for an example of hydrogen storage. Due to a stronger bonding mechanism compared with that of physisorption, ammonia adsorption[1] as a result of chemisorption can occur at normal atmospheric conditions, so not requiring the need for cooling apparatus for the retention of ammonia.

A wide range of materials exhibit ammonia chemisorption, most notably in the context of ammonia storage, ammonia borane (Peng & Chen, 2008) and metal ammines (Christensen et al., 2005). However due to the stronger bonding involved, the process of unammoniation requires larger amount of energy (in the form of heat) than physisorption and this in turn reduces the efficiency of the system.
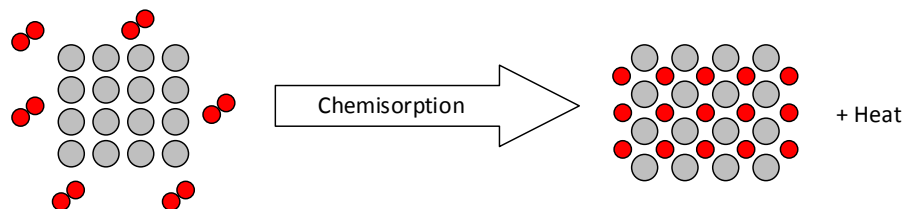
Figure 2.3 – Chemisorption of hydrogen showing changes in materials atomic structure and heat exchange from reaction, which is normally exothermic.

---

[1] Ammonia may not necessarily remain as ammonia when reacted with the host material and may yield other products.

2.2 Halide materials

Halide materials have been identified as potential ammonia storage materials (Christensen et al., 2005). A range of different types of halides are shown in Table 2.1. Alkali halide and rare earth halide have not been identified as efficient ammonia storage materials, but rare earth halides are currently used as dopants in metal hydrides to improve hydrogen kinetics and thermodynamics (Xueping et al., 2007). Alkali earth and transition metal halides have been shown to adsorb and hold ammonia at varying stoichiometric and non-stoichiometric amounts and so ammonia adsorption in these materials will be focused on in this project. Also, these halide materials have been shown to hold ammonia with comparable gravimetric and volumetric hydrogen density to that of other storage methods, such as liquid storage techniques (Klerke et al., 2008). Due to the low cost and ease of manufacture of halide materials, large scale synthesis and production is entirely possible for real world applications (Zhu et al., 2009).

Table 2.1 – Groupings of Halide materials showing some common materials that are used in ammonia storage techniques.

	Alkali metal	Alkali earth metal	Transition metal	Rare Earth metal
Chlorides	LiCl, NaCl, KCl	$MgCl_2$, $CaCl_2$, $SrCl_2$	$CoCl_2$, $NiCl_2$, $CuCl_2$	$LaCl_3$, $CeCl_3$
Bromides	LiBr, NaBr, KBr	$MgBr_2$, $CaBr_2$, $SrBr_2$	$CoBr_2$, $NiBr_2$, $CuBr_2$	$LaBr_3$, $CeBr_3$
Iodides	LiI, NaI, KI	MgI_2, CaI_2, SrI_2	CoI_2, NiI_2, CuI	LaI_3, CeI_3

2.2.1   Structure and properties

Most of the halides experimentally evaluated in this thesis form ionic structure comprising M^{2+} cation and two X^- anions. Due to the ionic bonding, these halide materials are solids at room temperatures. There can be a wide range of geometries for these anhydrous materials (tetrahedral, octahedral, cubic, etc). An octahedral formation (Dorrepaal, 1984) is shown for the example of $MgCl_2$ in Figure 2.4, where a chain structure is formed in the material.

Ammonia can bond to the metal cation by L-type ligand bonding (donates two electrons) to create a dipolar bond. These electron pairs occupy hybrid orbitals of the metal cation or can bond via electrostatic interactions. The size of unit cell tends to increase to incorporate the introduction of ammonia into the crystal structure. Therefore this bonding process can cause a wide range of new crystal formations to occur and result in liquid phase transitions (Poonia & Bajaj, 1979). An example of the differences in structure is shown in Figure 2.5 for a model of $MgCl_2$ as different amounts of ammonia are adsorbed into the material. Similar structures for Mg based halides have been observed (Leineweber et al., 1999).
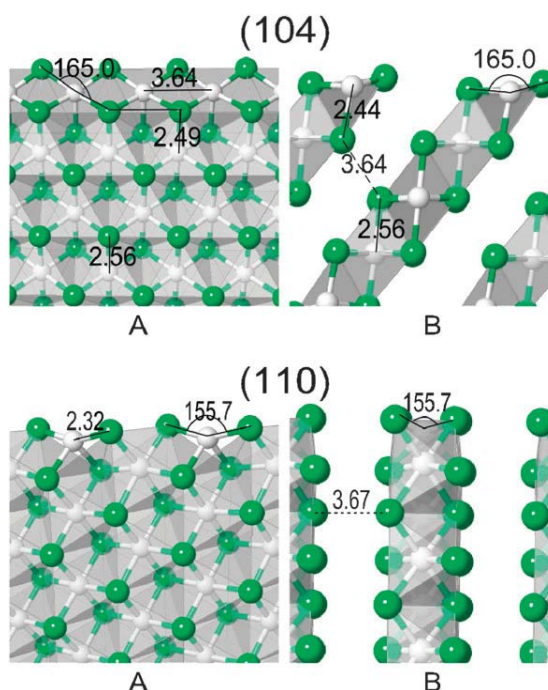
Figure 2.4 – Orthographic view of the structures of the optimised (104) and (110) α-MgCl₂ surfaces (A) perpendicular to the ab plane (B) parallel to ab plane (Credendino et al., 2009).
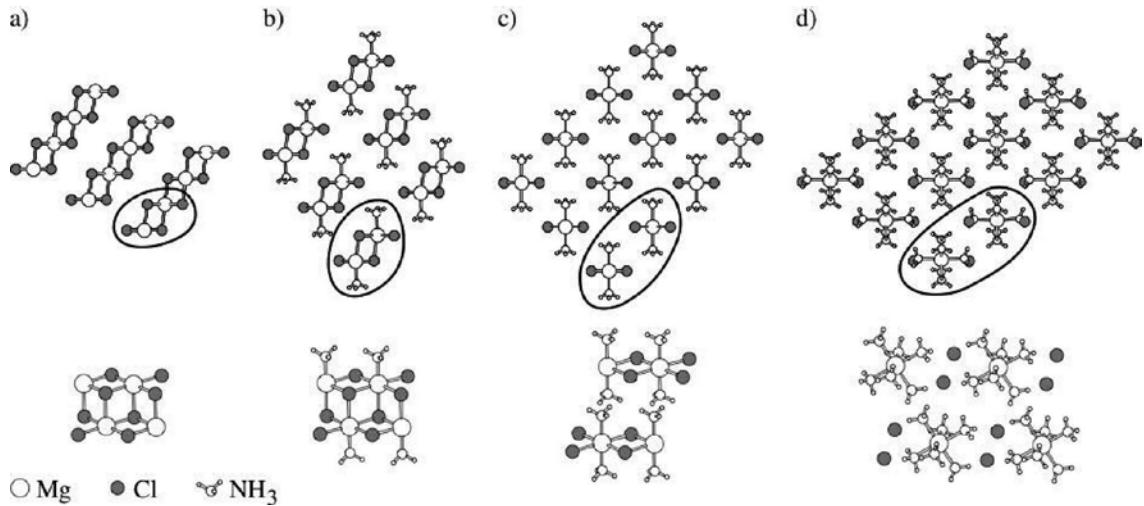
Figure 2.5 – Optimised structures found using density functional theory for (a) MgCl$_2$ (b) Mg(NH$_3$)Cl$_2$ (c) Mg(NH$_3$)$_2$Cl$_2$ (d) Mg(NH$_3$)$_6$Cl$_2$, viewed along the chains that continue infinitely in and out of the picture. Four formula units are shown from the side, corresponding to the highlighted fragments in the end view (Sørensen et al., 2008).

The coordination number can vary from one, as is the case shown in Figure 2.5 (a) to anything up to a coordination of twelve (cuboctahedron) (Milburn et al., 1998). However, certain materials will favour certain coordination geometries. For example, in Mg(NH$_3$)$_x$Cl$_2$ the maximum coordination from Figure 2.5 (d) is shown to be six whilst in Ca(NH$_3$)$_x$Cl$_2$ the maximum coordination is identified to be eight (Westman et al., 1981). This is because calcium has a larger atomic radius and thus has more space for ammonia to bind to it.

2.2.2 Ammoniation process

Due to the various different coordination complexes that can be formed from ammonia adsorption in halides, the kinetics of adsorption can vary from material to material. This can be seen from Figure 2.6(left), where both the amount of ammonia adsorbed and the rate of adsorption changes for different halide materials. The adsorption of ammonia has shown to be a sequential ligation process (Milburn et al., 1998). This means the material tends to form lower order complexes first and then sequentially forms the higher order complexes. For MgCl$_2$, it can be seen from Figure 2.5 that not all coordination complexes are possible and therefore the adsorption kinetics from Mg(NH$_3$)Cl$_2$ to Mg(NH$_3$)$_2$Cl$_2$ will be different to those from Mg(NH$_3$)$_2$Cl$_2$ to Mg(NH$_3$)$_6$Cl$_2$.
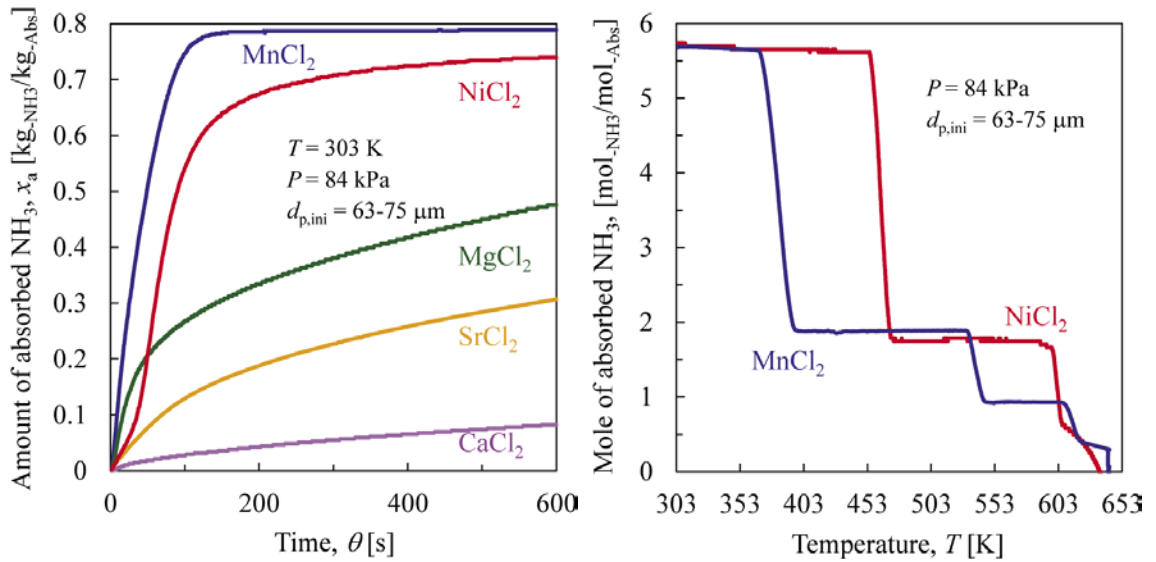
Figure 2.6 – Time dependence of the amount of adsorbed NH₃ per unit weight of various metal chlorides at 303 K and 84 KPa (left) and change in amount of adsorbed NH₃ for MnCl₂ and NiCl₂ with increasing temperature at a heating rate of 10 K/min (right) (Kubota et al., 2014).

This formation of coordination complexes during adsorption can be seen in the reverse process on thermal desorption shown in Figure 2.6(right). The higher order complexes are thermally liberated first and lower order complexes are sequentially desorbed (Jones et al., 2013).

The other factors that determine the adsorption process are the temperature and pressure of the material. Temperature increases will increase the bond dissociation in the ammonia adsorption process. Increased pressure, on the other hand, tends to increase the amount of ammonia adsorbed (Lui & Aika, 2004), up until the point where the pressure increase causes the same bond dissociation effects as for temperature. The main bulk of the ammonia adsorption process in halide materials comes from chemisorption. However halide materials can also exhibit physisorption of ammonia in the form of surface adsorption (Ammitzbóll et al., 2013). As with other physisorption materials, the binding energies of surface adsorption tend to be lower[1] than that of the coordinated ammonia and will be deadsorbed before the coordinated ammonia.

---

[1] In some cases chemisorbed ammonia with low enthalpies will be released prior to physisorbed ammonia.

2.3 Neutron and X-ray diffraction

X-ray diffraction (XRD) and neutron diffraction (ND) are two of the most effective techniques in the crystallographic characterisation of materials. Due to the small wavelengths (nm) of X-rays and neutrons, these waves can interact with atomic planes and so can give insight into the crystal structure of molecules.

2.3.1 Principles of diffraction techniques

In a crystal, the atoms are located at set distances (d) from one another to produce a three dimensional structure; for example, cubic, orthorhombic and hexagonal. When an incident neutron or X-ray beam is applied to this structure, with its wavelength (λ) comparable to the atomic spacing of crystal, the wave will reflect at an angle (θ) and cause constructive interference between all the outgoing waves (Siva, 2011). The condition where constructive interference occurs is known as the Bragg condition and is defined by Equation 2.1.

$$n\lambda = 2dsin(\theta)$$ **Equation 2.1**
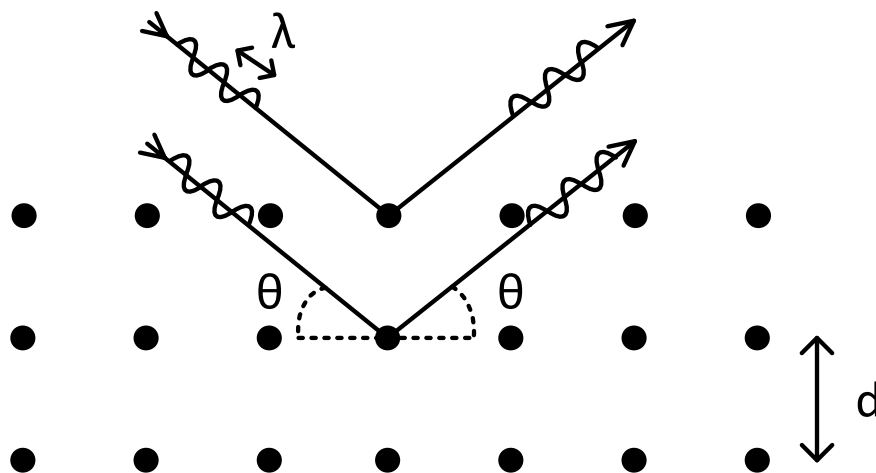
Figure 2.7 – Two dimensional representation of Bragg reflections from a crystal structure, showing constructive interference from reflections caused by the crystal's fixed interatomic distances (d).
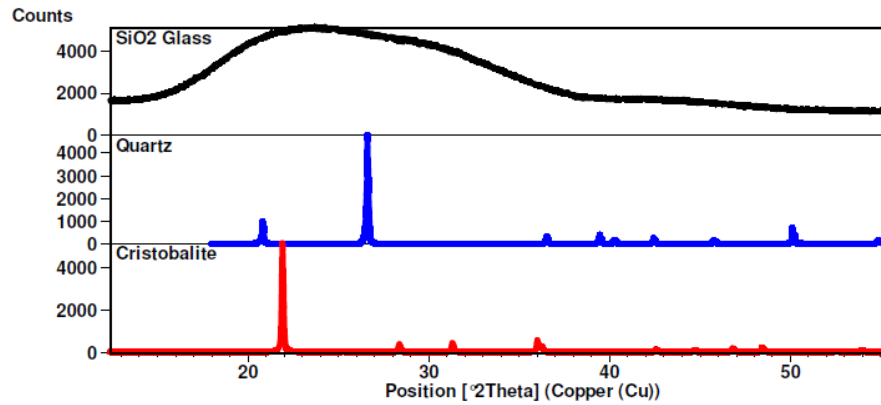
Figure 2.8 –The X-ray diffraction patterns from 3 different forms of SiO$_2$, showing difference in Bragg peaks due to changes in crystallographic structure (Speakman, 2014).

The d-spacings of a crystal structure can be determined by either fixing the wavelength and rotating the sample through all possible angles, or by fixing the position of the sample with a range of different wavelengths. The constructive interference caused by the Bragg condition will cause an increase of signal strength at that particular angle or wavelength. These are known as Bragg peaks and can clearly show the atomic spacings within a crystal structure. An example of this is shown in Figure 2.8, where the diffraction patterns of SiO$_2$ in three different forms are shown. Quartz and cristobalite show different Bragg peak positions from the different crystal structures, whereas glass does not show any well-defined Bragg peaks due to its intermediate crystalline state and lack of long range ordering (causing a continuous spread of varying atomic spacings).

2.3.2 Powder diffraction

In most cases, producing a single crystal large enough to produce good diffraction data is impractical, especially in the case of neutron diffraction (ND). Thus the use of powdered samples is used for many diffraction measurements as in this thesis. In a polycrystalline material all possible orientations of the crystal are exposed to incident signal. This will give diffraction patterns that are invariant to the azimuthal angle and give the so called Deybe-Scherrer rings associated with powder diffraction at a constant angle of incidence θ, as shown in Figure 2.9. Due to the varying orientations of crystals, all Bragg reflections from all of the Miller indices of the crystal planes will be present at any one time. This is seen from the NaCl sample in Figure 2.9, where there are multiple Deybe-Scherer rings. From these multiple diffraction angles make it possible to determine valid Miller indices h, k and l (Langford & Louert, 1996) and by refinement methods to determine the crystal's unit cell (Rietveld, 1967), (Rietveld, 1969).
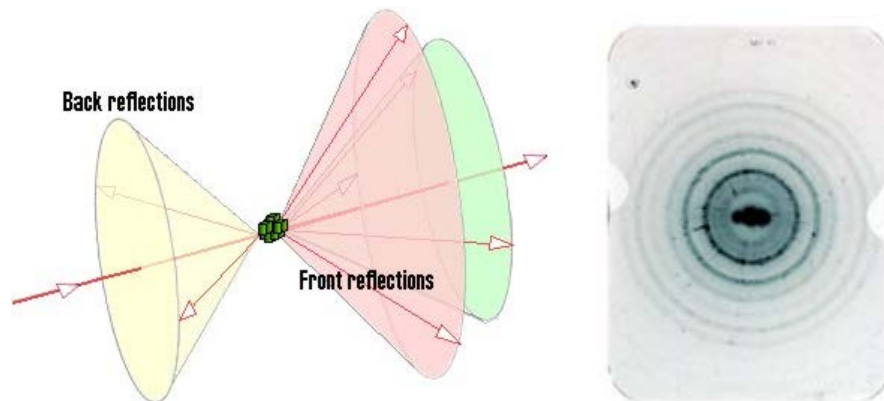
Figure 2.9 – Representation of diffraction patterns from randomly orientated single crystals (University of Liverpool, 2000) (left) and of diffraction patterns of NaCl (Leybold, 2014) (right).

2.3.3 Differences between X–ray and neutron diffraction

XRD and ND have similar wavelengths, which are comparable to interatomic distances and are both used as key tools in crystallography. The diffraction principles explained in section 2.3.1 apply to both XRD and ND. However there are some differences between XRD and ND techniques that can make one technique more preferable in certain applications. Firstly X-rays are electromagnetic waves which interact with the orbital electrons of a material. In contrast, neutrons are particle waves which interact with the nucleus of the atom by the strong nuclear force (Siva, 2011). These differences in interactions are illustrated in Figure 2.10. The difference in scattering interaction produces vastly different scattering lengths and attenuation coefficients in X-rays and neutrons, as seen in Figure 2.11. This is due to the neutron scattering lengths depending on nuclear mass and the strong interaction (the theory of quantum chromodynamics), whereas X-ray scattering lengths depend on the number of electrons and the electromagnetic interaction (the theory of quantum electrodynamics) (Fischer et al., 2006).
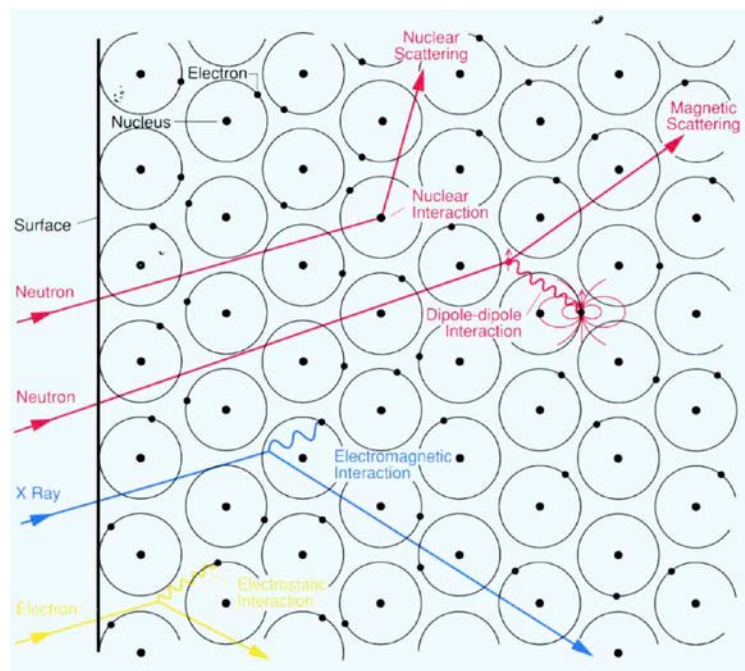
Figure 2.10 – Scattering interactions for beams of neutrons, X-rays and electrons, showing the different mechanisms by which they interact with materials (Pynn, 1990).

This is why the X-ray scattering length increases with the increasing amount of electrons in the material (i.e. the atomic number), whereas neutron scattering length does not.

An advantage of X-ray methods is the availability of large photon fluxes, as much as 10^5 times greater than those available in equivalent neutron experiments (Neilson et al., 2001).This gives XRD measurements the ability to collect greater amounts of data owing to the much larger signal to noise ratio than for ND techniques. This gives significant advantages in situations where fast data capture is required or low amounts of material are available. A disadvantage of X-ray methods is that X-rays are highly attenuating, resulting in penetration depths of the order of microns to millimetres, compared to neutrons where penetration depths are typically of the order of centimetres. This can cause problems when there is unwanted material in the X-ray path, for example due to furnace walls or sample holders, which can cause significant X-ray signal degradation.   Because of the different attenuation coefficients for the two measurement techniques, some materials are more suited for X-ray diffraction techniques than ND and vice versa.
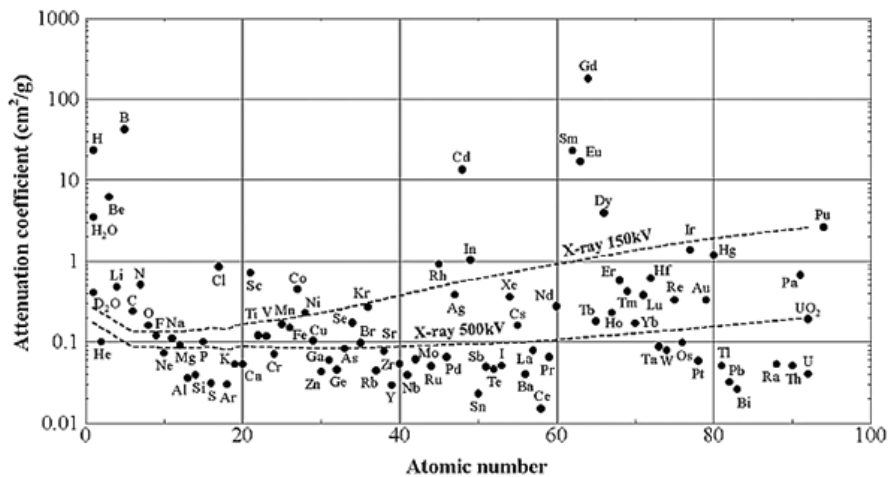
Figure 2.11 – Neutron and X-Ray Mass Attenuation Coefficients for the Elements (S.H.I Examination & Inspection LTD, 2014)

2.4 Microwave measurement theory

Similar to neutron and X-ray measurement techniques, microwaves can be used to non-invasively measure intrinsic properties of materials. Due to the longer wavelengths (order of cm) compared to X-rays and neutrons (order of nm), microwaves are more suited to measure bulk properties of a material rather than atomic and molecular properties.

2.4.1 Dielectric fundamentals

A material's dielectric property can be defined by its permittivity (ε). This is a value assigned to a material's ability to produce a displacement electric field that opposes the applied (external) electric field, also known as its polarisation (Fröhlich , 1948).   The polarisation vector $\underline{P}$ (defined as the net dipole moment per unit volume, in units of C/m^2) is then expressed in terms of the permittivity via $\underline{P} = (\varepsilon - 1)\varepsilon_0\underline{E}$, where ε_0 is the permittivity of free space and $\underline{E}$ is the internal electric field that results inside the material. In metals there are a large number of free electrons that become displaced to form a large polarisation of the material, whilst the internal $\underline{E}$ is reduced to zero by the screening of the free electrons. In a metal, we see that the permittivity is effectively infinite. In complete contrast, a vacuum has no opposition to an electric field (i.e. no material to polarise) and so its permittivity is one.
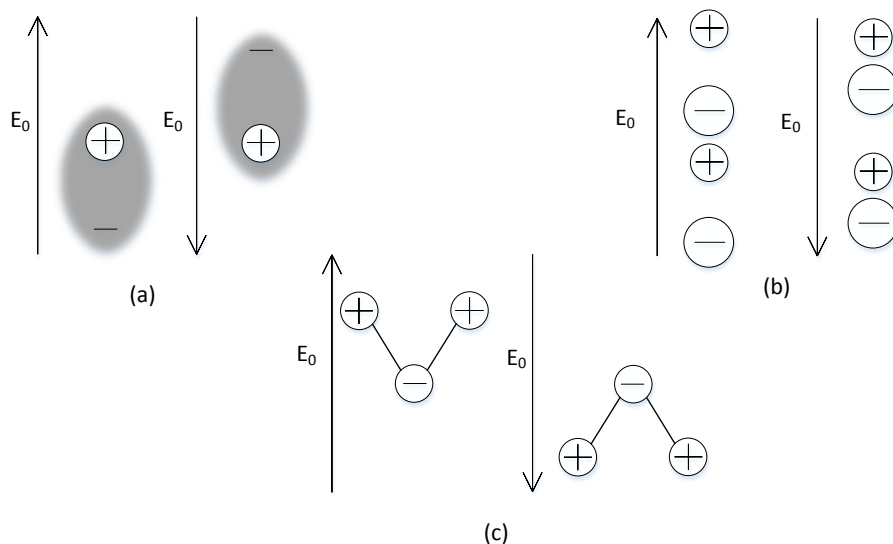
Figure 2.12 – Mechanisms that effect permittivity of materials, showing the polarising effect with different electric field direction for electronic (a), atomic (b) and orientational polarisation (c).

All other materials have permittivity values in the range between one to infinity, and are generally classed as dielectric materials. At ac frequencies the permittivity can be considered to be a complex number $\varepsilon = \varepsilon_1 - j\varepsilon_2$. The real part ε_1 is associated with stored energy (via the polarisation), whilst the imaginary part ε_2 is associated with energy loss (i.e. a phase difference between the polarisation and the internal electric field). Polar materials such as water and ammonia have frequency-dependent values of both real and imaginary parts of the permittivity, which are both large at the microwave frequencies (1-10 GHz) studied in this thesis. This large interaction with microwave fields, quantified via the large and complex permittivity, is the reason why microwave methods are so successful for studying the loading of polar molecules such as ammonia in solids. Three[1] types of polarisation contribute to a materials permittivity. Firstly, electronic polarisation, shown in Figure 2.12(a), is the distortion of the atomic orbitals to create a partial charge separation. This phenomenon generally has a small contribution to permittivity, in the range of less than two, and occurs in all materials. Secondly, atomic polarisation occurs in ionic structures shown in Figure 2.12(b), its mechanism is due to the expansion and contraction of ionic bonds. This creates varying atomic distances between the atoms nearest neighbours and the resulting varying dipole moments create an overall polarisation.

Atomic polarisation is a stronger polarising mechanism than electronic polarisation and materials which exhibit this generally have permittivities approximately less than ten. The final form of polarisation is orientational. This is the strongest of the three types of polarisation with permittivities greater than ten. Orientational polarisation occurs in molecules that have a permanent dipole moment and rotational freedom, so that when an electric field is applied the dipoles can orientate themselves to oppose the external field, as shown in Figure 2.12(c).

---

[1] Ferroelectricity is another form of polarisation; however it is intrinsic to material structure (has a bulk permeant dipole moment) and not induced by electric field.

2.4.2   Dielectric properties of ammonia

Ammonia is a polar molecule, like water, and its dielectric properties are dominated by its orientational polarisation (Billaud & Demortler, 1975). With the dipole moment of ammonia and deuterated ammonia being 1.47D with a 1.484D respectively (Halevi et al., 1967). The orientational polarisation mechanism of ammonia is shown in Figure 2.13. The diagram shows that the molecule takes time to orientate itself to an alternating electric field, causing a lag between the change in field (E_0) and the polarisation (P). This is known as dielectric relaxation and liquid ammonia at -50°C has a dielectric relaxation of 1.5 ps (Fish et al., 1958).

Depending on the frequency of the applied electric field, the dielectric relaxation will have varying effect on the dielectric properties of the material. The extent of this effect is shown in Figure 2.14 and the complex permittivity follows a Debye relation with frequency (Sihvola, 1999). At the frequencies used in this thesis (around 2.45 Ghz) the dielectric properties of the ammonia molecule are very close to the static dielectric properties. However the dielectric relaxation of the ammonia molecule can be altered, i.e the molecule can take a longer or shorter time to orientate itself and in doing so this will change the dielectric properties of ammonia. In the case of liquid ammonia, the ammonia molecules are hydrogen bonded to each other and the strength of this hydrogen bond will determine the dielectric relaxation.
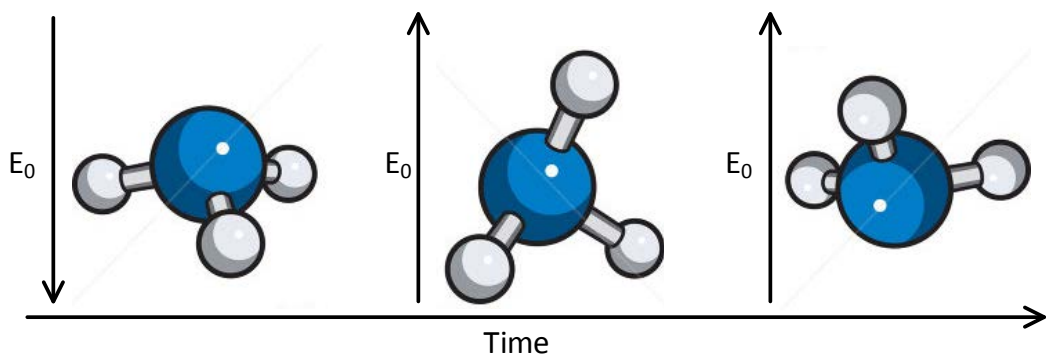
Figure 2.13 **– The orientational polarisation of ammonia molecules under an alternating electric field showing the effect of dielectric relaxation.**

As shown in Figure 2.14 the temperature, and by extension pressure, will affect the strength of the hydrogen bond and therefore change the dielectric properties of the material (Mantas, 1999). This change in dielectric properties is most significantly seen in phase changes in the ammonia where bonding mechanisms drastically change.

Assuming now ammonia interactions with other materials, various different types of bonding mechanisms at various different bonding strengths of the ammonia to a host material can exist. This means the dielectric relaxation of the ammonia molecule can vary significantly for different ammonia related compounds (Jonscher, 1992). This could be anything from ammonia bonded via weak van der Walls forces and having a dielectric relaxation close to that of gaseous ammonia, to ammonia tightly bonded in a crystal lattice, therefore not being able to rotate and thus removing the dielectric effect from orientational polarisation.
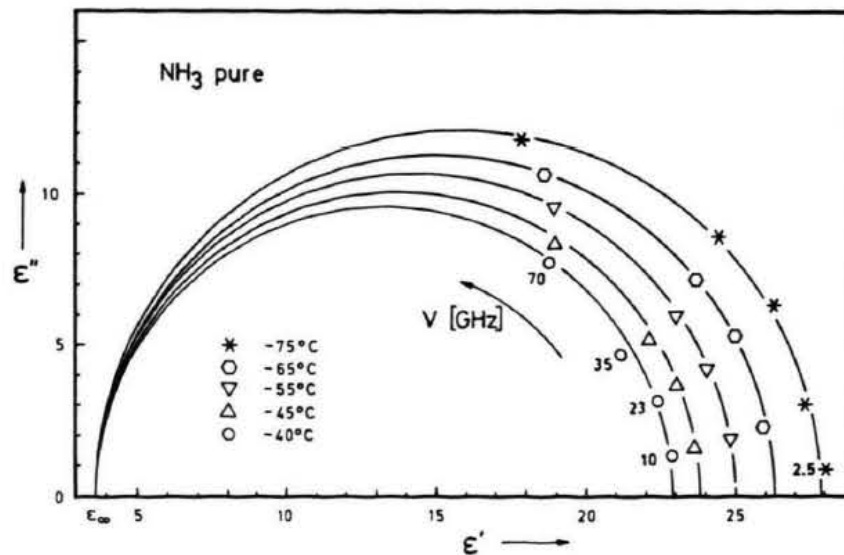
Figure 2.14 – **Cole-Cole plot for liquid ammonia showing dielectric properties under a range of temperatures (Breitschwerdt & Schmidt, 1970).**

2.4.3 Microwave cavity resonator model

A microwave cavity resonator (MCR) can be represented as a RLC circuit, as shown in Figure 2.15. The resistive element represents the ohmic losses from the microwave cavity walls. The inductive and capacitive elements represent the potential energy storage of the electric and magnetic fields, respectively. Resonance occurs when both reactive capacitive (X_c) and inductive elements (X_L) are equal, as shown Equation 2.2. Therefore, the resonance frequency (f) of a cavity is determined by Equation 2.3.

$$X_c = \frac{1}{2\pi f C} \qquad X_l = 2\pi f L$$

Equation 2.2

$$f = \frac{1}{2\pi\sqrt{LC}}$$

Equation 2.3

In the case of microwave cavities the (L) and (C) components are fixed by the dimensions of the cavity. The RLC circuit of a MCR can be represented as a complex impedance (Z). The electromagnetic fields within the cavity structure can be excited via capacitive or inductive methods. Figure 2.16 shows an inductively coupled resonator model where (m_1) and (m_2) are the mutual inductances of the two coupled ports and (Z_0) is the impedance of the transmission line to the cavity (usually 50 Ω). This MCR model can be mathematically described via an S parameter scattering matrix $\begin{bmatrix} S_{11} & S_{12} \\ S_{21} & S_{22} \end{bmatrix}$. A more detailed description showing equivalent circuit model is shown by Kajifez (Kajifez et al., 1999).
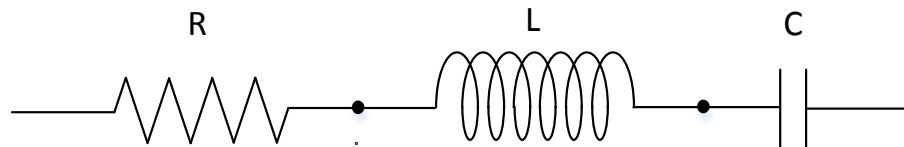
Figure 2.15 – Resistive, capacitive and inductive elements that compose a resonant circuit.
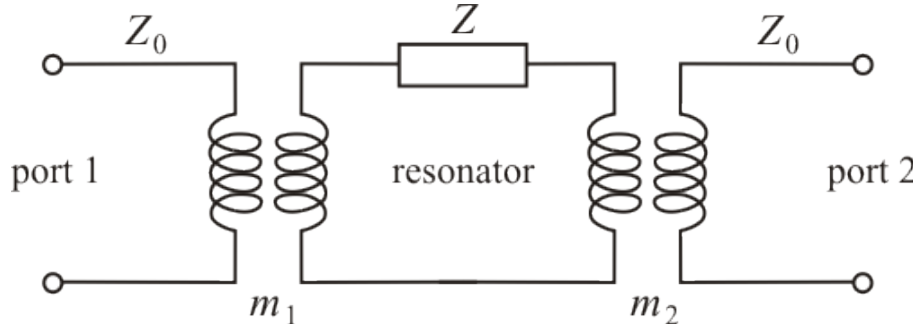
Figure 2.16 – Two port microwave cavity resonator model showing inductive coupling.

$$S_{21} = \frac{2\sqrt{g_1 g_2}}{g_1 + g_2 + 1 + 2jQ_0 \left(\frac{\omega - \omega_0}{\omega_0}\right)}$$

Equation 2.4

$$|S_{21}|^2 = \frac{4g_1 g_2}{(g1 + g2 + 1)^2 + 4Q_0^2 \left(\frac{\omega - \omega_0}{\omega_0}\right)^2}$$

Equation 2.5

In this thesis we focus on transmission resonant structures and therefore use S_{21}[1] to determine resonant properties. Derived from a two port network representation of Figure 2.16, (full derivation shown in appendix 8.1.1) the transmission coefficient for a microwave cavity resonator is shown in Equation 2.4 and the power transmission coefficient in Equation 2.5, where (ω) is the excitation frequency and (ω_0) is the frequency of resonance. Therefore at resonance, S_{21} will be at a maximum and limited only by the coupling coefficients (g_1) and (g_2), which are shown in Equation 2.6 and Equation 2.7. Equation 2.5 also shows that the power transmission coefficient will follow a Lorentzian function. The unloaded Q factor (Q_0) will determine the shape of this Lorentzian function as shown in Figure 2.17.

$$g_1 = \frac{\omega^2 m_1^2}{Z_0 R} = \frac{\omega m_1^2 Q_0}{L}$$

Equation 2.6

$$g_2 = \frac{\omega^2 m_2^2}{Z_0 R} = \frac{\omega m_2^2 Q_0}{L}$$

Equation 2.7

---

[1] Assuming port 1 and port 2 are symmetrical then S_{21} = S_{12} and measurement can be performed from either transmission method.
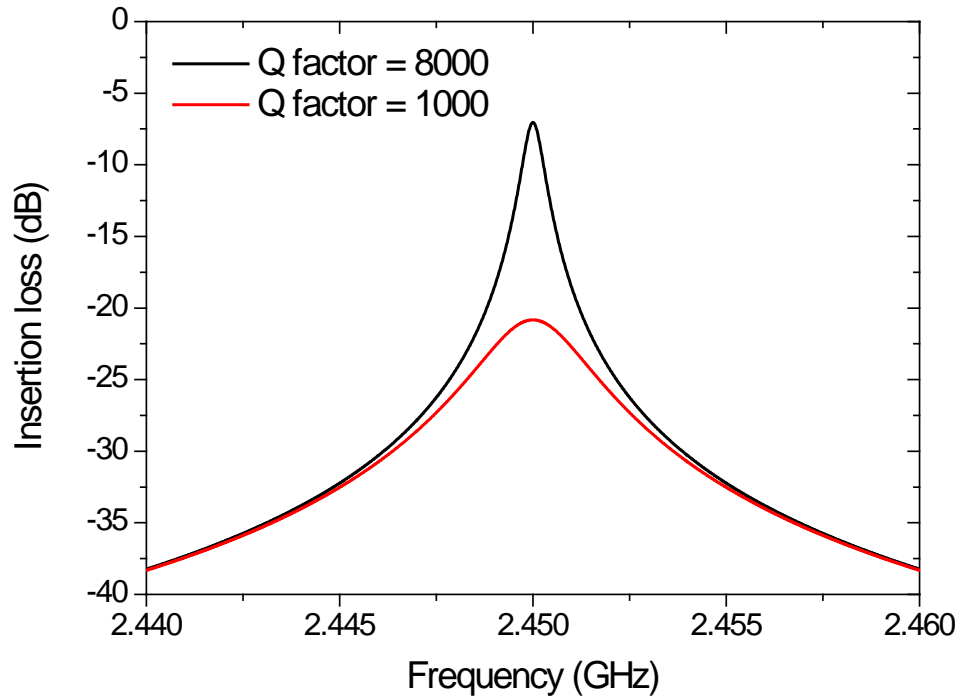
Figure 2.17 – Effect of Q factor on Lorentzian peak shape of resonance curve modelled from Equation 2.5.

2.4.4 Microwave perturbations

As discussed in section 2.4.3, the resonant frequency of a microwave is determined by its dimensions. However, the resonant frequency is also dependent on the permittivity (and permeability, if magnetic materials are present) of the medium contained inside the cavity. Changing this medium will cause a perturbation in stored electric and magnetic energy and thus change the resonant frequency of the cavity. This perturbation is caused by the change in permittivity ($\Delta\varepsilon_r$) and permeability ($\Delta\mu_r$) and is derived from Maxwell's equations, shown in Equation 2.8 (Waldron & Inst, 1960), which is known as the cavity perturbation equation.

In MCR measurements, we assume that changes in the permittivity $(\Delta\varepsilon_r)$ and permeability $(\Delta\mu_r)$ are small. Then we can approximate the perturbed fields (E), (H) from the original fields (E_0), (H_0) within the cavity (Pozar, 1998). This gives a perturbation equation as shown in Equation 2.9, where (V_s) and (V_c) are the volumes of the sample and cavity, respectively.

$$\frac{\Delta\omega}{\omega_0} = \frac{\int_{V_S}(\Delta\varepsilon_r E \times E_0 + \Delta\mu_r H \times H_0)dv}{\int_{V_C}(\varepsilon_r E \times E_0 + \mu_r H \times H_0)dv} \qquad \text{Equation 2.8}$$

$$\frac{\Delta\omega}{\omega_0} = \frac{\int_{V_S}(\Delta\varepsilon_r E_0^2 + \Delta\mu_r H_0^2)dv}{\int_{V_C}(\varepsilon_r E_0^2 + \mu_r H_0^2)dv} \qquad \text{Equation 2.9}$$

As noted in section 2.4.3, at resonance the energy stored in the (E) and (H) fields are equal so the terms in the denominator of the cavity perturbation equation are equal. In the measurements presented in this thesis we focus on the permittivity of materials. Since samples are non-magnetic and are placed in an applied electric field, this leads to further simplifications. Where (Q_s) and (Q_0) denote the cavity Q factor with and without the sample, respectively, defined to be the resonant frequency divided by the half power (3 dB) bandwidth, which we denote *B*.

$$\frac{\Delta\omega}{\omega_0} = \frac{\int_{V_S}\Delta\varepsilon_r(E_0^2)dv}{2\int_{V_C}\varepsilon_r(E_0^2)dv} \qquad \text{Equation 2.10}$$

$$\frac{\Delta\omega}{\omega_0} = -\frac{f_s - f_0}{f_s} + \frac{j}{2}\left(\frac{1}{Q_s} - \frac{1}{Q_0}\right) \qquad \text{Equation 2.11}$$

The complex frequency (ω) can be separated into its real and imaginary parts shown in Equation 2.11 (Lin et al., 2005). Similarly the complex permittivity (ε_r) can be separated into its complex parts of (ε_1) and (ε_2). Therefore from Equation 2.10 and Equation 2.11, assuming that the electric field within the sample is the same as the applied field (true, for example, for the electric field applied parallel to the axis of a cylindrical sample), we can derive the perturbations in the resonant frequency and bandwidth[1] in terms of the complex permittivity, shown in Equation 2.12 and Equation 2.13. More details relating to the microwave cavity used in this experiment, and its application to perturbation measurements for complex permittivity measurements, are discussed in Chapter 3.

$$-\frac{f_s - f_0}{f_0} = \frac{(\varepsilon_1 - 1)V_s}{2V_c}$$ **Equation 2.12**

$$\frac{B_s - B_0}{f_0} = \frac{\varepsilon_2 V_s}{V_c}$$ **Equation 2.13**

---

[1] Bandwidth is derived from equation Q=f/b

2.5   Thermal analytical techniques

Thermal analysis can broadly be defined by observing a change in a material property as a function of temperature (Hatakeyama & Quinn, 1999). Many different techniques have been developed over the years in the field of thermal analysis in order to measure various physical processes. Some of the most common measurement techniques are shown in Table 2.2. These thermal analytical techniques have been used in a wide range of fields such as biology, medicine, pharmaceuticals, organic and inorganic chemistry (Giron, 1994) (Brown, 2001). In this project Thermogravimetric Analysis (TGA) and Differential Scanning Calorimetry (DSC) are used to measure the ammoniation and unammoniation processes in halide materials samples, as discussed in section 2.1.3.

Table 2.2 – Common thermal analytical techniques and the parameters measured (Stodghill, 2010), (Wendlandt & Gallagher, 1981).

Technique	Abbreviation	Parameter measured
Thermogravimetric analysis	TGA	Mass
Differential scanning calorimetry	DSC	Enthalpy
Differential thermal analysis	DTA	Temperature difference
Thermomechanical analysis	TMA	Deformation
Dynamic mechanical analysis	DMA	Deformation
Evolved gas analysis	EGA	Thermal conductivity
Thermo-optical analysis	TOA	Light emission

2.5.1   Thermogravimetric analysis

TGA measures the weight of a sample as a function of temperature, which is traditionally

achieved by use of a thermobalance. The measurement process can provide information about

physical and chemical phenomena, such as second order transitions, vaporization, sublimation,

adsorption, adsorption, decomposition and solid state reactions (Coats & Redfern, 1963)

(Horowitz & Metzger, 1963). TGA techniques are regularly combined with other thermal

measurements such as DSC to obtain a complete understanding of the physicochemical

processes involved.

Typical traces for TGA and DSC measurements are shown in Figure 2.18 for different

physicochemical processes. A TGA curve is normally plotted with the mass change expressed

as a percentage change with respect to the temperature or time on the horizontal axis. An

example of a TGA plot is shown in Figure 2.19, showing a one stage reaction process of the

decomposition of carbon from a chemically activated fibre (Yue et al., 2006).
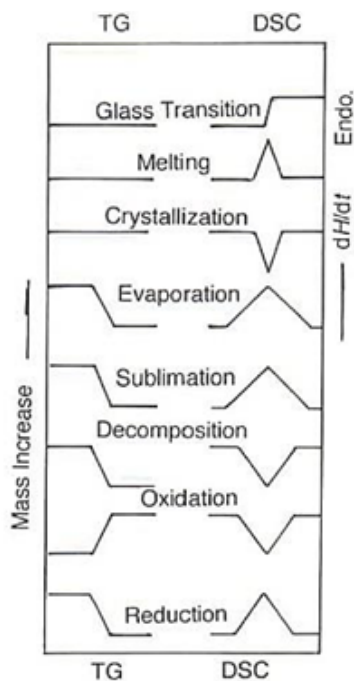
Figure 2.18 – Comparison of the schematic TGA and DSC curves recorded for a variety of physicochemical processes (Hatakeyama & Quinn, 1999).
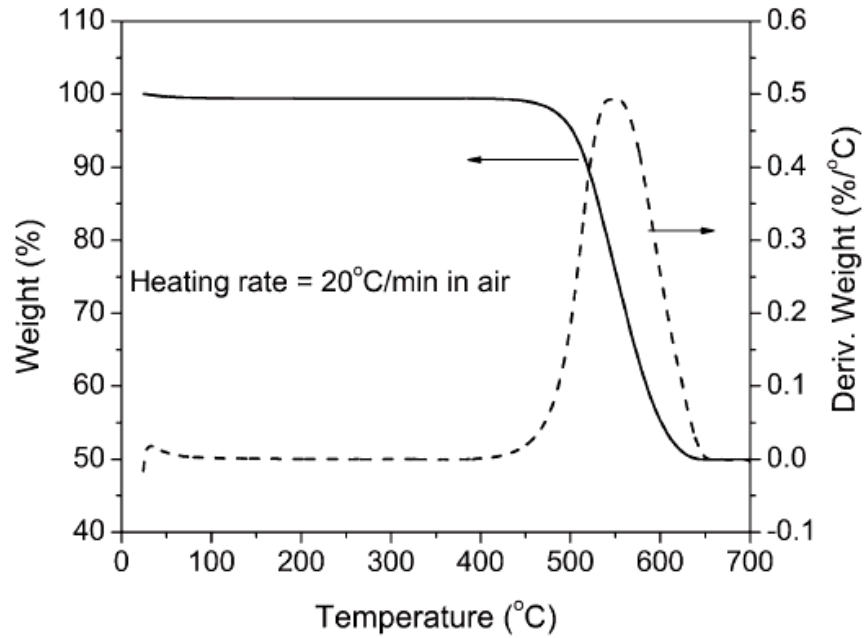
Figure 2.19 – TGA analysis of chemically activated fibre in air (Yue et al., 2006).

The kinetics of the reaction can vary greatly with varying sample mass and temperature profiles. This can result in ambiguous comparison between different TGA traces conducted under different experimental conditions, most notably with endothermic and exothermic reactions, where an increase in heating rate or sample mass will cause a greater temperature difference between the sample and furnace. Similarly, the heating rate and sample mass will determine the uniformity of temperature across the sample and this will affect the rate at which mass loss and gain occurs. Physicochemical processes measured by TGA tend to occur at specific temperatures. However, as with Figure 2.19, these transitions occur over a temperature range, due to the finite heating rate and sample mass issues discussed.

2.5.2 Differential scanning calorimetry

DSC instrumentation comes in two major forms, power compensation DSC and heat flux DSC. Heat Flux DSC techniques are applied in this project and therefore will be discussed in more detail. DSC works by comparing the difference in thermal properties between a sample and a reference. A generalized system diagram is shown in Figure 2.20, where one endeavors to maintain the sample and reference at the same experimental conditions.

The temperatures of the sample and reference are measured by thermocouples under a controlled heating rate. The temperature difference between these thermocouples measures the heat flow rate and this measurement can indicate temperature dependent properties in the sample (Hohne et al., 2003). However, the thermocouples will most often measure a voltage which is related to the true heat flow rate. Calibration is therefore very important for DSC to link heat flow and measured voltage via an instrument calibration constant (Schubnell, 2000). Furthermore any differences in voltages between the two thermocouples with an empty sample condition will also be needed to be calibrated out.
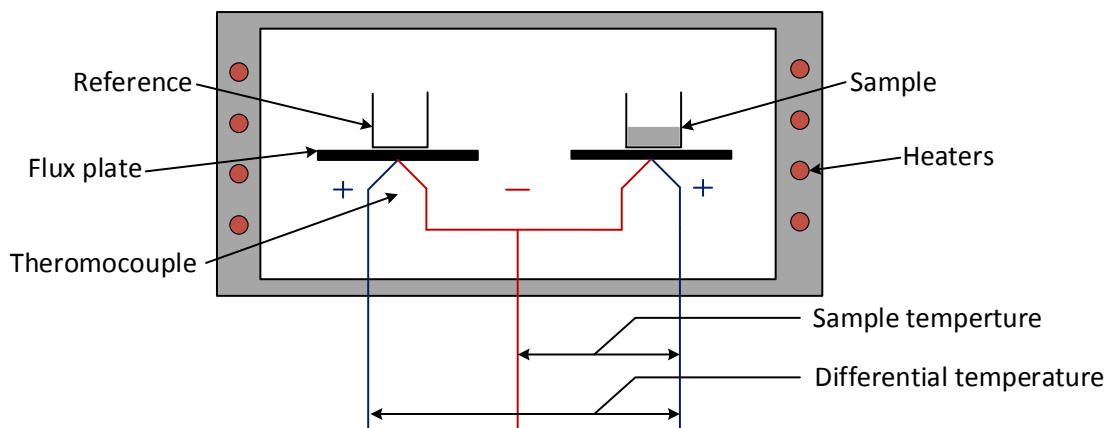
Figure 2.20 –Typical experimental setup of a heat flux DSC showing individual components.
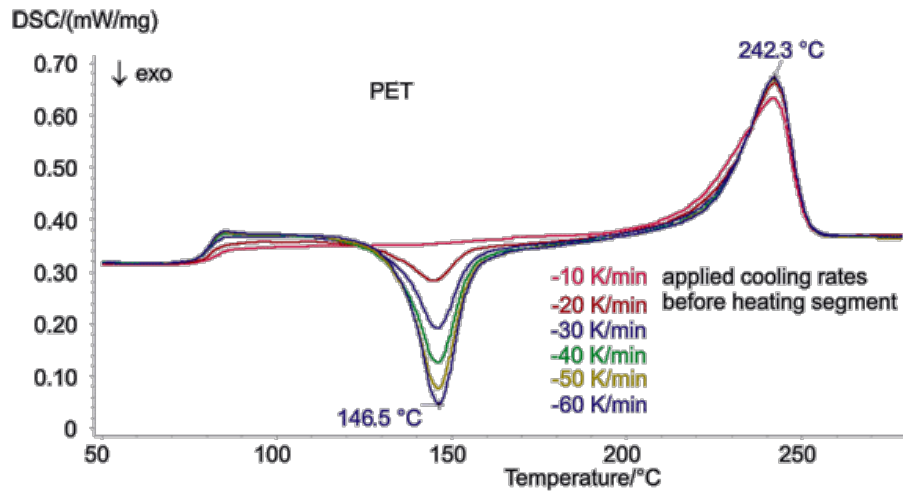
Figure 2.21 – DSC experiments showing amorphous polyethylene terephthalate recrystallization (146°C) and melting (242°C) (NETZSCH Group, 2014).

The difference in heat flow between the sample and reference can be used to measure various endothermic and exothermic processes. Figure 2.21 shows the most common form of thermal changes observed by DSC equipment. The transition at approximately 75 °C relates to specific heat of the material. This is a first order endothermic process where heat flow is reduced in the sample thermocouple due to the adsorption of energy into the material. This measurement can be used to measure the heat capacity of materials (O'Neill, 1966). The peak at 146 °C is a second order transition and relates to a physical change in a material. In this case the change is exothermic and could indicate decomposition, oxidation or in this case crystallisation in the material (Toda et al., 1997). The final peak at 242.3 °C is an endothermic transition and could relate to physical phenomena such as evaporation, reduction or in this case melting (Alamo & Mandelkern, 2003). Errors in measurement can primarily come from calibration and the differences between reference and sample noted in section 2.5.1.

3 Dielectric sensor design and measurement

In this chapter the simulation, design and measurement of two dielectric sensors will be discussed. Both instruments are to be integrated into a larger system and therefore specific design considerations are required for each device. The first is a microwave cavity resonator (MCR) used for its high Q factor and ability to be strongly coupled when using lossy samples. The second is a hairpin resonator used for its open structure. Also the data acquisition system will be detailed in this chapter.

3.1 Microwave cavity resonator

This dielectric sensor is to be used in simultaneous measurement with neutron diffraction techniques, as discussed in chapter 4. Neutron diffraction measurements require approximately 5 cm^3 of sample, which is a particular to the neutron diffractometer used here (and for neutron diffraction generally). Therefore the dielectric sensor will need to enclose the entire sample space and be able to deal with the very high dielectric losses that sometimes occur in heavily ammoniated samples that reduce the signal to noise ratio for dielectric measurement. For these reasons an MCR is preferred over other dielectric sensors, such as parallel plate (Hoppe et al., 2014), transmission line (Stuchly & Bassey, 1998) and coax probe (Marsland & Evans, 1987) methods. The other design requirements for this sensor are as follows.

- Internal dimensions of cavity chosen to give a resonant mode at approximately 2.45 GHz to measure ammonia adsorption.
- Another resonant mode which is independent of ammonia adsorption which can be used as a control measurement.
- A signal to noise ratio of at least 10 dB for the lossiest samples.
- 2.1 cm diameter hole through the cavity to fit a quartz tube.
- 2 cm thinned walled section to allow passage of neutrons through the material without compromising the MCR's mechanical stability.

3.1.1 Mechanical construction

An MCR with a high quality factor (Q) when empty is desirable for dielectric measurement. Q for the empty cavity is inversely proportional to the surface resistance (R_s) of the metal making up the cavity walls, as shown in Equation 3.1 (full derivation in appendix 8.1), where (a) is the radius and (d) is the height.

$$Q = \frac{\omega\mu_0}{2R_s\left(\frac{1}{a}+\frac{1}{d}\right)}$$
Equation 3.1

So the material chosen for the cavity walls should have a low surface resistance and therefore high conductivity to increase the Q factor. The other consideration for the material in the MCR construction is that the neutron beam and the scattered signal will have to penetrate the cavity walls. This means that the cavity walls should have a low neutron scattering cross section, so that the interference in measurement arising from the metal walls will be kept to a minimum. The neutron scattering cross section is made up of coherent scattering that will cause Bragg peaks from the material, incoherent scattering and adsorption that will increase the noise floor. Both coherent and incoherent scattering should be as low as possible. However, spurious Bragg peaks caused from coherent scattering have the potential to cause major problems in structural analysis of the sample.

Table 3.1 shows the electrical conductivities and neutron scattering cross section of some machinable materials that can be manufactured into MCR's. Purely from an electrical standpoint, sliver or copper would be the best choice as the cavity material. However, they both have relatively high coherent scattering and silver has high incoherent scattering, not to mention the high cost of these materials. Similarly, vanadium has the best coherent scattering and acceptable incoherent scattering but low electrical conductivity. So aluminium was chosen as a reasonable compromise between these two parameters.

Table 3.1 – Electrical conductivity and neutron scattering cross sections of typical materials used to make cavity structures (Kaye & Laby, 1995) (Sears, 1992).

Material	Electrical conductivity ×106 S/m	Neutron scattering b(coherent)	Neutron scattering b(incoherent+adsorbtion)
Silver	68.03	4.407	63.3
Copper	64.94	7.485	4.33
Aluminium	41.32	1.495	0.239
Tungsten	20.75	2.97	19.9
Vanadium	5.52	0.018	10.16
Steel (stainless)	2.39	11.22	2.96

A MCR has two standard geometries, rectangular and cylindrical (Ramo et al., 1994). For this application a cylindrical cavity design was chosen, since this will cause the scattered signal from the neutron beam to have equal attenuation and noise from all angles, as shown in Figure 3.1. For production purposes the cavity structure was machined out of three parts and the schematic diagram is shown in appendix 8.2.2. This will reduce the Q factor of the cavity quite significantly due to a bad electrical connection between the aluminium plates. To improve the conductive path for the plate to plate connection, bolts are used to clamp the plates together. However using steel bolts (as would be the norm) would cause large coherent scattering, as detailed in Table 3.1, due to the bolts passing across the scattering region. Nylon bolts are used instead. This does not give as good mechanical and electrical connection but nylon does have a low coherent scattering.

Figure 3.1 shows that the centre plate of the cavity has a 2 cm wide band where the aluminium wall has been thinned to a depth of 1 mm to reduce further coherent and incoherent scattering from the walls. Finally the cavity structure has a 2.1 cm diameter axial hole (top and bottom) to allow placement of a quartz tube in the centre of the cavity. Further explanation of the choice of the inlet and outlet holes is detailed in section 3.1.3.
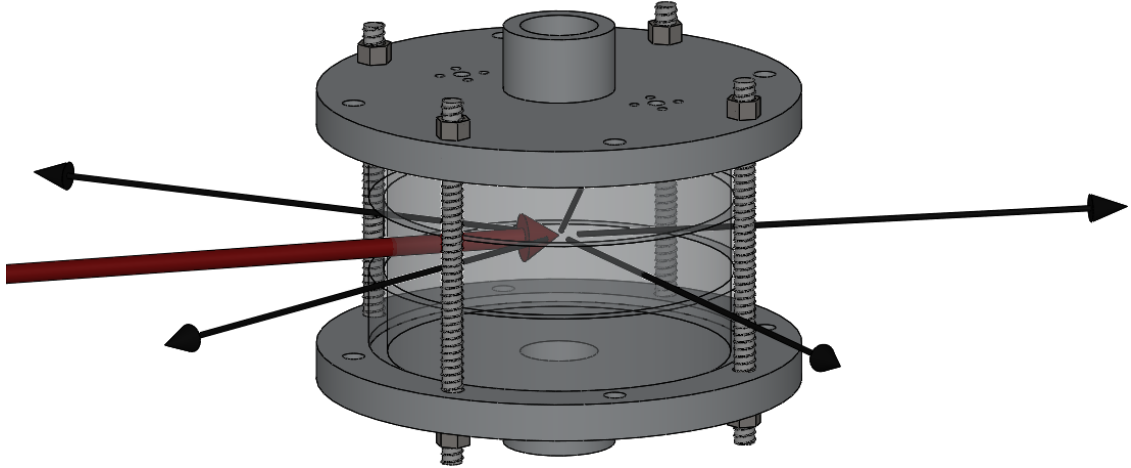
Figure 3.1 – Microwave cavity design for use in a neutron diffractometer showing neutron beams incident signal (red) and scattered signal (black).

3.1.2   Electromagnetic design

The electromagnetic design primarily comes from the choice of internal dimensions of the cavity structure. Equation 3.2 shows the frequency of mode (f_{nml}), where n,m and l are the mode numbers. (a) and (d) are the radius and height of the cavity and (p_{nm}) is the mth zero of the Bessel function of the first kind $J_n(x)$. For example, for the TM$_{010}$ mode, p_{01} = 2.405 (Pozar, 1998). Note that the designed frequency of operation is for an empty cavity and therefore (μ_r) and (ε_r) are assumed to be equal to one.

$$f_{nml} = \frac{c}{2\pi\sqrt{\mu_r \varepsilon_r}}\sqrt{\left(\frac{p_{nm}}{a}\right)^2 + \left(\frac{l\pi}{d}\right)^2}$$

Equation 3.2

The mode chosen for dielectric measurement is the transverse magnetic (TM$_{010}$) mode as seen in a finite element model preformed using COMSOL multiphysics as shown in Figure 3.2 (left). This is a common mode used for measurement proposes (Li et al., 1981) (Bourdel et al., 2000). The mode has a high uniform electric field near the cavity axis. This will give maximum sensitivity to dielectric changes in the centre of the cavity space. The electric field in this mode is directed parallel to the axis and hence the walls. The field is also parallel to the sample tube, resulting in minor depolarising effects from the quartz tube, allowing simple perturbation theory (from Equation 2.8 and Equation 2.9) to be used to extract the dielectric properties.

The frequency of operation of TM_{010} has no dependence on the cavity height and therefore the ideal cavity radius to achieve the desired f_{nml} of 2.45 GHz (A common frequency used for measurement) is shown in Equation 3.3. The actual radius chosen for the cavity was 46 mm, which will give a theoretical TM_{010} resonant frequency of 2.495 GHz.

$$a = \frac{p_{nm}c}{2\pi f_{nml}} = 46.84 \; mm$$
<div align="right">**Equation 3.3**</div>

This slightly higher frequency was chosen because when a sample is placed in the cavity the resonant frequency will drop towards the desired frequency of operation. To ensure that the TM_{010} mode is free from interference there should be no other modes within ±500 MHz of TM_{010}. The transverse electric mode (TE_{111}) could interfere with the TM_{010} mode if the internal height of the cavity is around 95 mm. However the height of the cavity was set at 65 mm to push TE_{111} up in frequency to 3 GHz.

The distributions of modes from the chosen internal dimensions are shown in Table 3.2, where the spectral separation between TM_{010} and the next closest mode (TE_{111}) can be clearly seen. Other modes of interest are labelled in Table 3.2.
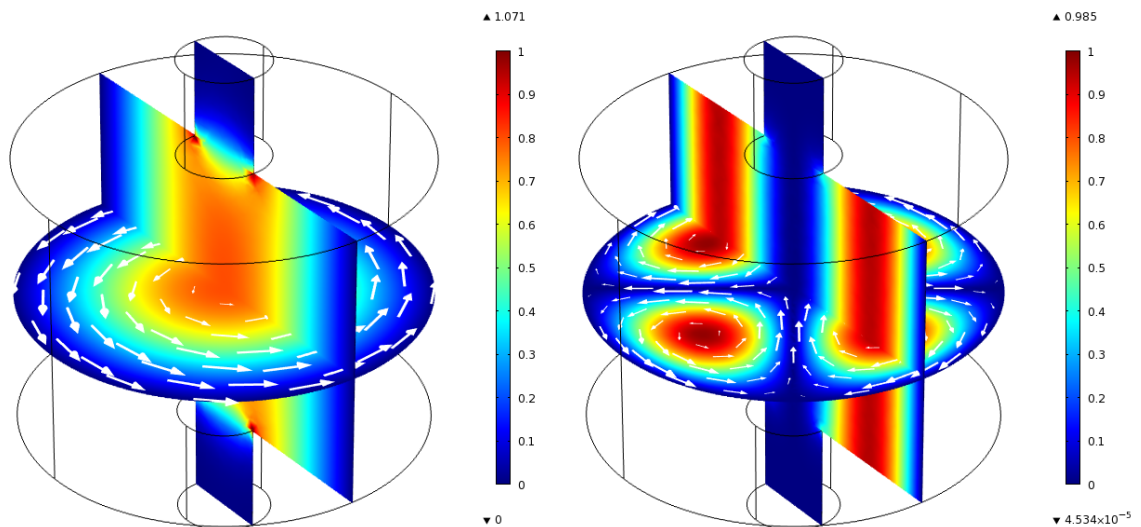

Figure 3.2 – Electric field distribution of TM_{010} (left) and TM_{210} (right) showing normalised electric field distribution (colour scale) and magnetic field distribution (arrows). These simulations were performed using COMSOL multiphysics.

TM_{110} has a maximum magnetic field in the centre of the cavity and so can be used to measure changes in magnetic properties of materials. The materials tested in this investigation showed little to no change in magnetic properties due to their weak, diamagnetic properties and thus no useful analysis was extracted from the information of this mode. TM_{020} is the second order variant of TM_{010}. It has a more concentrated field distribution around the centre of the cavity and is more sensitive to dielectric changes than TM_{010}. However this increased sensitivity means there are greater frequency shifts in this mode and it was found in certain circumstances the frequency of the TM_{020} mode dropped into adjacent modes, causing loss of signal.

The final mode of interest is the TM_{210} which has a theoretical frequency of operation of 5.32 GHz. The field distribution of this mode is shown in Figure 3.2 (right) where there is no electric or magnetic field in the centre of the cavity and so it is insensitive to any changes to the material property when the material is placed in the centre of the cavity. Because the cavity's frequency of operation is determined by the internal dimensions, any changes in temperature of the cavity will cause frequency shifts in the resonance due to thermal expansion/contraction, and this could be interpreted as changes in the sample. Due to TM_{210} insensitivity to the sample, any change in frequency in this mode is from the expansion and contraction of the cavity space and so then can be used to correct for temperature changes affecting the TM_{010} mode, as discussed in section 4.1.3.

Table 3.2 – Theoretical mode distribution across the frequency spectrum for proposed MCR, labelled resonant modes of interest.
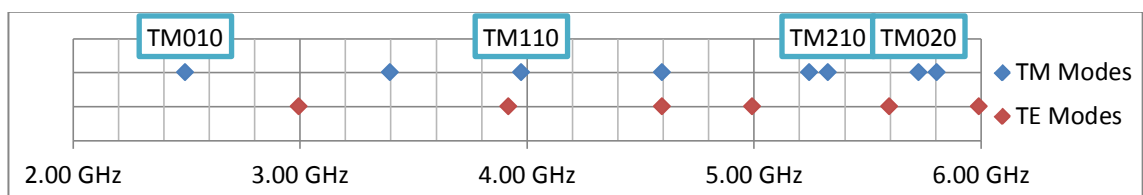
3.1.3   RF chokes

As stated in previous sections, a quartz tube is inserted through the cavity space to hold the sample in the centre of the cavity and to allow a gas flow of ammonia through the sample. The schematic diagram of the quartz tube is shown in appendix 8.1.3. To accommodate the tube 2.1 cm diameter holes are machined at the top and bottom of the cavity structure. Holes of this size can cause significant problems in the electromagnetic operation of the MCR.

Firstly the hole allows radiation of electromagnetic energy out of the cavity structure. This can lead to a greatly reduced Q factor. Secondly, this electromagnetic radiation can couple to materials in the surrounding environment, so that any dielectric changes around the hole (but outside the cavity) will also be measured. A solution to this problem is to have radio frequency (RF) chokes. These structures act as waveguides that operate well below their cut-off frequency so that they reflect the transmission signal along them and so maintain the electrical energy within the cavity structure. This effect is shown in Figure 3.3 in a cross section model of the MCR, with the RF choke length set as 2.3 cm.
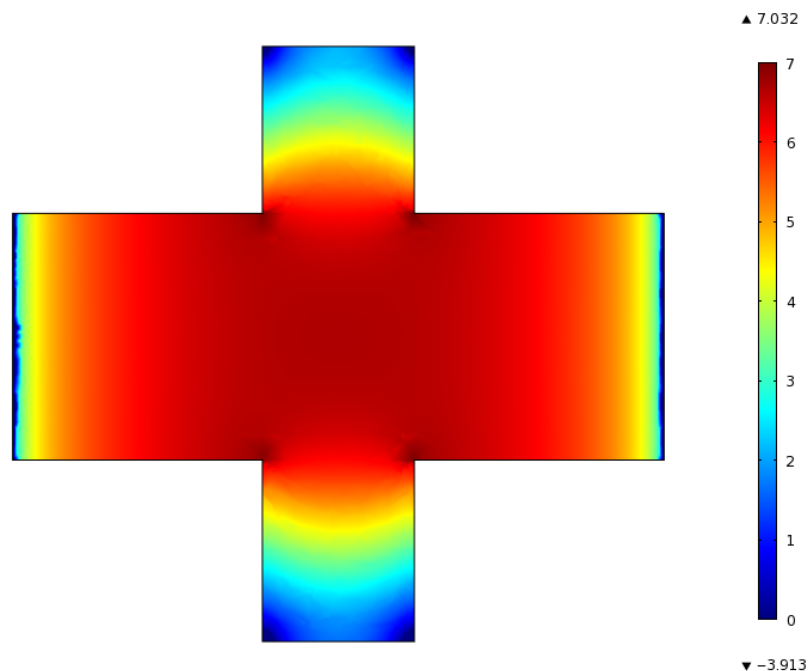

Figure 3.3 – COMSOL simulation showing the cross section of the MCR in the TM$_{010}$ mode, with the Log scale electric field distribution of TM$_{010}$ detailing the effect of the RF chokes in reducing the EM radiation out of the cavity.

The field intensity drops across the length of the RF choke and at the interface with the outside environment the field intensity is approximately four orders of magnitude less than the field in the centre of the cavity. This means any external effects will have negligible effect on the Q factor and resonant frequency of the cavity.

3.1.4   Calibration

With dimensions (a) and (d) chosen in the previous section the theoretical Q factor for the cavity can be attained from Equation 3.1. This Q factor was calculated at 16420. However this Q factor calculation does not take into account the losses caused from the connection between individual plates of the cavity. Furthermore, the effective area of the cavity is increased due to surface roughness (on a scale greater than the microwave skin depth, which is about 1.6 μm at 2.5 GHz for aluminium) and the degraded conductivity of the surface layer of aluminium caused by machining (e.g. by the introduction of defects and stress). The actual Q factor was first measured to be 6280. However, during preliminary measurements presented in section 4.2, sample material from a break in the quartz tube reacted with the aluminium cavity, causing damage to the cavity. The cavity was mechanically cleaned and the Q factor was found to be much lower than its original value (1784).

The cavity was measured on an Agilent PNA and the important properties of the MCR are shown in Table 3.3. This table displays the unloaded resonant frequency (f_0) and the unloaded bandwidth (B_0) of the cavity, which are required parameters to compute complex permittivity of sample materials. The other parameter that is needed from the intrinsic cavity properties to compute complex permittivity, as shown in Equation 2.12 and Equation 2.13, is the effective cavity volume (V_c). Because the electrical field distribution is not uniform across the cavity and focused towards the sample position, there is an effective filling factor for the cavity volume shown in Equation 3.4. This can be determined from direct integration of the electric field energy.

$$V_c = \pi a^2 d \times J_1^2(p_{01}) = 0.269 \, \pi a^2 d \qquad \qquad \textbf{Equation 3.4}$$

Therefore the theoretical (V_c) for the cavity is 1.162×10^{-4} m^3. The actual (V_c) will differ from the theoretical value due to change in field distribution from the RF chokes and differences in cavity volume due to mechanical tolerances. To determine the actual effective cavity volume metal spheres of varying (but known) size are placed on the cavity axis. Results of this are shown in appendix 8.3.1. The spheres develop a known electric dipole moment, from which the effective cavity volume can be found experimentally. The value determined this way is 8.67×10^{-5} m^3, and this is used in the cavity perturbation analysis to extract values of the sample permittivity.

To calibrate out effects from temperature on cavity measurements, the frequency and bandwidth shift per degree was measured for both TM_{010} and TM_{210}. This was done by measuring the (f_0) and (B_0) of the cavity under a controlled temperature ramp with no sample present.

Table 3.3 – Measured operating properties of MCR modes TM_{010} and TM_{210}.

	TM_{010}	TM_{210}
Resonant frequency (GHz)	2.5107	5.3147
Resonant bandwidth (KHz)	1408	2943
Insertion loss (dB)	16.173	2.7245
Q factor	1784	1807
Effective volume (m³)	8.6693 x 10^{-5}	N/A
Frequency shift per degree (KHz)	57.93	120.95
Bandwidth shift per degree (KHz)	1.808	2.369

The results of these ramps are shown in appendix 8.3.1. As expected, the frequency shifts per degree for the TM_{010} to TM_{210} modes scale exactly with the frequency ratio, which is important for dealing with temperature drifts. The bandwidth shift due to temperature shows hysteresis between the heating and cooling of the cavity. The bandwidth is related to the conductivity of the cavity and the different thermal expansion of nylon to aluminium will change the electrical contact between the plates of the cavity. This is the most likely reason for the hysteretic effect and is not due to a thermal lag.

3.2 Hairpin cavity resonator

The design of a dielectric sensor for use in simultaneous measurement with X-ray diffraction has many of same design considerations as discussed in section 3.1 for the cylindrical cavity. However due to the differences in X-rays to neutrons there are some unique design constraints. The different experimental conditions are discussed in chapter 5. The main two different design considerations are, firstly the change in sample volume from the range of cm^3 in the neutron experiments to mm^3 in X-ray experiments; Secondly, the highly attenuating nature of X-rays compared to neutrons means that there is a much greater requirement for an unimpeded beam path. A hairpin cavity resonator was used to satisfy these two design considerations and the reasoning of the design is discussed in this section.

3.2.1 Mechanical construction

As with the cavity resonator from section 3.1.1, the resonant structure is made out of aluminium for its highly conducting properties and ease of machining. As shown in Figure 3.4, the hairpin resonator sits on a low loss polytetrafluoroethylene (PTFE) holder, which is screwed down. PTFE is used because of its low dielectric losses (loss tangent of 5.824×10^{-4}) and low permittivity of about 2.05. Therefore it does not influence the electromagnetic fields of the resonator (Krupka et al., 1998), bearing in mind that the PTFE sits at the magnetic field end of the hairpin, and introduces a negligible dielectric loss. Two holes of 5 mm diameter are drilled in the PTFE holder to allow space for the coupling structures (in this case loops) connected to the microwave ports. A full schematic diagram of the hairpin resonator is shown in appendix 8.2.3.

The sample material in the X-ray experiments will be contained within a 1 mm of outer diameter and 0.8 mm inner diameter, discussed in more detail in chapter 5. Holes of 1.1 mm diameter in the electromagnetic shielding and in the resonant structure are positioned for placement of the quartz capillary in the hairpin's electric field region.
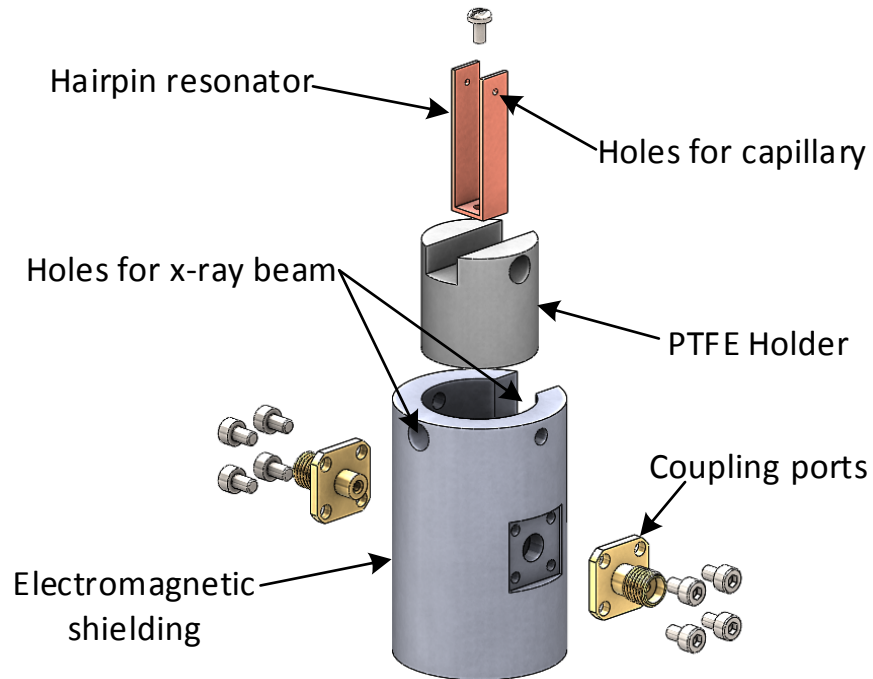
Hairpin resonator

Holes for capillary

Holes for x-ray beam

PTFE Holder

Coupling ports

Electromagnetic shielding

Figure 3.4 – Diagram of Hairpin resonator construction showing individual parts.

For the X-ray photon energy that will be used in the experiments (15 Kev), the X-ray mass attenuation coefficient for aluminium is 7.955 cm^2/g (Hubbell & Seltzer, 1996). This means that 1 mm thickness of aluminium within the beam path will cause 88.3% of the incident signal to be attenuated and thus cause a considerable loss in detectable signal strength. Because of this, the design focused on having no aluminium within the beam path. This is why the hairpin design was chosen over other possible solutions, since the open ends of the hairpin can be fully exposed without causing much reduction in Q, as shown in Figure 3.4 and Figure 3.5. The electromagnetic shielding has a 5 mm diameter hole for the incident X-ray beam and a 10 mm by 8 mm rectangular window for the diffracted beam.
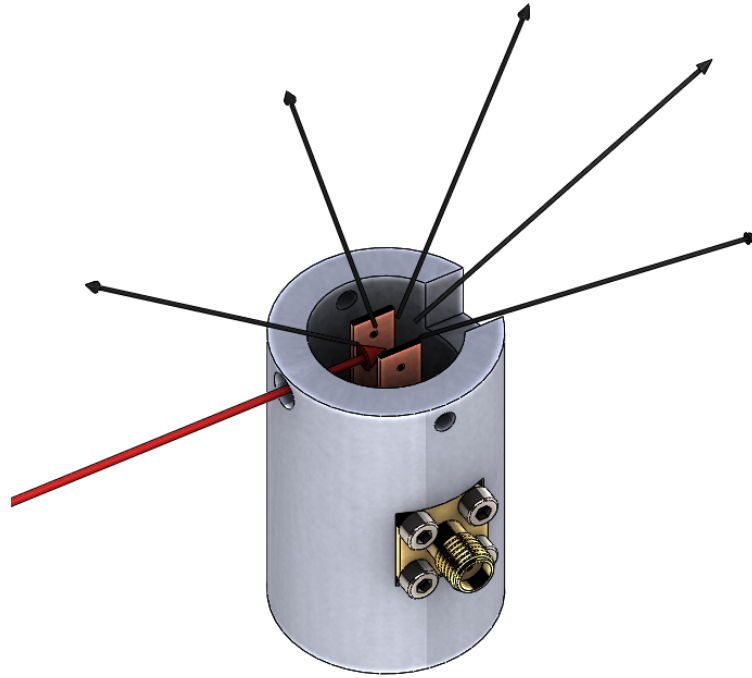
Figure 3.5 – Hairpin resonator design showing X-ray beams incident signal (red) and scattered signal (black).

The X-ray detectors for the diffracted signal are arranged vertically around a 150° arc. The notch ensures that the diffracted beam is unimpeded over an arc of angle 179.3^0, so giving the widest range of possible scattering angles, from backscattering to low angle scattering, as shown in Figure 3.5. The detectors are located 140 mm away from the sample and require an unimpeded perpendicular scattering angle of 6.1^0. The sample capillary is positioned 3 mm from the end of the hairpin, giving an unimpeded angle of 60.6^0 to the vertical. Hence, by careful design, the diffracted X-ray beam is unimpeded in all relevant directions.

3.2.2   Electromagnetic design

The electromagnetic properties of the hairpin resonator, like the MCR discussed in section 3.1, are mainly dependent on the dimensions of the resonant structure (Piejak et al., 2004). In this case the dimensions of interest are shown in Figure 3.6. The thickness (t) of the resonator plates need to be greater than the skin depth of 1.65 µm and structurally strong, so in this case a thickness of 0.8 mm was chosen for ease of construction.
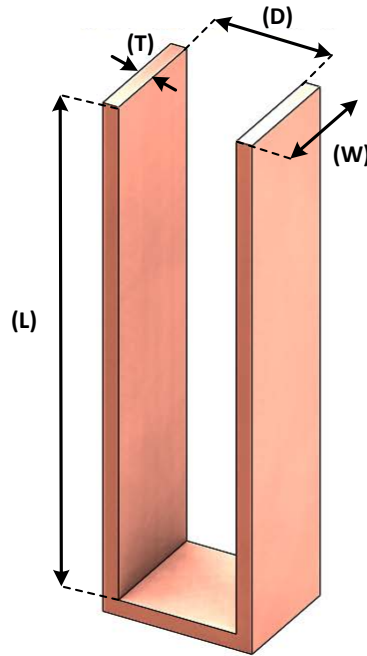
Figure 3.6 – Hairpin resonator structure showing dimensions that define its electromagnetic properties (l) length, (w) width, (d) distance between plates and (t) thickness.

The frequencies of the resonant modes of the hairpin cavity are mainly determined by the length (l) (Dankov et al., 2010). The fundamental resonant mode will be used for measurements, therefore the mode number (p) from Equation 3.5 will equal one. There will be a high electric field at the open end of the hairpin, where the sample is placed, and a high magnetic field at the closed end.

$$l = p\frac{c}{4f}$$
Equation 3.5

The resonator will also have resonant modes at odd multiples of the fundamental frequency. Assuming the desired frequency of 2.45 GHz, the theoretical length of the hairpin would be 30.6mm. Because of the open structure nature of the resonator, the effective length of the resonator will be longer, as seen from the COMSOL simulations in Figure 3.7 (left), where the EM fields are seen to spill out from the space between the plates. Because of this the actual length was chosen to be 25 mm, which was verified by simulation to yield a resonant frequency of about 2.45 GHz.

The X-ray beam is 2.5 mm wide and so this sets the minimum distance between the plates (d). Also a larger plate distance will improve the Q factor. As well as high Q factor, a uniform electric field within the sample space is desired. With an increasing plate distance the field non-uniformity will increase and similarly the field non-uniformity will increase with shortening width (w) of the plates. The plate width and separation were both set as 6 mm. As seen from Figure 3.7 (left), the electric field distribution at the sample position varies by approximately 5% along the length of the sample. The field non-uniformity also increases towards the top of the resonator structure and this is why the hairpin holes (and so the capillary) position is set 3 mm down from the open ends of the hairpin. The 1.1 mm diameter holes for the capillary will have little effect on the electric field distribution as seen in Figure 3.7 (left). Whilst the electric field will be largest at the hairpin's open end, the magnetic field will be at a maximum at the closed end, as seen in Figure 3.7 (right). The coupling loops are positioned, as shown in Figure 3.4, so that they can couple into the magnetic field.
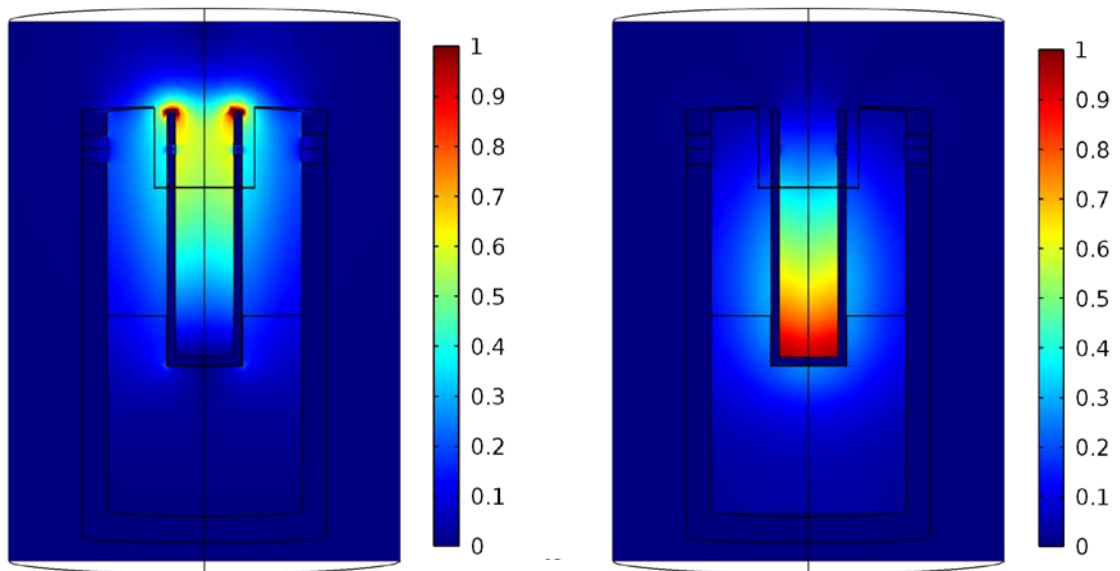

Figure 3.7 – COMSOL simulation of hairpin cavity resonator showing electric field distribution (left) and magnetic field distribution (right).

The outer electromagnetic shielding contains the EM fields that spill out from the hairpin resonator. This containment improves the Q factor of the cavity by reducing the radiation losses. The EM shielding should be as close to the resonant structure as possible, but far enough away from the hairpin so as not to interfere with the X-ray signal. The added holes for capillary placement and the diffracted beam cause very little reduction in the total Q factor of the cavity resonator.

3.2.3   Calibration

With dimensions (l) and (d) chosen in the previous section, the theoretical maximum possible Q factor for the hairpin cavity can be attained from Equation 3.6 with the full derivation shown in appendix 8.1.3.

$$Q = \frac{\omega \mu_0}{4R_s \left(\frac{1}{2l} + \frac{1}{d} \right)}$$

Equation 3.6

The maximum attainable Q factor was calculated at 1725. This value is nearly ten times lower than the Q factor of a MCR as discussed in section 3.1, due to the low volume to surface area ratio. This is why MCR's are much more desirable to use as dielectric sensors than hairpin resonators, unless for specific circumstances as explained here. Due to the open structure of the hairpin resonator used for the X-ray experiments, the actual measured Q factor will be considerably lower even with the electromagnetic shielding used. This Q factor was experimentally measured to be 744 and this as well as the other important parameters are shown in Table 3.4. The equation used to determine the effective volume of the hairpin cavity (used in the cavity perturbation equations) is shown in Equation 3.7. With the dimensions of the hairpin the theoretical effective volume of the hairpin is $4.5 \times 10^{-7} \text{m}^3$

$$V_c = \int_0^p \sin^2 \left(\frac{ldw\pi}{2} \right) . dl = \frac{ldw}{2}$$

Equation 3.7

Table 3.4 – Measured operating properties of empty hairpin resonator.

	First order mode
Resonant frequency (GHz)	2.5447
Resonant bandwidth (KHz)	3419
Insertion loss (dB)	19.83
Q factor	744
Effective volume (m³)	5.089×10^{-6}

However, due to the open structure of the hairpin, the magnetic and electric field (in particular) spill out of the "enclosed" hairpin volume. This will cause the effective cavity volume to be larger than calculated (and also the resonant frequency to be smaller than expected, as previously discussed). Performing a calibration using metal spheres, shown in appendix 8.3.2, (noting that a different range of sphere size is used because of smaller cavity structure) the actual effective cavity volume of $5.1 \times 10^{-7} m^3$ can be attained.

A temperature ramp was performed on the hairpin cavity, as shown in appendix 8.3.2, to attain the frequency and bandwidth shift per degree. However it was found that the profile of frequency and bandwidth shift was highly nonlinear. This is because there is thermal expansion from the hairpin, the EM shielding and the PTFE post (PTFE is known to have a nonlinear thermal expansion over the temperature range experienced (Kirby, 1956)). Therefore, the frequency and bandwidth shift per degree was not able to be accurately determined. Neither is there any mode of the hairpin which is insensitive to the presence of the sample, so it is not possible to perform temperature correction to any of the microwave data attained from it.

3.3   Measurement System and operation

Dielectric sensors come in many different structures and yet the measurement technique to attain dielectric properties is essentially the same. This is by measuring the S parameters of the sensor by use of a vector network analyser (VNA). Over the years the improvement in quality and versatility of VNA's has been one of the main driving factors in improvement of dielectric measurement (Stancliff & Dunsmore, 2007).

3.3.1   System setup

Cavity perturbation is measured from the voltage reflection (S_{11}) or transmission (S_{21}) coefficients (Sheen, 2009). S_{11} type measurements can yield more accurate results than S_{21} measurements (Gregory & Clarke, 2006). However S_{11} measurements require careful calibration of one port coupling coefficients and tend to have less dynamic range than S_{21} measurements. For these reasons S_{21} type measurements are used in this project and the measurement setup is shown in Figure 3.8. The VNA used in all experiments is a Fieldfox N9912A. This has a smaller dynamic range than other VNA's but is rugged and portable. It was chosen due to the need for a portable system to incorporate into the facilities at the Rutherford Appleton Laboratory, in particular for the neutron and X-ray systems.
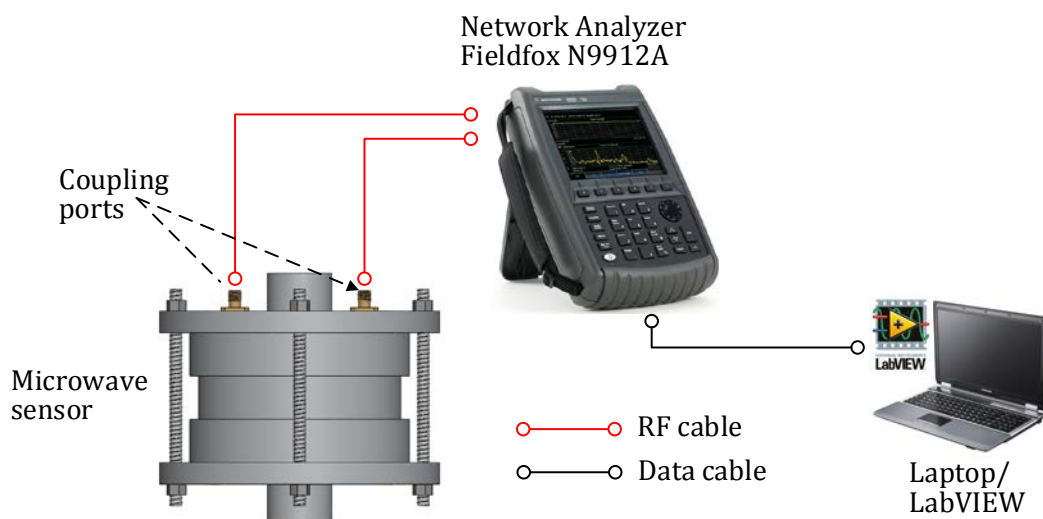

Figure 3.8 – S_{21} measurement setup for microwave dielectric measurement showing RF transmission and automated control system data logging of microwave properties.

The VNA operates by providing an excitation signal (in this case an output power of 0 dBM, i.e 1 mW rms) across a user-specified frequency range and measures what proportion of that signal is transmitted to the receiver port of the VNA. In the case of resonance, the transmitted signal will be at a maximum and insertion loss (the difference in power between the incident and transmitted power) will be at a minimum. Two semi rigid RF cables (Times Microwave) are used to connect the VNA with a pair of square-flanged Sub miniature A (SMA) jack connectors (Farnell), which form the coupling structures for both types of microwave resonator used in this thesis. The SMA connector termination at the cavity will be different according to the type of measurement performed and is discussed further in section 3.3.2. The VNA is connected by an Ethernet cable to a computer which records the S_{21} data (via a National Instruments LabVIEW program) and controls the sweep settings of the VNA, which is discussed in more detail in section 3.3.3.

3.3.2   Coupling structure

A cavity requires input and output ports to measure S_{21} and to enable excitement of the resonant modes of the cavity. There are two methods to achieve this: inductive coupling using a loop structure, Figure 3.9 (left), to couple into a magnetic field and capacitive coupling using an antenna structure, Figure 3.9 (right), to couple into the electric field (Wang et al., 2011).

The position of the coupling structure is important in determining the coupling strength into the cavity. For the cylindrical cavity used for neutron scattering experiments, the primary mode of use is TM_{010}. The coupling structure should ideally be placed where the magnetic or electric field is at a maximum, shown in Figure 3.2 (left). The electric field is strongest in the centre of the radial plane and along the z axis. This means the best position for an antenna coupling structure would be in the centre of the top or bottom plate of the cavity.
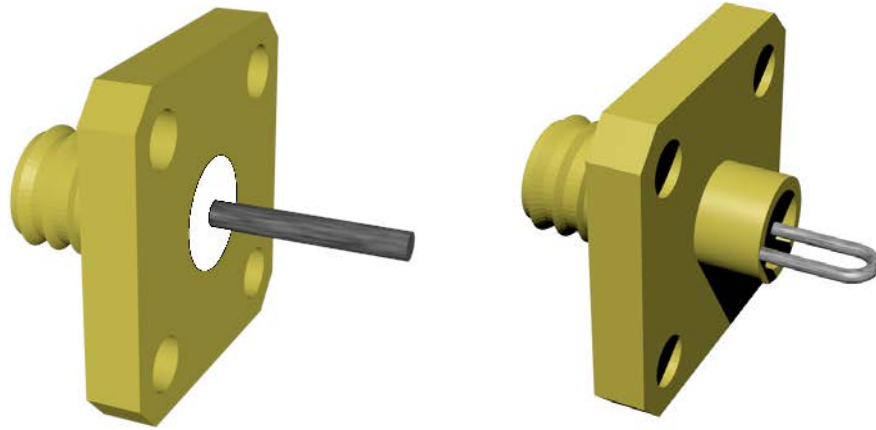
Figure 3.9 – SMA coupling connectors for antenna structure (left, E field coupling) loop structure (right, H field coupling).

The magnetic field is strongest around the inner perimeter of the cavity, so the loop coupling structure would be placed at its circumference. Because the neutron beam source is directed along the azimuth plane and the aluminium wall is thinned in that section, it is not possible to use a loop coupling structure due to signal interference in neutron powder diffraction (NPD) measurements. Hence, antenna coupling at the top of the cavity is used. For the hairpin cavity used for XRD experiments, loop coupling is used to couple into the magnetic field, shown in Figure 3.7 (right). Antenna coupling would not be possible since these would need to be near the open end of the hairpin, so would be in the path of the X-ray beam. For loop coupling the coupling position is orientated towards the base of the hairpin, as here the magnetic field is largest.

The coupling strength is determined by the physical length for the antenna structure (longer length produces stronger coupling) and the area of the loop for the loop structure (larger area produces stronger coupling). For the best measurement capabilities, a cavity should have a high Q factor to get maximum sensitivity and low insertion loss to get the maximum dynamic range.
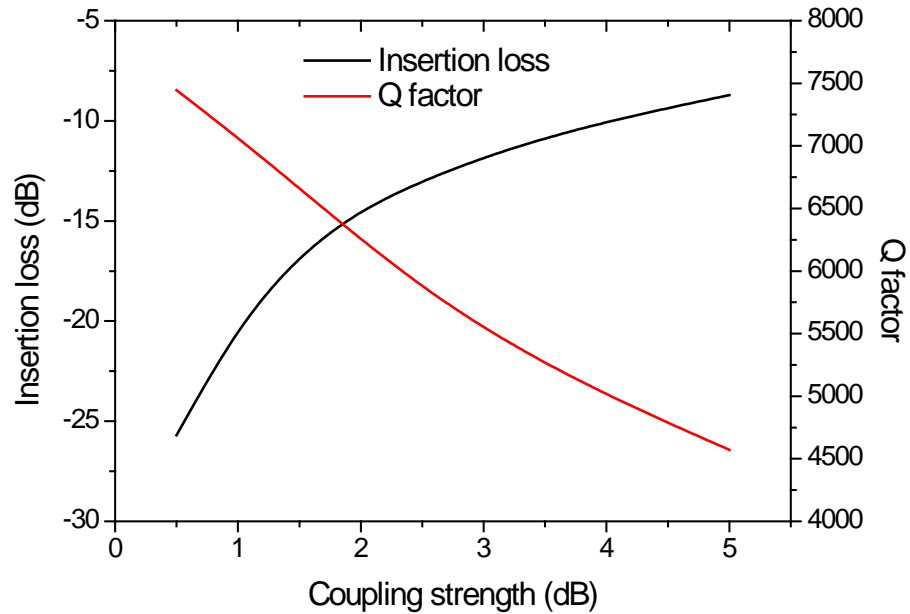
Figure 3.10 – Effect of antenna coupling strength on insertion loss and Q factor of an MCR.

However increasing the strength of the coupling whilst decreasing the insertion loss and so increasing the signal to noise level, reduces the measured (i.e. "loaded") Q factor and it becomes more difficult to extract material parameters from cavity perturbation, unless careful calibration standards are used to quantify the insertion loss very precisely. This is shown in Figure 3.10. Also, high coupling strength will cause cross coupling and therefore unwanted signals in measurements, which is undesirable. In general, the coupling strength should yield an insertion loss in the range of -20 dB to -40 dB, since then the contribution of coupling to the loaded Q is small, and also there is an acceptable signal to noise ratio.

For the hairpin cavity case, because of the low sample volumes used, there is little need for high dynamic range due to small expected changes. Therefore a coupling strength of 0.5 dB is used for S_{11} and S_{22} at resonance to achieve a high Q factor, close to the unloaded Q. For the MCR, larger samples are used and there is a greater need for dynamic range as they become very lossy. From experimental tests, the quartz tube and silicon frit had approximately 10 dB of loss, the lossiest samples had losses of approximately 30 dB and the noise floor of the VNA is 70 dB.

$$Q_0 = \frac{Q_L}{1 - \sqrt{P_0}}$$

Equation 3.8

Therefore the coupling strength chosen was 1.1 dB for S_{11} and S_{22} to give a total (worst case) insertion loss of the complete system at approximately 60 dB, giving at least 10 dB SNR at all times. Any form of coupling will cause a loading effect on the Q factor as seen from Figure 3.10. To correct for this in measurements the unloaded Q factor needs to be calculated. This is done in Equation 3.8 where the unloaded Q factor (Q_0) can be calculated from the loaded Q factor (Q_L) and the peak power at resonance (P_0).

3.3.3   Measurement and control system

To measure the complex permittivity of materials ($\varepsilon_1 - j\varepsilon_2$) three experimental properties are measured, the resonant frequency, bandwidth of resonance and insertion loss (Li et al., 1981). The change in frequency (Δf), shown in Figure 3.11, from the unperturbed cavity determines the change in real permittivity (ε_1). The change in bandwidth of the resonance ($B_s - B_0$) and the change in insertion loss (ΔIL) can both be used to measure change in dielectric losses (ε_2).

Typically for dielectric material measurement, the resonant frequency decreases with increasing permittivity and resonant bandwidth increases with increasing dielectric losses. This is shown in Figure 3.11 for the change in resonant properties for a sample of calcium iodide. In this measurement the VNA collected 51 data points across the frequency range at an intermediate frequency (IF) bandwidth of 300 Hz. This gave approximately 3 seconds sampling time per mode. The relevant information can be extracted straight from the S parameter data (Ewing & Royal, 2002). In this project the S_{21} data from the VNA is fed into a control system run in LabVIEW, as shown in Figure 3.8. The software performs a non-linear, least squares curve fitting to a Lorentzian response to determine the resonant frequencies and bandwidths (Hartley et al., 2015).
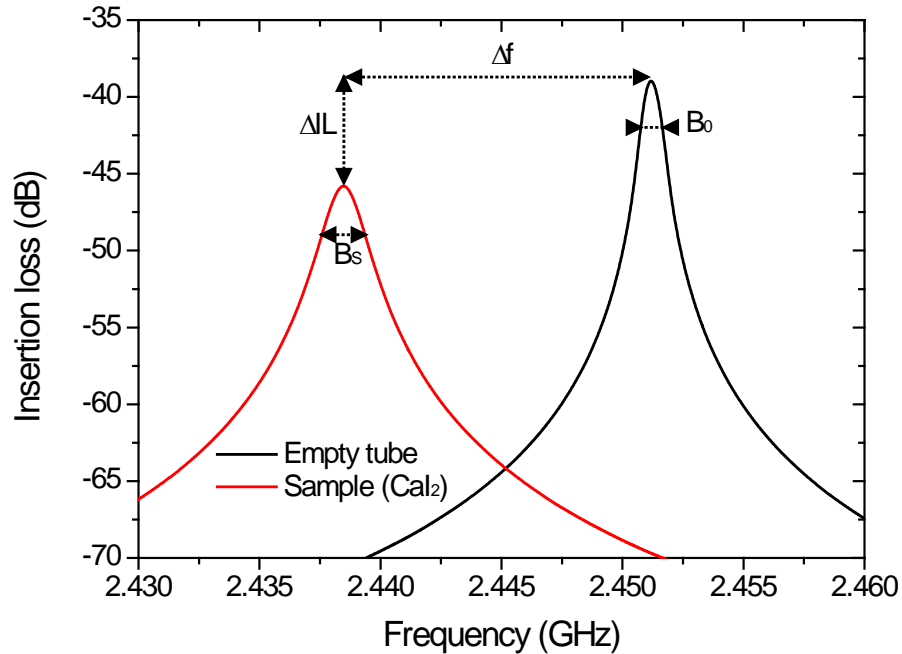
Figure 3.11 – Typical S$_{21}$ plot showing resonant curve when unloaded and loaded with dielectric material.

The data is then logged in a TDMS streaming file and post processing is applied to attain the real and imaginary permittivities by using Equation 2.12 and Equation 2.13. The LabVIEW software feeds back into the VNA, the frequency range for the next scan. This is set as two times the bandwidth of the previous trace and the centre frequency equal to that of the previous resonant frequency recorded. This control system can therefore automatically measure dielectric properties over time and capture dynamic processes. An example of this dynamic measurement system in action is shown in Figure 3.12. This shows a completely different physical system, here the clotting of blood, to show the versatility of the microwave method for measuring dielectric properties of a range of samples. The data shows the change in resonant frequency of venous blood inside a quartz capillary. The blood is taken from the veins in a finger and transported instantly into a quartz capillary within an MCR. The blood congeals in the capillary and the mechanics of this congealing process are shown as features in Figure 3.12. Other plots are shown in appendix 8.4.1.
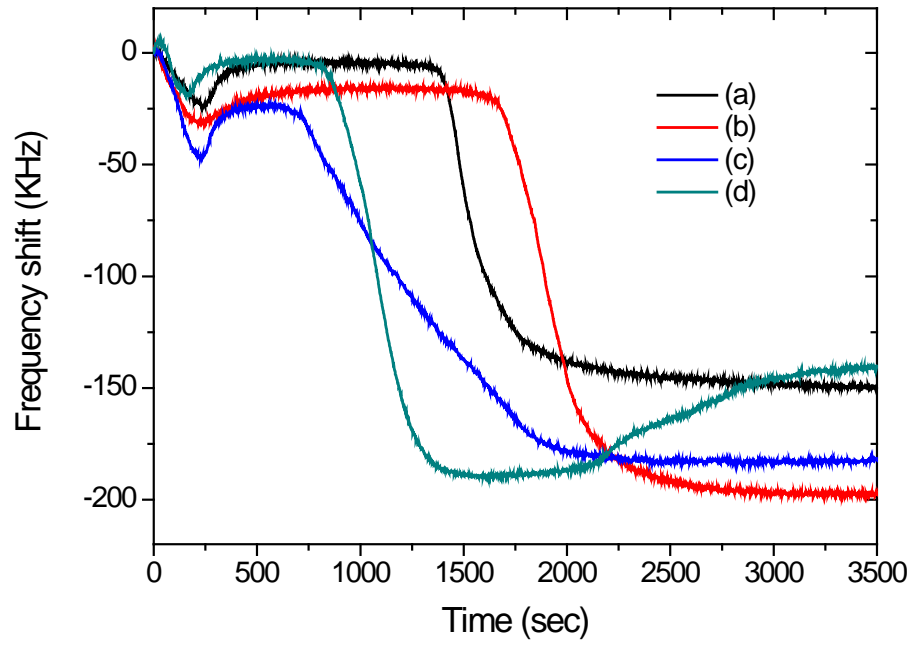
Figure 3.12 – Resonant frequency shift of venous blood congealing over time for four different subjects denoted as (a), (b), (c) and (d).

4   Simultaneous neutron diffraction and microwave measurement

In this chapter the MCR detailed in section 3.1 is integrated into a measurement system to conduct simultaneous measurements as a sample is introduced to ammonia gas. Preliminary measurements were conducted without the use of neutron powder diffraction (NPD) and the results and analysis of these tests are shown. The experiments conducted with the NPD are shown for alkali earth halides and transition metal halides. Analysis is conducted in an attempt to relate dielectric changes measured with structural changes.

4.1   Integrated measurement system

Multiple measurement techniques are used to attain as much information as possible from what is occurring when materials are exposed to ammonia. These are listed in Table 4.1, noting the particular physical property they measure. NPD and MCR will measure changes actually within the sample, whereas the mass spectrometer (MS) and mass flow meter (MFM) will measure changes in the system downstream due to changes from the sample.

Table 4.1 – The measurement devices used in the integrated measurement system and the parameters that they measure.

Measurement device	Abbreviation	Parameter measured
Neutron powder diffractometer	NPD	Material's crystal structure
Microwave cavity resonator	MCR	Material's permittivity
		Material's dielectric losses
Mass spectrometer	MS	Out gas composition
Mass flow meter	MFM	In and out gas mass
		System pressure

4.1.1   Experimental setup

Because some of the materials tested are hydroscopic and therefore air sensitive, the initial sample atmosphere consisted of argon. This is shown in Figure 4.1, where the argon gas flow can be switched by hand (by the three way valve) to ammonia gas flow in the case of preliminary experiments, or deuterated ammonia gas flow in the case of NPD measurements. The mass flow controller (Chell CCD100) regulates the gas flow rate of the system. This mass flow controller also has an MFM as part of the device and another MFM is placed on the gas line just before the MS. The MS (HPR-20 QIC R&D Plus from Hiden analytical) measures the out gas quantities of ammonia or deuterated ammonia, hydrogen or deuterium, argon, nitrogen, oxygen and water. The experimental rig is shown in Figure 4.2 (left), includes the MCR detailed in section 3.1. This fits within the vacuum chamber of the POLARIS NPD at the ISIS facility (Hull et al., 1992) (Smith et al., 1994). The neutron beam dimensions are set at 2 cm height and 1.5 cm width to encompass the entire thinned aluminium wall window in the MCR.
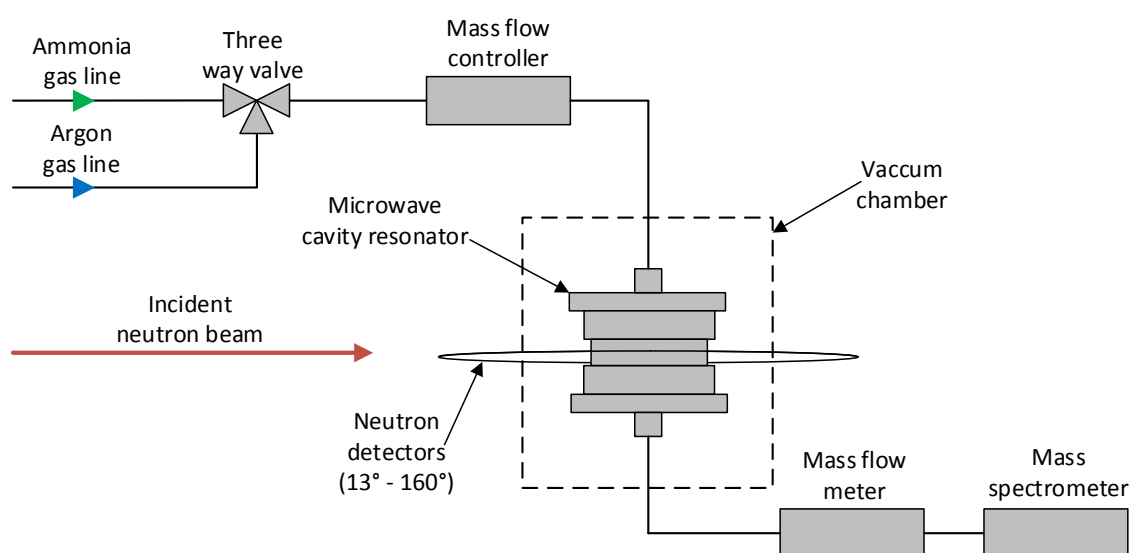
Figure 4.1 – System diagram of simultaneous neutron diffraction and microwave measurement setup showing gas lines and measurement equipment.
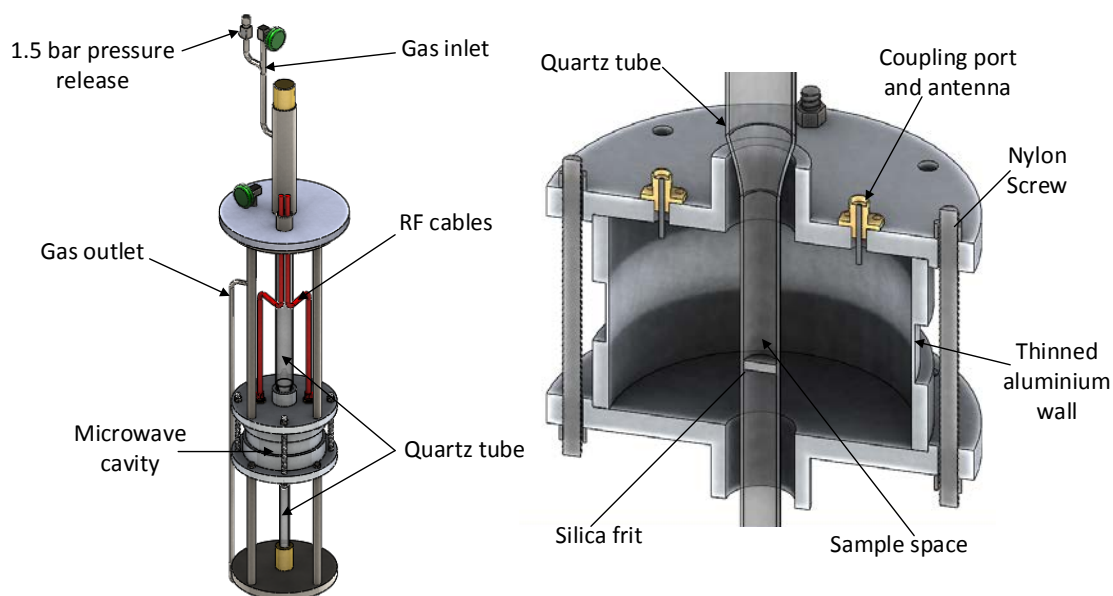
Figure 4.2 – Model of experimental rig (left) that fits within the vacuum chamber of the neutron diffractometer and the inside of the MCR (right).

The NPD measures diffraction angles from 13° to 160°, with the most significant measurements from planar diffraction, as shown in Figure 3.1. The gas outlet shown in Figure 4.2 (left) travels through the neutron beam path. Therefore the experimental rig is orientated so as not to interfere with the diffracted signal from the back-scattering and 90° detectors. The experimental rig has a 1.5 bar release valve to prevent pressure build up which could lead to shattering of the quartz tube. The sample material sits on top a silicon frit and is positioned at the same height as the 2 cm thinned aluminium wall, as shown in Figure 4.2 (right). The experimental rig is also positioned so that the nylon screws from the MCR are orientated so they do not interfere with the incident neutron beam. The MCR data capture system (as detailed in section 3.3.1) was used to collect data every 6 seconds and the NPD data capture system to collect the neutron counts for 2 minute periods to give diffraction pattern slices over the full duration of the experiment.

4.1.2   Experimental procedure

The alkali earth halides and transition metal halides samples used in the experiments were in powder form except for the MgI_2 sample, which was packed into anhydrous beads. The samples were prepared in an inert environment and weighed to an accuracy of 0.01 g. The sample environment was purged with argon gas prior to loading of samples. Background measurements were taken of the empty sample environment under argon gas flow and with the sample in the measurement space under argon gas flow. The material was loaded into the sample position by opening a cap on the top of the rig. This process exposed the sample to air for a short period of time and a small amount of air was introduced into the gas line. Therefore, before ammonia was introduced to the sample it was ensured that the air in the system was completely removed. To begin the experiment, the gas flow was switched from argon gas flow to ammonia gas flow. This point in time signifies the zero point for all experimental results shown in this chapter. At the appropriate time designated by the user, the ammonia gas flow was switched back to argon to see if desorption occurs in the sample. In certain circumstances, adsorption of ammonia into the sample caused the gas line to block. The system has a 1.5 bar pressure release valve but in most cases the gas flow was switched off when the pressure began to increase rapidly, leaving the sample sitting in an ammonia environment for the duration of the experiment. Depending on the sample, its removal from the quartz tube after the experiment sometimes left it available for post TGA, but for some samples the only way to remove the material was by dissolving them in water thus rendering them useless for any post analysis.

4.1.3   Artificial features and measurement uncertainties

Arguably the most significant measurement uncertainties come from the process of loading the sample into the quartz tube. This process firstly exposes the sample to air which will hydrate the sample. However, the hydration process of the materials tested is relatively slow and this should have minimum effect on measurements. Secondly (and more importantly) is that the powdered samples have to drop approximately 0.5 m down the quartz tube to the sample position. It has been observed that some of the powder sticks to the walls of the quartz tube during the powder's descent (more so with the finer powders). Therefore the original sample weight measured and the true sample weight within the measurement region will vary. It is also not possible to quantify this uncertainty so the error in weight could be anything up to (±10%). Therefore results showing percentage weight of ammonia adsorbed are subject to these errors. For measurements of permittivity and dielectric loss the sample volume needs to be known. Therefore this difference in sample amount will give rise to errors in these measurements. Also there are further errors in the computed values of ε_1 and ε_2 due to the material being in powder form, since the sample volume will have to be assumed from effective medium modelling.
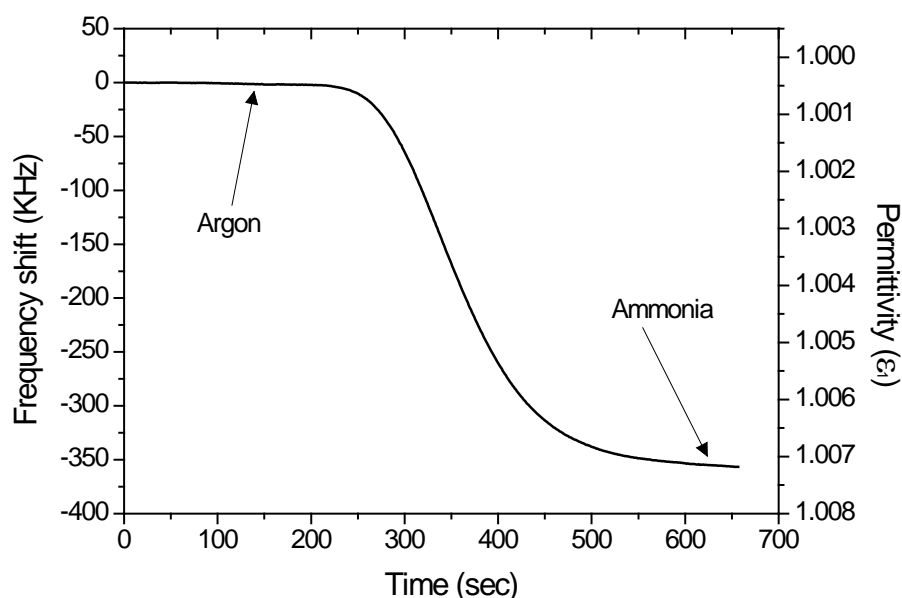
Figure 4.3 – Frequency shift of changing gas composition from Argon to ammonia at gas flow of 40cm^3/min.

Rather than employ any form of effective medium theory, the raw data for the effective permittivity are presented, otherwise the manipulated permittivity values are only as good as the effective medium model. We adopt (with its inherent assumptions of particle shapes and packing density) effective values of the complex permittivity of powder materials calculated directly from Equation 2.12 and Equation 2.13.

When conducting the experimental procedure without a sample present, artificial features are seen in the microwave data in Figure 4.3 and neutron diffraction data in Figure 4.4. The microwave measurement detects the change from argon gas to ammonia gas. This form of measurement can be used as a gas composition sensor (Rauch et al., 2015) and the permittivity measurement of ammonia agrees well with the book value of 1.0071 (Kaye & Laby, 1995). In our situation we are interested in ammonia adsorption, rather than just ammonia in the measurement space. However the change in frequency and bandwidth shown in Figure 4.3 and appendix 8.4.2 are two orders of magnitude less than the changes observed with the sample in the measurement space and therefore has negligible effect on measurements. Due to the time it takes for gas to flow through the gas lines, there is a delay between the switching of the gas line and observation of changes in the MCR. This delay is more pronounced in MS results due to the measurement device being further down the gas line. The NPD results show diffraction peaks when no sample is present. This is due to diffraction from the aluminium from the MCR walls, as shown in Figure 4.4. Aluminium has its most prominent lattice spacings at 2.338 Å, 2.024 Å, 1.431 Å and 1.221 Å (TED PELLA INC, 2015). However as seen from Figure 4.4, the peaks are not located at these d spacings, but instead dual peaks are located adjacent to the expected d spacings. This is because the aluminium walls are $\mp$4.6 cm away from the centre position and will cause a difference in the diffraction path.
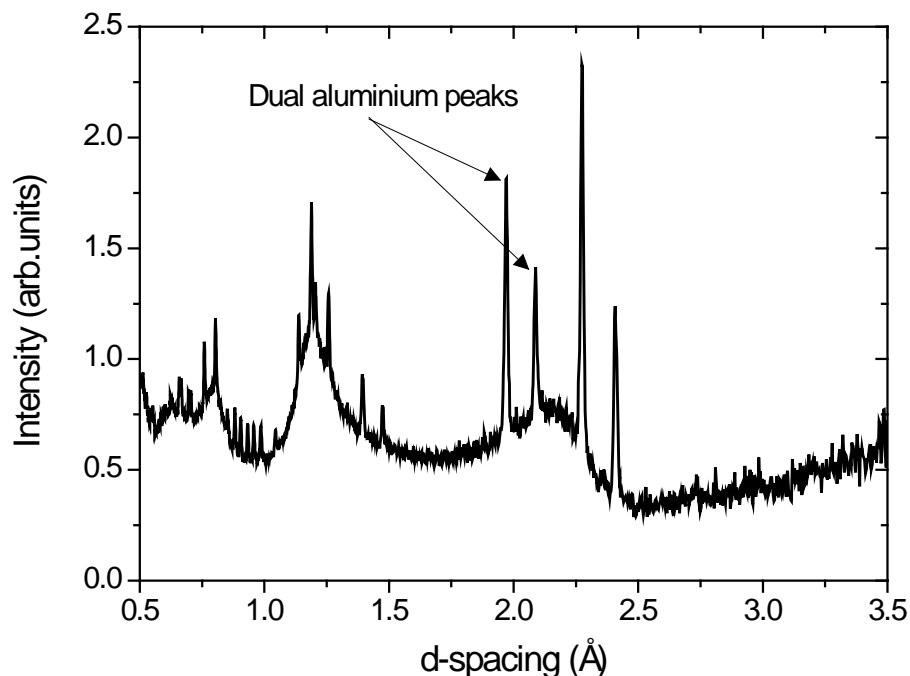
Figure 4.4 – Background neutron powder diffraction pattern of experimental rig showing effect from quartz tube and MCR aluminium housing.

The final feature that the measurement process has to account for is the thermal expansion of the cavity. Because the majority of reactions performed within the sample space are exothermic, invariably some of the heat produced will cause the MCR to heat up, expand and so reduce its resonant frequency (Kajfez et al., 2001). As mentioned in section 3.1.2, the MCR has the TM_{210} mode that can measure the thermal expansion of the cavity, independently of the sample. The profile of this expansion varies from sample to sample, but a general trend is shown in Figure 4.5, for the full length of the experiment for $CuBr_2$ under 5 cm^3/min of ammonia gas flow. From the frequency shift per degree in Table 3.3, the cavity increases in temperature by only 1 °C during the exothermic reaction. Similarly in Figure 4.3, the change in frequency is two orders of magnitude less than the changes caused by the material so that the effects of temperature changes are unnoticeable in the TM_{010} mode measurements.
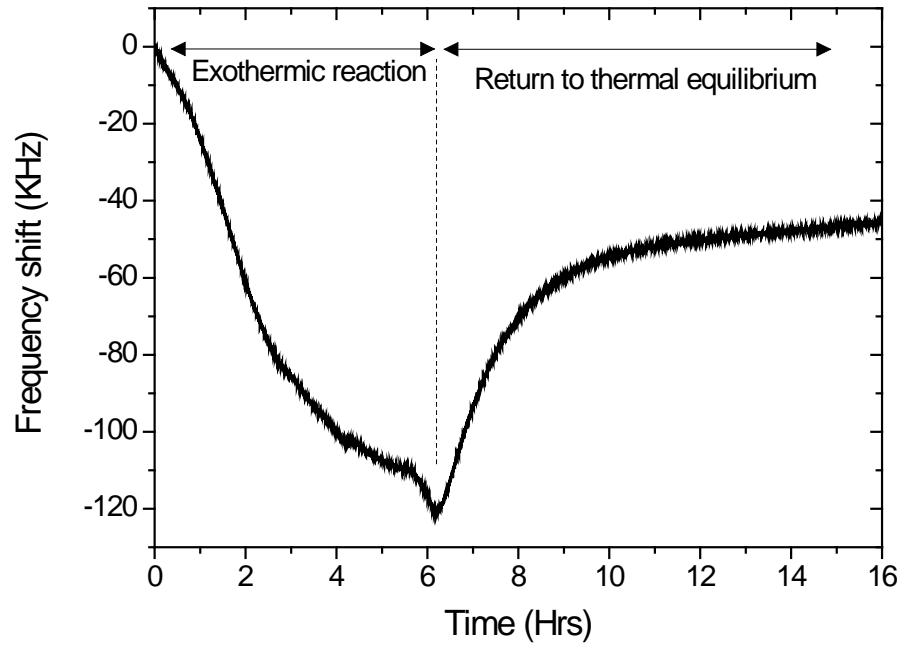
Figure 4.5 – Frequency shift of TM$_{210}$ sample insensitive mode for 1.5g of CuBr$_2$ under 5cm^3/min ammonia gas flow showing effect of the exothermic reaction on thermal expansion of cavity.

4.2 Preliminary measurements

Due to the limited experimental time on the NPD equipment, preliminary measurements were conducted offline, to determine the most suitable and interesting materials to test. The experimental setup and procedure for preliminary measurements are the same as discussed for the measurements with the NPD, except that the experimental rig is in normal atmosphere conditions rather than in a vacuum. A wide range of materials have been tested in anhydrous and hydrated form and all are listed in Table 4.2. Plots of frequency and bandwidth are shown for alkali earth halides in appendix 8.4.3, transition metal halides in appendix 8.4.4 and metal organic frameworks in appendix 8.4.5. Materials $MgCl_2$, $MgBr_2$, $CaCl_2$, $SrCl_2$ and $CuCl_2$ were found to break the quartz tube holding the sample due to the material expansion causing excess pressure on the tube. For this reason, these materials were not tested within the NPD. Given that water has a higher permittivity than ammonia, it is believed that dielectric measurement of the hydrated samples is measuring the release of water from the material over that of ammonia adsorption into the material. This is most prevalent in $CaCl_2(H_2O)_6$ and $CaI_2(H_2O)_6$ samples where the hydrated response differs greatly from the anhydrous response.

Table 4.2 – List of all materials tested using the NPD experimental rig.

Group	Material	
Alkali earth halides	$MgCl_2$	$MgBr_2$
	$MgBr_2(H_2O)_6$	MgI_2
	$CaCl_2(H_2O)_6$	$CaBr_2$
	$CaBr_2(H_2O)_6$	CaI_2
	$CaI_2(H_2O)_6$	$SrCl_2$
Transition metal halides	$CuCl_2$	$CuBr_2$
	CuI	
Metal organic frameworks (MOFs)	HKUST-1	CPO-27
	UIO-67	ZIF-8

This is most likely due to liquid phase transformations of the material because these materials are known to dissolve in excess amount of water. The hydrated materials also caused much greater dielectric losses than the anhydrous samples, reducing the SNR. For these reasons it was decided not to test the hydrated samples by NPD.

4.2.1 Typical responses

From performing ammonia adsorption experiments on the wide range of materials noted in Table 4.2 some repeatable trends have been observed. Results from CaI_2 (sample mass of 1 g, sample volume of 0.25 cm^3) are shown in this section and the responses are typical of the halide and MOF materials tested.

Figure 4.6 shows the frequency shift and (by extension) the permittivity change of the material due to adsorption of ammonia. As with all the measurements, we take no account of the volume expansion of the sample on ammonia adsorption, which will affect the true materials permittivity. The changes are much larger for those measured for ammonia gas alone, since on adsorption the ammonia becomes more concentrated within the powder. The concentration factor over that of an equivalent volume of gas is found to be 2125 times greater.
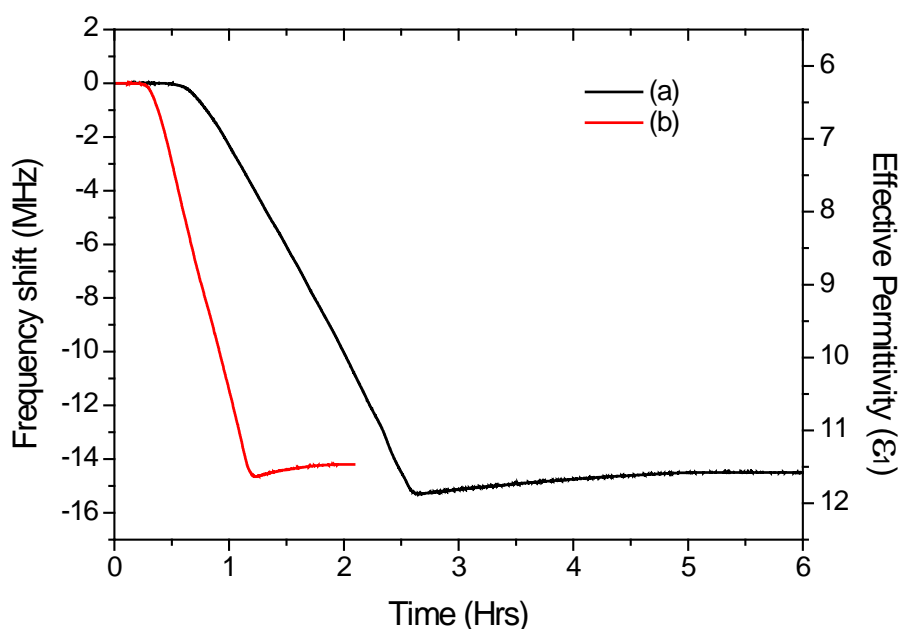
Figure 4.6 – Frequency shift and effective permittivity change of CaI_2 for sample weight and ammonia gas flow rate of 1 g and 5 cm^3/min (a) 1 g and 10 cm^3/min (b).

The change in MCR frequency from Figure 4.6 exhibits a linear response with the ammonia gas adsorption. This is expected because of the increase in ammonia in the MCR measurement space over the duration of the adsorption. The frequency shift ceases at approximately -15 MHz and at this point the material is believed to be saturated with ammonia. This is confirmed from the MS results in Figure 4.7, where ammonia is observed in the out-gas composition shortly after the observed saturation in the MCR results. As seen from Figure 4.6 the gas flow rate determines the rate of the sigmoidal reaction, with the point of saturation occurring approximately at half of the time in 10 cm^3/min flow rate compared in the 5 cm^3/min flow rate. Because the rate of the reaction is limited by the flow rate, all of the ammonia introduced to the sample is adsorbed before saturation. This is also shown in Figure 4.7, where the out-gas composition during the first order reaction consists mainly of nitrogen, i.e. air. Adsorption into the sample causes a pressure drop, as seen in Figure 4.9, in the gas line and therefore leads to the MS aspirating air to maintain sampling pressure.
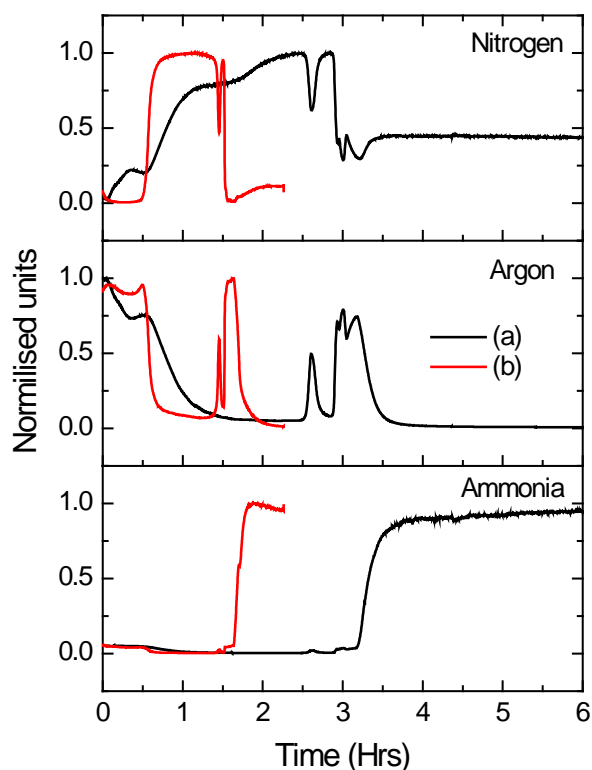
Figure 4.7 – Out-gas compositions of nitrogen, argon and ammonia of CaI$_2$ for sample weight and ammonia gas flow rate of 1 g and 5 cm^3/min (a) 1 g and 10 cm^3/min (b).
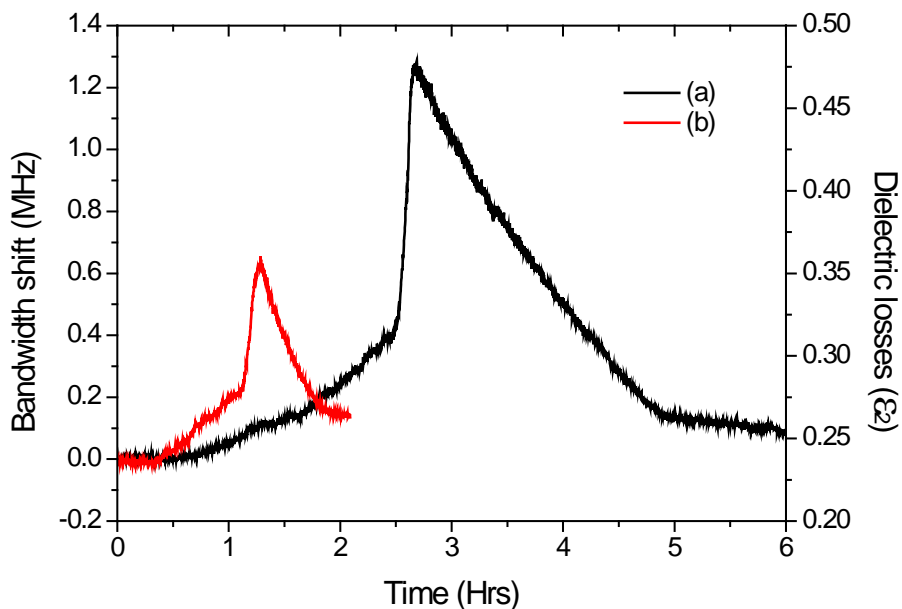
Figure 4.8 – Bandwidth shift and dielectric losses of CaI$_2$ for sample weight and ammonia gas flow rate of 1 g and 5 cm^3/min (a) 1 g and 10 cm^3/min (b).

When saturation occurs, gas flow into the MS is re-established, as seen from the MFM results in Figure 4.9; then, argon gas that had been sitting in the gas line immediately after the sample space is observed in the out-gas composition.
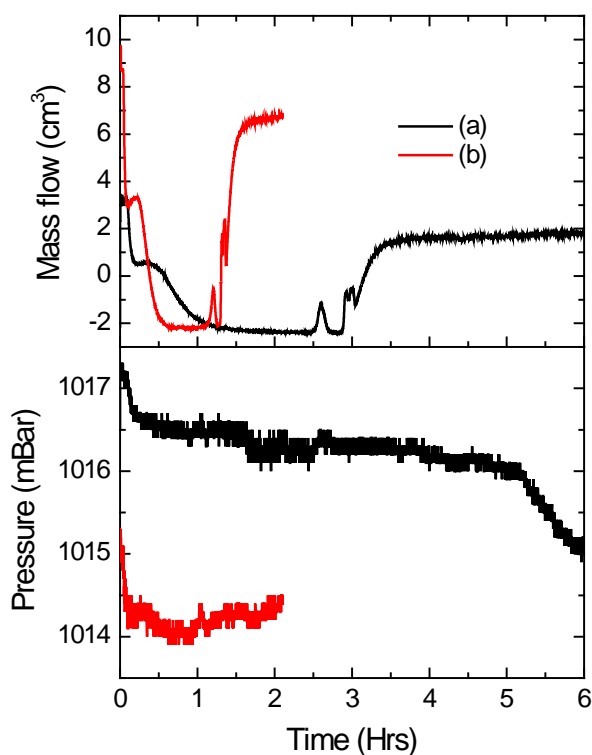

Figure 4.9 – Mass flow and system pressure of CaI$_2$ for sample weight and ammonia gas flow rate of 1 g and 5 cm^3/min (a) 1 g and 10 cm^3/min (b).

The MCR bandwidth change observed during the same experiment is shown in Figure 4.8. This exhibits a general increase, which relates to an increase in dielectric losses as the concentration of ammonia increases within the solid phase. A number of peaks in the dielectric loss were observed as a function of time. These loss peaks could arise from order-disorder transitions between different coordination complexes, or from order-disorder transitions associated with structural transformations. For some materials no dielectric loss peaks have been observed, as with UIO-67 and CPO-27 in appendix 8.4.5; alternatively, multiple loss peaks have been observed as with $MgBr_2$ in appendix 8.4.3.

4.2.2 Analysis and discussion

Even without structural information from the NPD, the MCR and MS measurements can be used to determine the amount of ammonia adsorbed into the sample. An example of this method is shown for $CuBr_2$. Knowing that the first order reaction in the frequency shift data is dependent on the flow rate we can calculate the maximum[1] amount of ammonia adsorbed (mol) by the sample from Equation 4.1. The ($slope$) variable in Equation 4.1 is determined by taking a linear fit of the region where ammonia is being adsorbed at the flow rate as shown in Figure 4.10.

$$mol = \frac{flow\ rate\ \times |\Delta f_{max}|}{slope \times V_m} \qquad \textbf{Equation 4.1}$$

The ($flow\ rate$) is in m³/hr, (f_{max}) is the maximum change in frequency observed by the sample and the molar volume (V_m) is 22.4×10^{-3} m/mol at standard temperature and pressure (STP). By extension, knowing the number of moles of ammonia adsorbed into the material (mol), the mass of sample (m) and the molar mass of the sample (M), these can then be used to calculate the amount of ammonia per unit formula in the material $(NH_3)_x$, as shown in Equation 4.2.

---

[1] The maximum amount of ammonia absorbed is likely to include surface level adsorption, which is not retained when ammonia gas flow is removed.
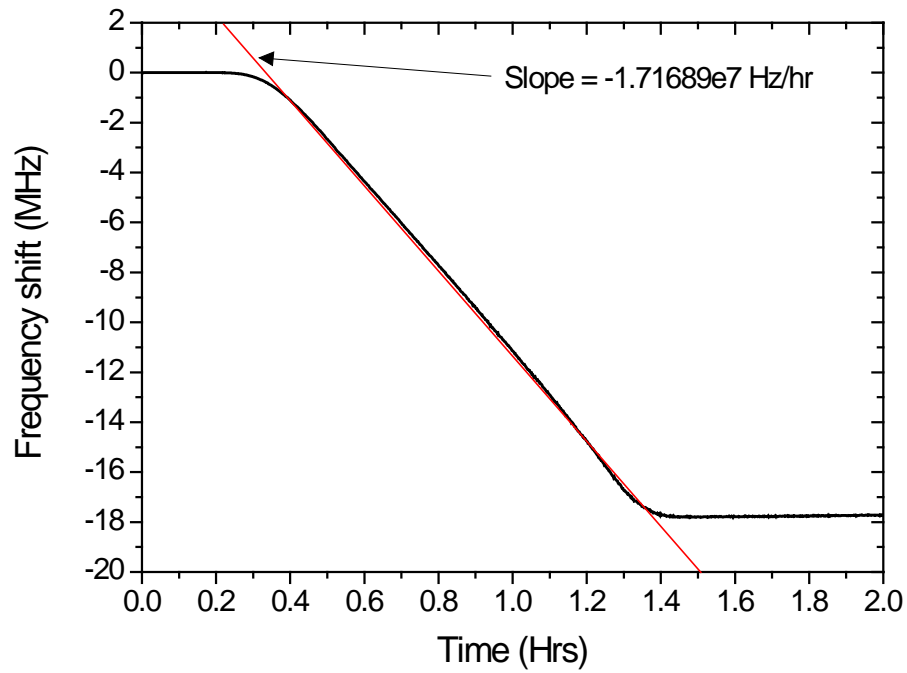
$$(NH_3)_x = \frac{mol \times M}{m}$$ **Equation 4.2**

Figure 4.10 – Frequency shift of CuBr$_2$ for sample weight and ammonia gas flow rate of 1g and 10cm^3/min, showing the slope of the linear fit of the first order reaction.

Using the results from the MS data, the same analysis can be performed as with the MCR data.

If we make the assumption that the only gaseous inputs to the system are argon and ammonia

from the input gas lines and air from the MS, we can assume that the amount of air observed

in the out-gas is directly related to the amount of ammonia being adsorbed by the material.

We can then calculate the molar volume of ammonia gas adsorbed in the sample by summing

the nitrogen content in the out-gas as shown in Figure 4.11. The formula to calculate this is

shown in Equation 4.3, with (v_i) being the normalised gas volume measured and (τ) is the

sampling period of the MS.

$$mol = \frac{\tau \times flow\ rate}{V_m} \sum_{T_1}^{T_2} (v_i)$$ **Equation 4.3**
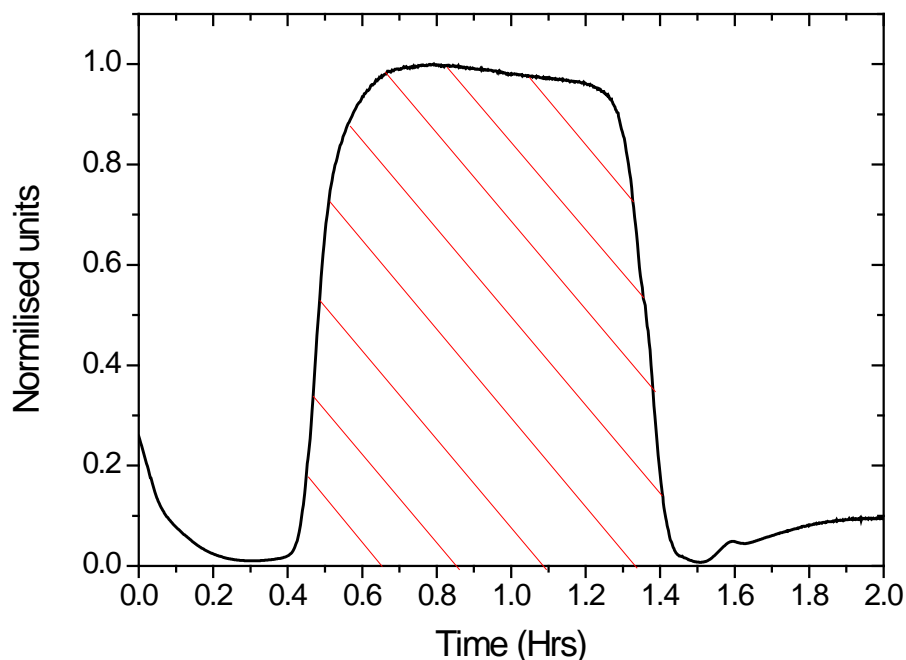
Figure 4.11 – Out-gas compositions of nitrogen for CuBr$_2$ for sample weight and gas flow rate 1g and 10cm^3/min, the shaded area indicating when gas adsorption occurs.

The ammonia per unit formula can also be calculated from the MS data using Equation 4.2. The amount of ammonia adsorbed and ammonia per unit formula are shown in Table 4.3 for a range of tested materials, calculated from both the MCR data and MS data. Because the masses of the materials tested are approximately the same, we can see from Table 4.3 that the amount of ammonia adsorbed into the material is directly related to the molar mass of the material.

This fits with what is expected from previous studies, which showed that MgCl$_2$ and CaCl$_2$ have the most desirable percentage weight of ammonia (Elmøe et al., 2006) (Gillespie & Gerry, 1931). The ammonia adsorbed follows the same trends as for the MCR and MS calculations; however, there is an offset between the two results which has most likely arose from errors in the linear fit and summation limits (T_1) and (T_2) in the MS results. The ammonia per unit formula for a range of halide materials have been deduced from previous studies (Aoki et al., 2014) (Poonia & Bajaj, 1979).

Table 4.3 – Calculated number of moles of adsorbed ammonia and adsorbed ammonia per unit formula from MCR results and MS results for a range of materials.

Material (1g)	Moles adsorbed from MCR data	$(NH_3)_x$	Moles adsorbed from MS data	$(NH_3)_x$	Predicted $(NH_3)_x$
$MgBr_2$	0.042	7.728	0.031	5.704	6
MgI_2	0.0265	7.367	0.0238	6.616	6
$CaBr_2$	0.038	7.609	N/A	N/A	8
CaI_2	0.024	7.056	0.0232	6.821	8
$CuBr_2$	0.0279	6.222	0.0249	5.562	6
CuI	N/A	N/A	0.0198	3.767	3

The results shown in Table 4.3 do not yield to integer coordinations as might be expected, but this will be due to the differences in sample quantity, as discussed in section 4.1.3. Also it is possible that ammonia gas is not fully permeating into the powdered material, so that pockets of material were left uncoordinated. The results still tend to suggest that most materials achieve maximum coordination complexes with molar ratios of 6:1 or 8:1, in agreement with others (Westman et al., 1981) (Johnsen et al., 2014). However there is still an error of around 20% from the recorded results and the predicted results from the known coordination's observed from these materials.

4.3 Alkali earth halides

The preferable alkali earth halides to test in the NPD are $MgCl_2$ and $CaCl_2$ as they have shown the most promise in ammonia storage techniques (Sørensen et al., 2008). However for the reasons discussed in section 4.2, these materials were not suitable to test in the current system. Instead MgI_2 (99.998% purity from Sigma-Aldrich) and $CaBr_2$ (99.5% purity from Alfa Aeser) were tested as these materials are expected to have similar properties to their chloride counterparts. Due to the microwave adsorbing nature of the halide materials in the MCR, the sample quantity should be relatively low to retain high SNR in measurements. Conversely, a larger sample quantity is needed to retain a high SNR for NPD measurements. A sample quantity of 1.5 g was used as a compromise between the two technique requirements. Because the NPD captured data in 2 minute segments, the gas flow rate was set as low as possible (5 cm^3/min) to give the maximum possibility of recording any intermediate or transient change in the materials.

4.3.1 Thermal analysis results

TGA and DSC are common techniques to assess ammonia storage materials. These techniques can be used to give insight into adsorption and desorption and gravimetric density of ammonia (Bialy et al., 2015) (Huang et al., 2010). TGA and DSC was conducted separate from the simultaneous measurement of MCR and NPD. The experimental setup is similar to the setup shown in Figure 2.20 and a NETZSCH STA 449 F3 TGA was used. In these experiments the same anhydrous beads for MgI_2 and powder for $CaBr_2$ were used as in NPD experiments. A protective gas flow of nitrogen at 20ml/min was applied to protect the components from ammonia corrosion. The gas flow path was directed from below the sample and crucible up to the gas exit. This means the material is not directly in the path of the gas flow. Therefore not all the gas is exposed to the sample and there is the possibility that not all of the sample undergoes full ammonia uptake.
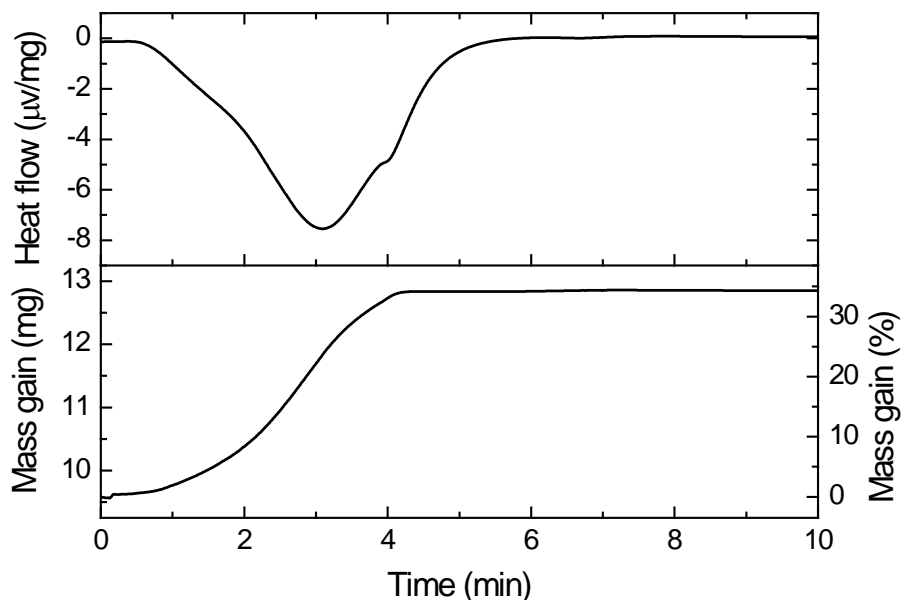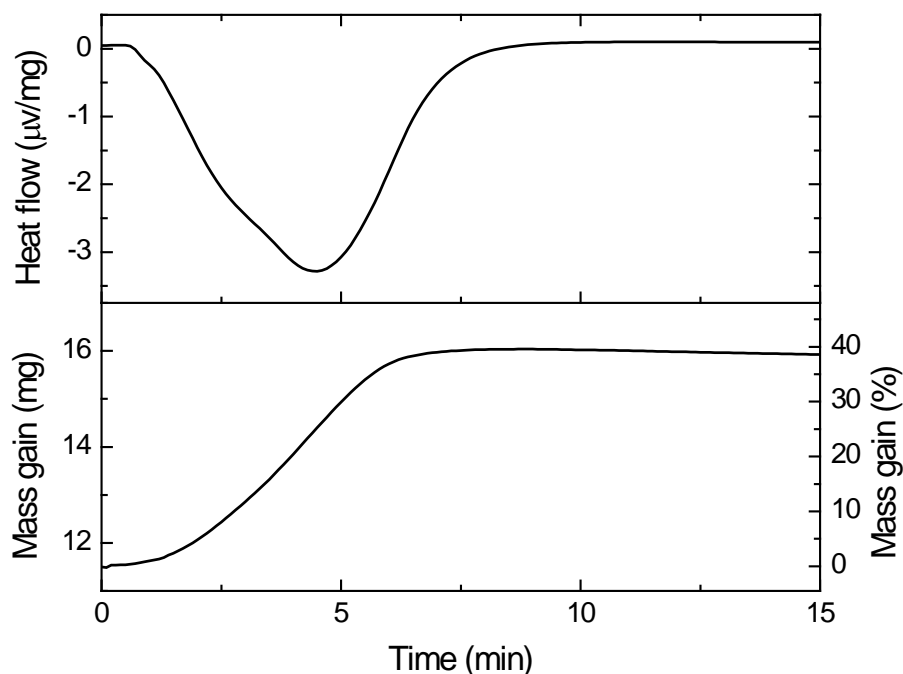
Figure 4.12 – Heat flow and mass change of MgI$_2$ for sample weight and ammonia gas flow rate of 9.57 mg and 20 ml/min.

The TGA and DSC results for ammonia adsorption of 9.57 mg of MgI$_2$ are shown in Figure 4.12. The adsorption of MgI$_2$ occurs sigmoidally until the material saturates with ammonia. The ammonia per unit formula was calculated from the mass gain results, yielding a result of 5.6. This is not known as a stable complex of MgI$_2$. This is probably due to some of the material not being exposed to the ammonia gas flow, or an error in measuring mass due to calibration.
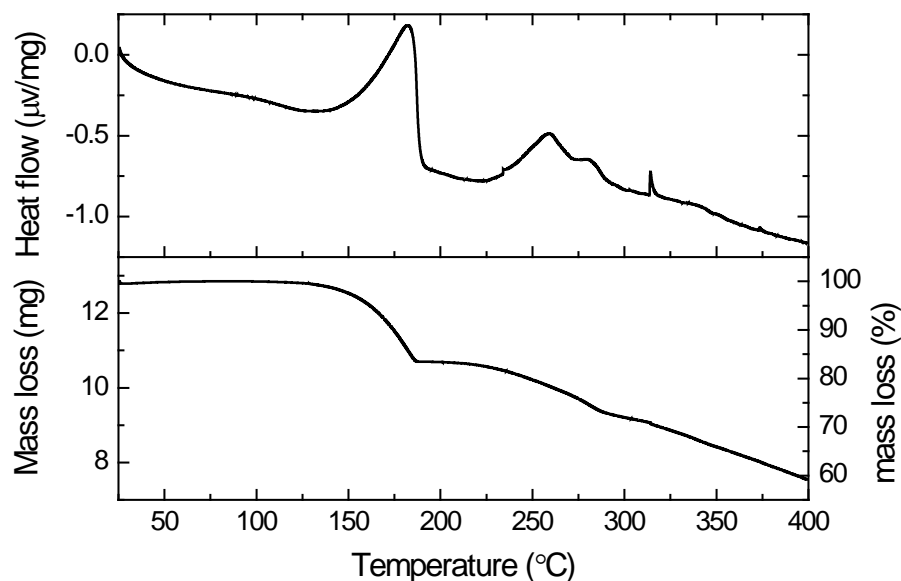
Figure 4.13 – Heat flow and mass change of MgI$_2$(NH$_3$)$_x$ under a heating profile of 3 k/min.

Figure 4.14 – Heat flow and mass change of CaBr$_2$ for sample weight and ammonia gas flow rate of 11.5 mg and 20 ml/min.

The DSC results show an exothermic peak for the adsorption of ammonia into MgI$_2$. However, at a time of four minutes in the adsorption process, there is a variation in the exothermic peak shape, possibly indicating another exothermic event. The desorption characteristics of MgI$_2$ are shown in Figure 4.13. The mass drops throughout the duration of the experiment and it is believed that after 310 °C the material starts decomposing from MgI$_2$ into other products. Two coordinated phases can be seen from the mass loss results; the starting phase and another phase at 200 °C. Assuming the mass at 310 °C is just MgI$_2$ then the two distinct phases seen are MgI$_2$(NH$_3$)$_{2.34}$ and MgI$_2$(NH$_3$)$_{6.06}$. This approximately fits the coordination complexes of two and six observed in previous studies (Jones et al., 2013). The DSC results also show two endothermic peaks between 250-300 °C, which suggests there is another coordination complex, most likely MgI$_2$(NH$_3$), but this phase will have very similar enthalpy of formation to that of the coordination of two.
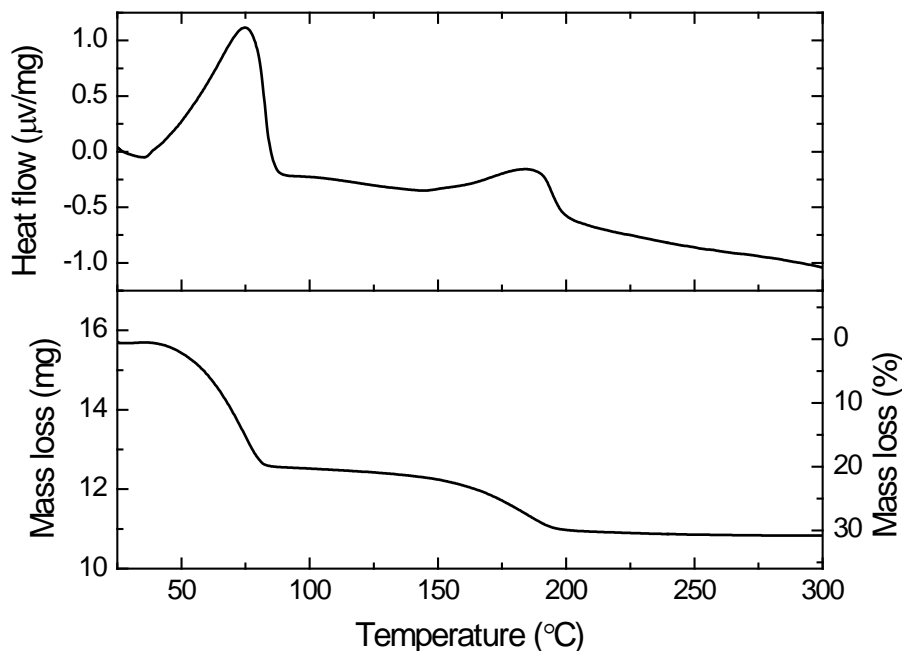
Figure 4.15 – Heat flow and mass change of CaBr$_2$(NH$_3$)$_x$ under a heating profile of 3 k/min.

The ammonia adsorption of 11.5 mg of CaBr$_2$ shows similar results as for the MgI$_2$ sample in TGA measurements, as shown in Figure 4.14. The DSC measurement from Figure 4.14 shows an exothermic peak, but in this situation the asymmetry in the peak shape appears earlier than for MgI$_2$. This indicates that there are exothermic events during the adsorption process, rather than at saturation. The desorption results shown in Figure 4.15 show two phases of CaBr$_2$(NH$_3$)$_x$. The DSC results show the temperatures of these phase changes with endothermic peaks from the transition from one phase to another. The mass lost during the experiment exceeds the starting reactants (11.2 mg – 10.8 5mg). It is not believed that the CaBr$_2$ material decomposes as in the MgI$_2$ sample but this difference in mass may be due to the material having been partially hydrated prior to ammonia adsorption. Assuming that the final recorded mass from the TGA results is CaBr$_2$ only, then the ammonia per unit formula for the two coordinated phases corresponds to CaBr$_2$(NH$_3$)$_{1.81}$ and CaBr$_2$(NH$_3$)$_{5.34}$. These results will be subject to the same errors in measurement as previously mentioned. However, assuming a 12% systematic error in measurement, the ammonia per unit formula for the two phases is then consistent with CaBr$_2$(NH$_3$)$_2$ and CaBr$_2$(NH$_3$)$_6$, which are valid complexes observed in other halide materials (Patil & Secco, 1971) (Iwata et al., 2014).

4.3.2 Dielectric results

The first material tested within the simultaneous measurement system was MgI_2. The experimental setup and procedure is the same as detailed in sections 4.1.1 and 4.1.2. The sample was in anhydrous bead form and deuterated ammonia gas was used. The results of frequency shift and effective permittivity change for ammoniated MgI_2 are shown in Figure 4.16. It takes 40 minutes for the gas in the system to reach the sample and this is when a dielectric change in the material is observed. The change in frequency is approximately sigmoidal, like that in the preliminary measurements and TGA measurements until saturation, which occurs at 4.2 hours. At 7.2 hours the deuterated ammonia gas flow was switched back to the argon gas flow. Because of this, at 8 hours into the experiment there is a positive frequency shift of 1 MHz, suggesting ammonia is leaving the measurement space. This is expected due to the replacement of ammonia gas with argon gas, but as shown from Figure 4.3 the gas replacement contributes approximately 350 kHz to the frequency shift. The remaining 650 kHz change is believed to be from the removal of physisorbed ammonia from the material. Therefore we can conclude that the ammonia adsorption process of MgI_2 consists of 4.9% physisorbed or surface level ammonia.

By preforming the analysis methods discussed in section 4.2.2 on the frequency data using Equation 4.1 and Equation 4.2, the amount of ammonia adsorbed can be obtained. At 4.2 hours 0.0482 moles had been adsorbed, which relates to an ammonia complex of 8.94 per unit formula. Accounting for the release of ammonia after argon was applied, this leaves the moles adsorbed and ammonia per unit formula at 0.0447 and 8.29, respectively, which suggests that the saturation coordination complex of MgI_2 is eight. The excess amount is probably from physisorbed ammonia which is not released when argon is reflowed over the sample.
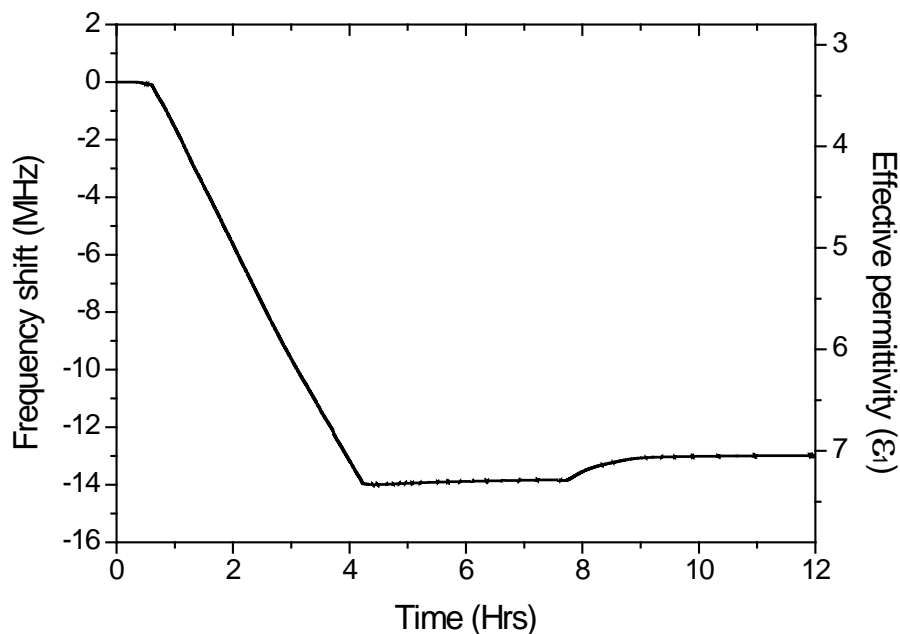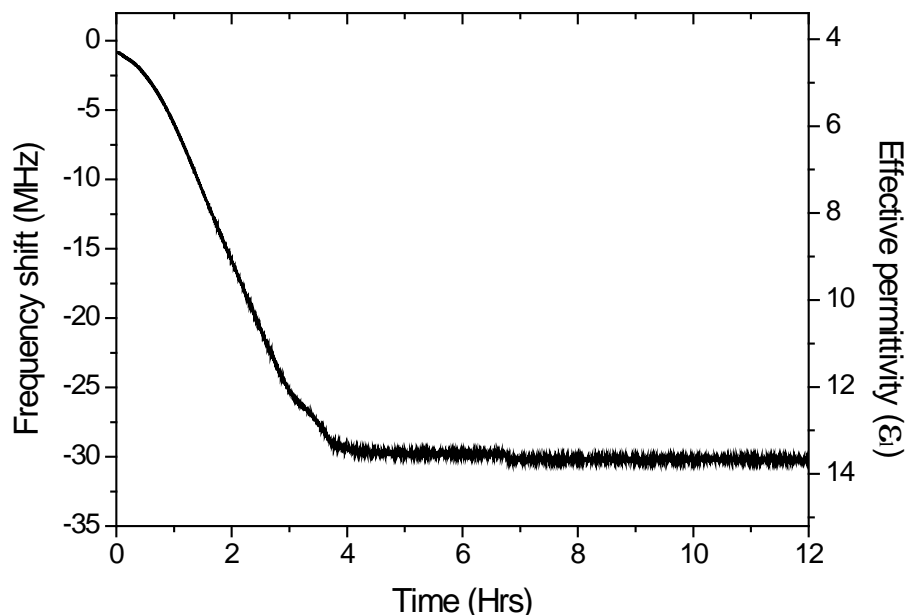
Figure 4.16 – Frequency shift and effective permittivity change of MgI$_2$ for sample weight and ammonia gas flow rate of 1.5 g and 5 cm^3/min.

The idea of the presence of physisorbed ammonia is supported by the change in bandwidth and dielectric losses shown in Figure 4.17, where at 8 hours there is a dramatic reduction in the bandwidth of the resonance. This bandwidth change is much more pronounced than the frequency shift, a change of 79.4%. This is expected because the dielectric losses are highly influenced by the rotational freedom of the ammonia molecule (Davies, 1954), (Fish et al., 1958), which itself is dependent on the binding energy to the host halide material. The chemisorption process of ammonia is from L-type ligand bonding and this has lower enthalpies to that of covalent bonding, typically in range of 20-50 kcal/mol (Bauschlicher et al., 1995), (Chan, 1999). We believe this ligand bonding is not the main contributor to dielectric losses because the metal to nitrogen bond still gives the ammonia molecule relative freedom of rotation. The bulk of the dielectric losses in chemisorbed ammonia will come from the hydrogen bonds (or in this case deuterium bonds) between the ammonia molecules in the halide lattice.
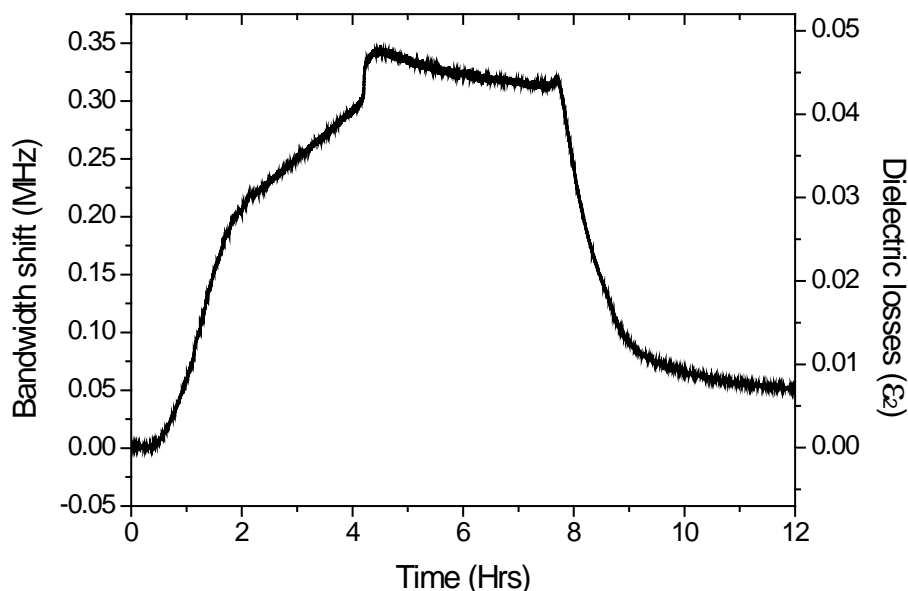
Figure 4.17 – Bandwidth shift and dielectric losses of MgI$_2$ at sample quantity and ammonia gas flow rate of 1.5 g and 5 cm^3/min.

Physisorbed ammonia tends to have lower enthalpies than that of chemisorbed ammonia. However, this process is highly influenced by hydrogen bonding of the ammonia to the bulk material. Hence we believe this will contribute more to the dielectric losses than the chemisorption processes and so this is the reason for greater bandwidth changes (Atkins, 1990).

The bandwidth shift in Figure 4.17 differs from the first order response in the frequency shift. The reason for this is not fully understood because the structural analysis in section 4.3.4 does not shed any light on what is happening. A possible reason for the change in the rate of bandwidth shift from 0.6-2 hours to 2-4 hours might be related to the change in the exothermic peak shape in Figure 4.12, where the variation in peak shape might indicate change in the adsorption kinetics. This is seen at saturation, where in the dielectric results there is a sharp jump in bandwidth and in the DSC result there is an exothermic event.

Figure 4.18 – Frequency shift and effective permittivity change of CaBr$_2$ for sample weight and ammonia gas flow rate of 1.5 g and 5 cm^3/min.

The second material tested was CaBr$_2$. In this experiment the neutron beam was shut off shortly after the ammonia gas flow was switched from argon gas flow. In this case the gas flow was stopped. When the beam was re-established gas flow was resumed. In Figure 4.18 the zero time is when the gas flow was resumed. Therefore there is little to no delay in the time it takes for ammonia gas to reach the sample and the frequency shifts sooner than for the MgI$_2$ results. The frequency shift in CaBr$_2$ follows the same trends as for the MgI$_2$ sample. The CaBr$_2$ frequency shift does have some second order components, but this is from the bandwidth shift in Figure 4.19, since the real and imaginary parts of the permittivity should be coupled in the usual way by the Kramers-Kronig relations (Roessler, 1965) (Lovell, 1974). Unfortunately in this experiment the sample blocked the gas flow, so that at 4 hours into the experiment the frequency shift ceases. This may be due to saturation in the material or from the blockage preventing access to unammoniated material. Due to the lower molar mass of CaBr$_2$ it is expected that CaBr$_2$ will adsorb more moles of ammonia than MgI$_2$ (Kubota et al., 2014).
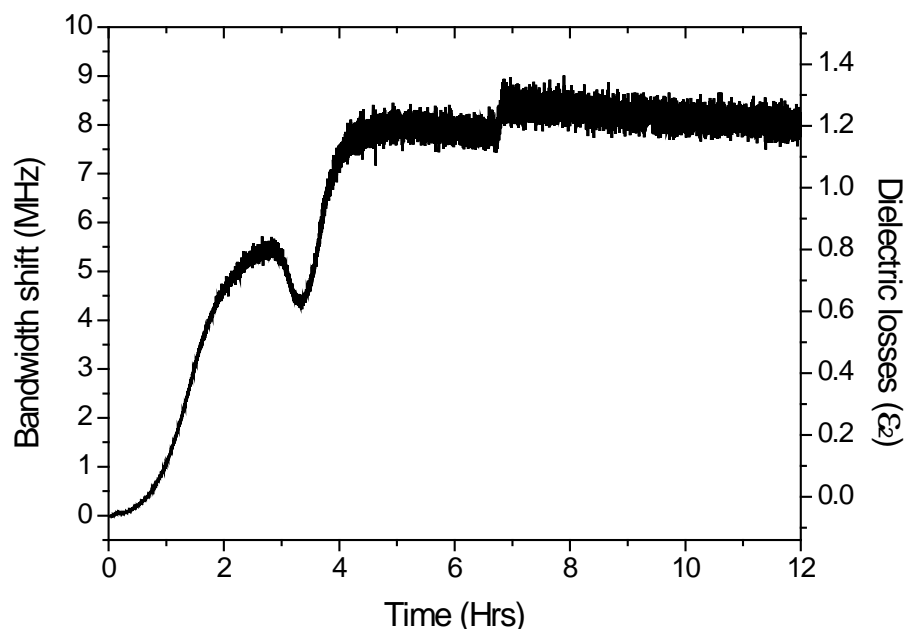
Figure 4.19 – Bandwidth shift and dielectric losses of CaBr$_2$ for sample weight and ammonia gas flow rate of 1.5 g and 5 cm^3/min.

This longer adsorption time (approximately 1.5 times longer than MgI$_2$) has been observed in preliminary measurements, shown in appendix 8.4.3, which suggests there is unammoniated material in the CaBr$_2$ sample. This theory is supported by the calculations of the number of moles of ammonia adsorbed and ammonia per unit formula which are 0.041 and 5.45, respectively. These are significantly lower than the result for CaBr$_2$ shown in Table 4.3. Due to the blockage in the gas flow system the gas flow had to be shut off at 6 hours and argon was not reflowed over the sample.

The bandwidth shift shown in Figure 4.19 follows the same trend as in the frequency shift for the first 2 hours. Then another phenomenon influences the bandwidth shift. This produces prominent loss peaks, which have been seen numerous times in the preliminary experiments. In this case, the origin of the features in the bandwidth data can be related to the structural data in section 4.3.4 and the relationship between the two sets of data is discussed in more detail in section 4.3.5. The bandwidth data becomes noisier as the experiment progresses. This is because the measurement signal is being adsorbed as there is a greater amount of ammonia in the measurement space.

4.3.3   Mass spectrometry and mass flow results

The measurement of out-gas compositions by mass spectrometry in integrated measurement systems has been previously used to provide information on a wide range of chemical processes involving ammonia (Topsoe et al., 1995) (Cumaranatunge et al., 2007). However the out-gas composition does not provide direct information on the properties of the sample, rather the products, or lack of from the processes occurring in the sample. A MS can still provide valuable complementary information on the reaction processes involved in these experiments. Because the MS is placed further down the gas line, as displayed in Figure 4.1, there is a 40 minute delay between the same phenomena observed in the dielectric and structural data to the mass spectrometry data.
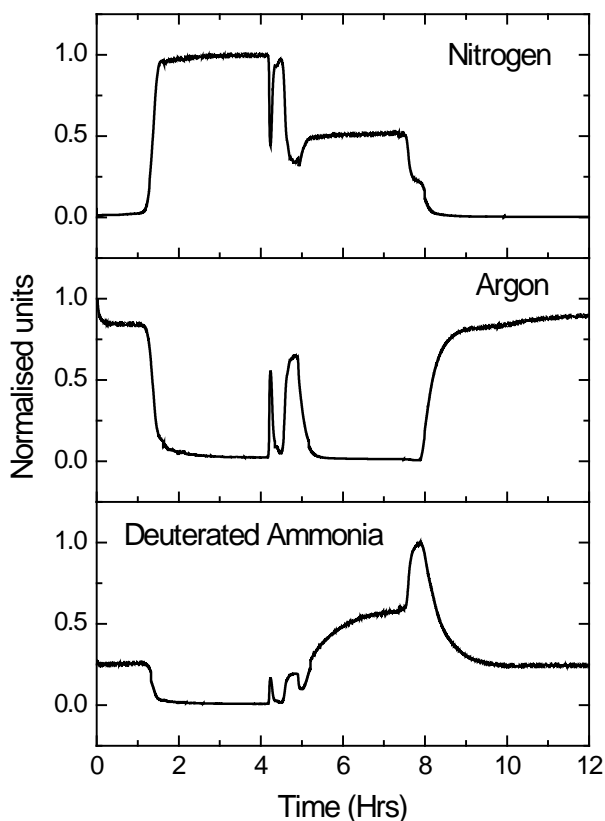
Figure 4.20 – Out-gas compositions of nitrogen, argon and ammonia of MgI$_2$ for sample weight and ammonia gas flow rate of 1.5 g and 5 cm^3/min.

The results from the MS for ammonia adsorption by MgI_2 are shown in Figure 4.20. Initially argon is shown in the out-gas, as expected due to the purging of the system prior to the experiment. As ammonia is flowed through the system the argon is removed from the system and nitrogen is observed in the out-gas. As with the preliminary results in section 4.2.1 this is due to ammonia being adsorbed in the material and the MS aspirating air to maintain sampling pressure. Until 4.2 hours into the experiment no ammonia is observed exiting the system. This relates to the dielectric results in Figure 4.16, which indicates ammonia adsorption until 4.2 hours or saturation in the material. Due to the material's ability to adsorb ammonia completely the material can be used in ammonia trapping methods such as filters (Britt et al., 2008). After 4.2 hours the remaining argon gas that has been sitting in the system between the sample and MS exits the system. After the argon is completely removed ammonia is then observed in the out-gas.
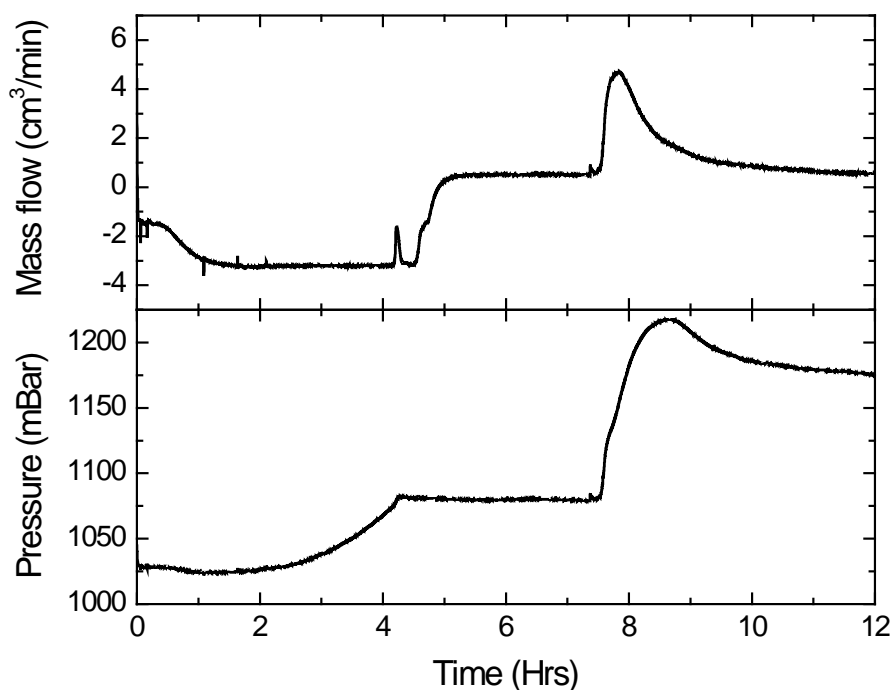
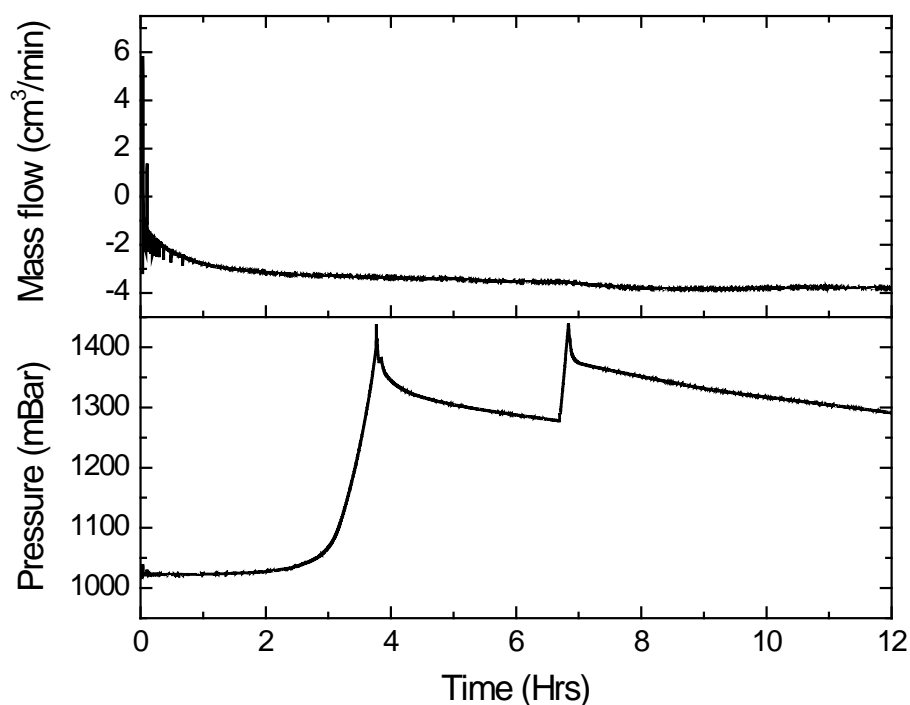**Figure 4.21 – Mass flow and system pressure of MgI$_2$ for sample weight and ammonia gas flow rate of 1.5 g and 5 cm^3/min.**

The amount of ammonia observed in the out gas will tend to an asymptote if the gas flow is not changed. At 7.2 hours the gas flow was switched back to argon. Instead of observing the reintroduction of argon back into the out-gas, an excess of ammonia is observed. This is due to the physisorbed ammonia being released from the sample, from the change in ammonia to argon atmosphere at the sample. This excess ammonia release lasts approximately 40 minutes, then argon gas is observed in the out-gas.

The molar volume of ammonia adsorbed was assessed using the methods discussed in section 4.2.2 and the ammonia adsorbed and ammonia per unit formula was determined from Equation 4.3 and Equation 4.2. Similar to the results shown in section 4.3.2, the calculated ammonia adsorbed at saturation was 0.0455 and the ammonia per unit formula was 8.43. Removing the excess ammonia observed when argon was reflowed, the values come to 0.0425 and 7.87 respectively. These are slightly lower than the results from the calculations based on the MCR's resonant frequency, but still suggests a maximum ammonia content of eight in the MgI_2 sample.

Figure 4.22 – Mass flow and system pressure of $CaBr_2$ for sample weight and ammonia gas flow rate of 1.5 g and 5 cm^3/min.

The results in Figure 4.21 show the mass flow and pressure of the system for the MgI_2 ammonia adsorption experiment. Because the MFM is not calibrated to a single type of gas composition and the gas flow rate is around its minimum sensing level, the values are not indicative of the true mass flow occurring in the system. However, the trends do contribute to the previous results of excess ammonia leaving the system when argon gas is reflowed, as both the mass flow and pressure increase in accordance with the increase in ammonia gas in the system. Because of the blockage to the system in the $CaBr_2$ run, the mass spectrometry data does not yield any useful information on the process of ammonia adsorption into the material. Similarly, the mass flow data shown in Figure 4.22 indicates that there is little to no out-gas contribution to the MS. Additionally, the pressure in the system, shown in Figure 4.22, does show how the gas flow is restricted by the blockage, with the pressure spiking at 4 hours, when the gas flow was switched off. After the 4 hour mark the pressure begins to drop. This may be due to ammonia still slowly percolating through the material and being adsorbed, or more likely due to ammonia escaping through leaks in the system. At 6.8 hours the ammonia gas flow was briefly re-established to check if the system could become unblocked, but the pressure spiked as before.

4.3.4 Neutron powder diffraction results

It was found that the clearest quality of NPD results for both MgI_2 and $CaBr_2$ was from the bank 4 (90°) detectors. The time resolved diffraction patterns for all the other diffraction banks are shown in appendix 8.6.1. Figure 4.23 shows the diffraction peaks for ammonia adsorption into MgI_2. The diffraction peaks that are visible at time zero are from the aluminium MCR, as shown in Figure 4.4, and are constant for the duration of the experiment. Diffraction peaks from MgI_2 are not seen at the start of the experiment because the material only occupies approximately 20% of the beam height and the capture time is only in 2 minute segments.
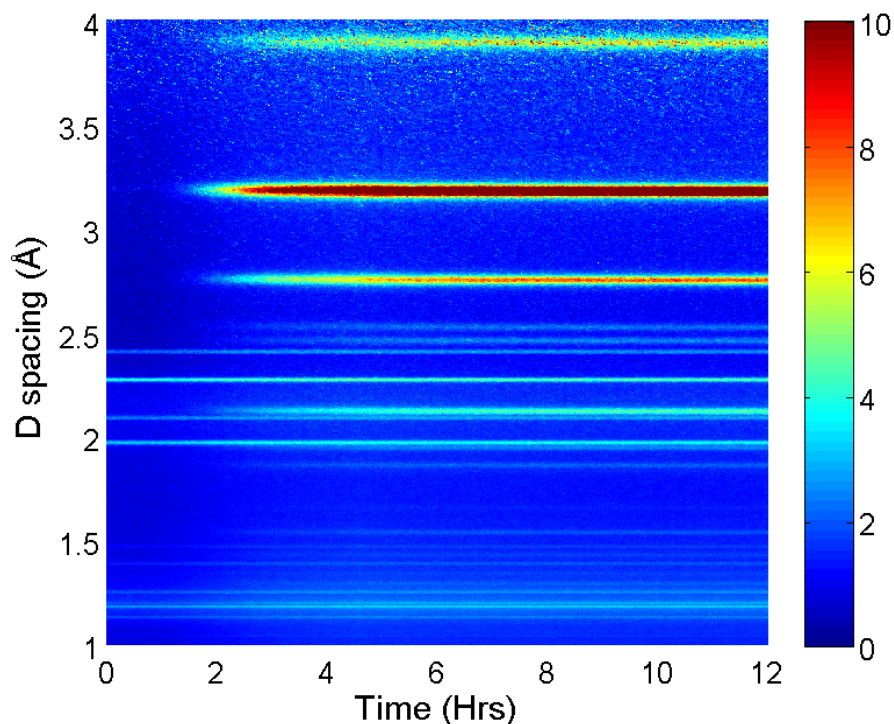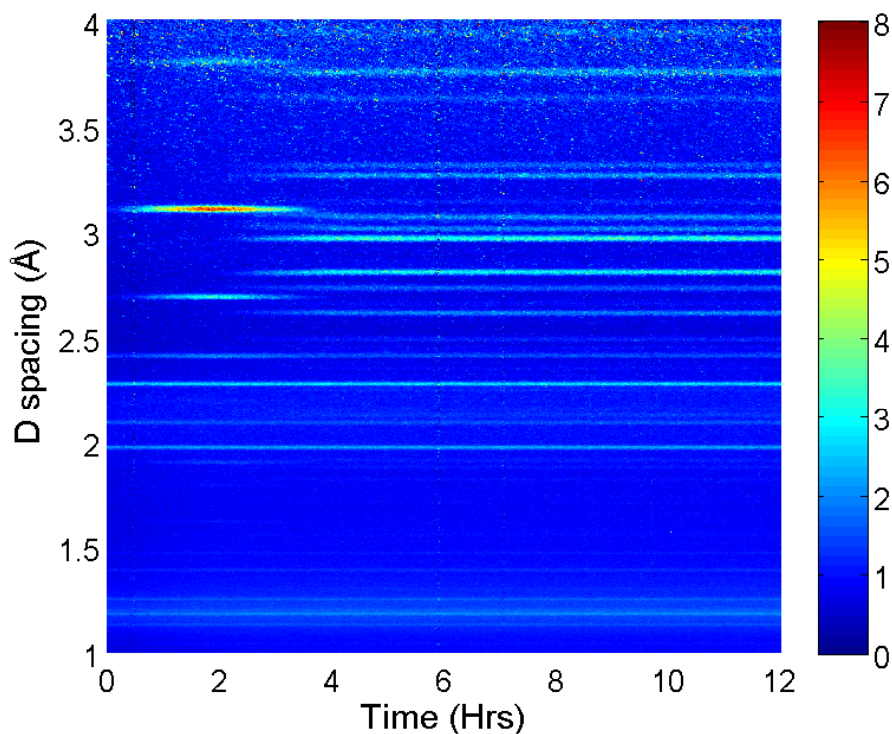
Figure 4.23 – Diffraction peaks from bank 4 (90° detectors), showing neutron count in colour intensity for MgI$_2$ for sample weight and ammonia gas flow rate of 1.5 g and 5 cm^3/min.

As the deuterated ammonia is adsorbed by the sample, peaks begin to appear due to the diffraction from the deuterium, which has a relatively high neutron scattering cross section of 5.592 b (Sears, 1992). The strength of these diffraction peaks also increases due to the expansion of the sample in the quartz tube and thus a greater percentage of the neutron beam is in the path of the sample. The rate of this expansion is not measured, but at the end of the experiment the MgI$_2$(NH$_3$)$_x$ sample occupies 6 cm of the quartz tube, three times greater than the beam height. The evolution of these new diffraction peaks follow similar trends to other in-situ NPD measurements of various chemical reactions, where there is a compositional or structural change from one material to another (Walton et al., 2001), (Mcintosh et al., 2006). The diffraction data shows that the ammonia adsorption forms one phase. This is unexpected as the TGA in Figure 4.13 shows that there are multiple viable complexes for MgI$_2$(NH$_3$)$_x$ and previous studies show there is MgI$_2$(NH$_3$)$_1$, MgI$_2$(NH$_3$)$_2$ and MgI$_2$(NH$_3$)$_6$ structures (Jones et al., 2013) (Leineweber et al., 1999). The results suggest that MgI$_2$ does not form these lower order complexes in the presence of excess ammonia at STP, but instead goes straight to forming its maximum coordination complex.

Figure 4.24 – Diffraction peaks from bank 4 (90° detectors), showing neutron count in colour intensity for CaBr$_2$ for sample weight and ammonia gas flow rate of 1.5 g and 5 cm^3/min.

The NPD results from the CaBr$_2$ sample tell a very different story to the MgI$_2$ sample. In this case a phase transition is observed in the sample, shown in Figure 4.24. For the first 2 hours the ammonia is adsorbed into an initial phase and between 2-4 hours the material transitions to a second higher order coordination complex. This process of formation and deformation of intermediate phases from lower order complexes to higher order complexes has been observed in hydration experiments using similar in-situ neutron diffraction techniques (Ting et al., 2009). The results in Figure 4.24 agree well with the ex-situ results from TGA and DSC in Figure 4.15, which show two distinct phases of ammoniated CaBr$_2$.

4.3.5   Correlation between MCR and NPD results

The nature of simultaneous measurement means that direct correlation between change in dielectric properties and structural changes can be compared with confidence. Both MgI$_2$ and CaBr$_2$ show a general increase in permittivity and dielectric losses as ammonia is introduced to the samples. Previous experiments on the hydration of materials have shown the same general increase for adsorption of water into a material (Bone et al., 1977).

In this case the rate of adsorption of ammonia (similar to the adsorption of water) correlates well with the change in permittivity and the evolution of Bragg peaks from the NPD results. This effect is seen in Figure 4.25, where in the MgI_2 sample the change in frequency shift follows the same trend (apart from a small lag between results) as the neutron scattering intensity at 3.17Å, where a Bragg peak forms. This correlation between frequency data and NPD fits well when there is a first order reaction occurring in the sample. However, when there are other reaction steps occurring in the sample, as with the $CaBr_2$ sample, the frequency data alone does not provide all the necessary information.

For the $CaBr_2$ sample the NPD data showed a phase change in the material. The dynamics of this phase change can be seen in Figure 4.26, where the intensity of two Bragg peaks, one from each phase, are shown. Figure 4.26 also shows the change in bandwidth recorded and the features in the bandwidth correlate very well with changes in intensities from one phase to another. Dielectric losses are known to vary quite dramatically with phase changes in materials (Zou et al., 2008).
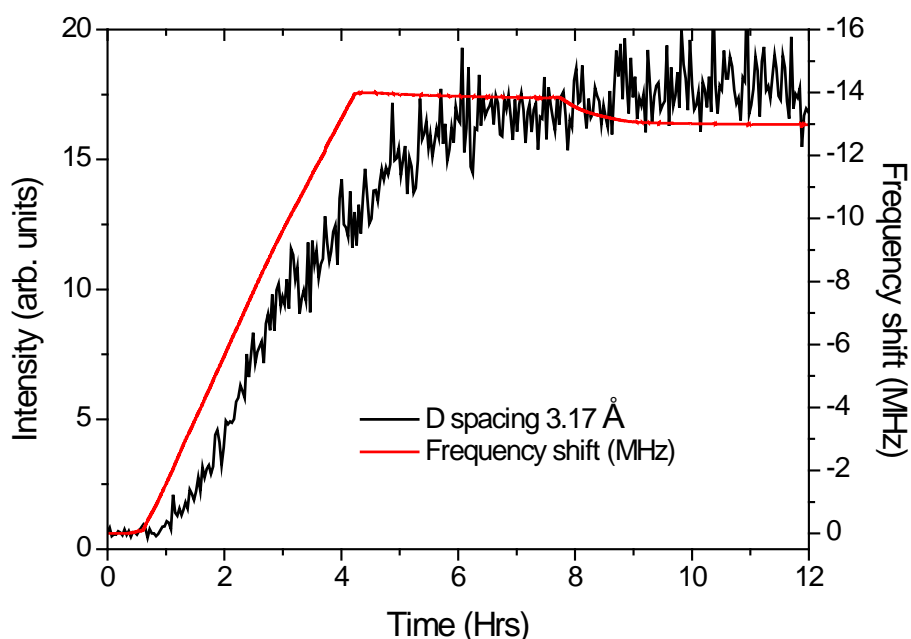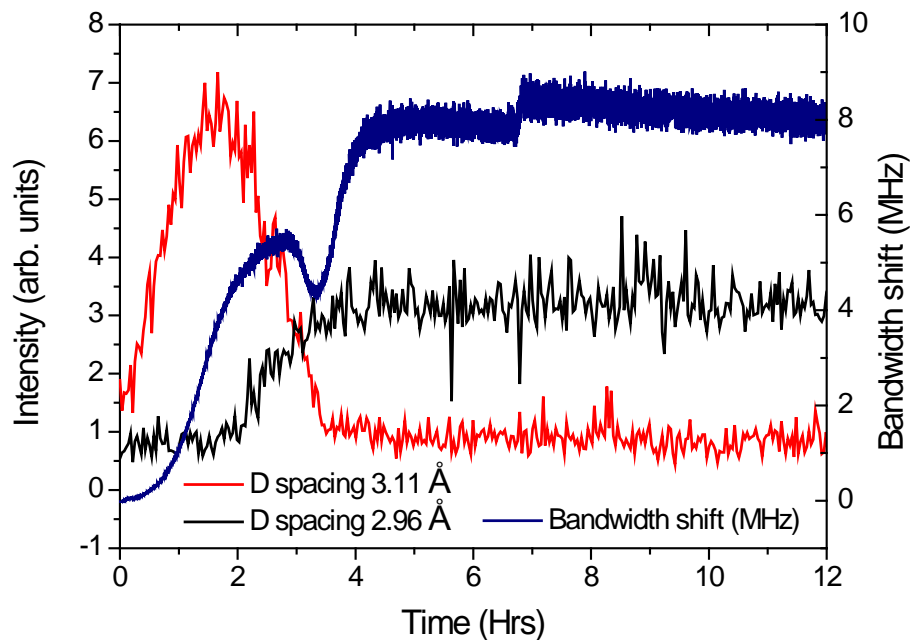

Figure 4.25 – Comparison between frequency shift of MCR and intensity in diffraction peak of NPD in MgI$_2$ for sample weight and ammonia gas flow rate of 1.5 g and 5 cm^3/min.

The Bragg peaks shown relate to the hydrogen-hydrogen bonds (or in this case deuterium-deuterium bonds) in the material. As the material undergoes this phase change the H-H bonding will break and then reform at different bond lengths as shown. This process will therefore cause an order-disorder transition in the material (Desiraju & Steiner, 1999). The change in dielectric losses have been observed for various different forms of order-disorder transitions. These transitions can cause sharp changes in the dielectric losses and even dielectric loss peaks, that have been widely observed in preliminary measurements (Akutagawa et al., 2004) (Śanchez-Anđujar et al., 2010). In the case of $CaBr_2$ the breaking of these H-H bonds causes the ammonia molecule to more easily rotate to maintain its orientational polarisation (as discussed in section 2.4.1) and thus less energy is lost in doing so. This is why there is a decrease in the bandwidth while the material undergoes the order-disorder transition. When the Bragg peak from the initial phase disappears completely the bandwidth beings to increase again. This is due to the ammonia still being adsorbed into the material, but also from the formation of new H-H bonds in the new phase.

Figure 4.26 – Comparison between Bandwidth shift of MCR and intensity in diffraction peaks of NPD in CaBr$_2$ for sample weight and ammonia gas flow rate of 1.5 g and 5 cm^3/min.

4.4 Transition metal halides

Various different types of transition metal halides have been investigated for their ammonia adsorption properties (Reardon et al., 2012) (Leineweber & Jacobs, 2000). In this section $CuBr_2$ (99% purity from Alfa Aesar) and CuI (99.99% purity from Sigma Aldrich) were tested under the experimental conditions detailed in section 4.1. $CuCl_2$ was unable to be tested due to the same reasons of quartz tube breakage as with other chloride compounds. The same sample quantity and gas flow rate of 1.5 g and 5 cm^3/min were used in these experiments, so that meaningful comparisons could be made with the results in section 4.3.

4.4.1 Thermal analysis results

As in section 4.3.1, TGA and DSC were conducted separatly from the simultaneous measurement system, with the same experimental setup. The ammoniation of $CuBr_2$ is shown in Figure 4.27. This has a similar adsorption characteristic to MgI_2 with a secondary exothermic peak around the saturation of the material.
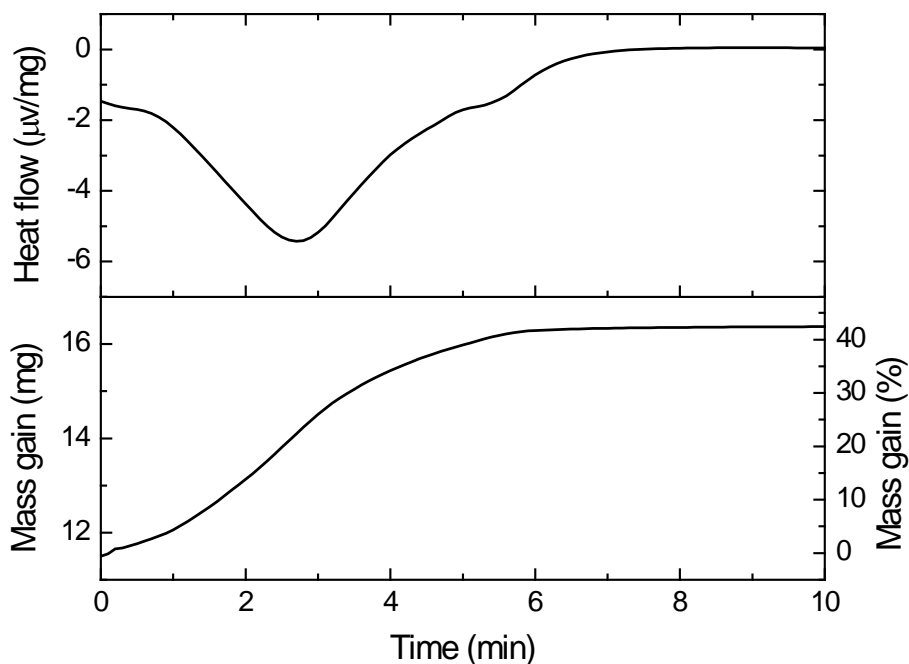
Figure 4.27 – Heat flow and mass change of $CuBr_2$ for sample weight and ammonia gas flow rate of 11.5 mg and 20 ml/min.
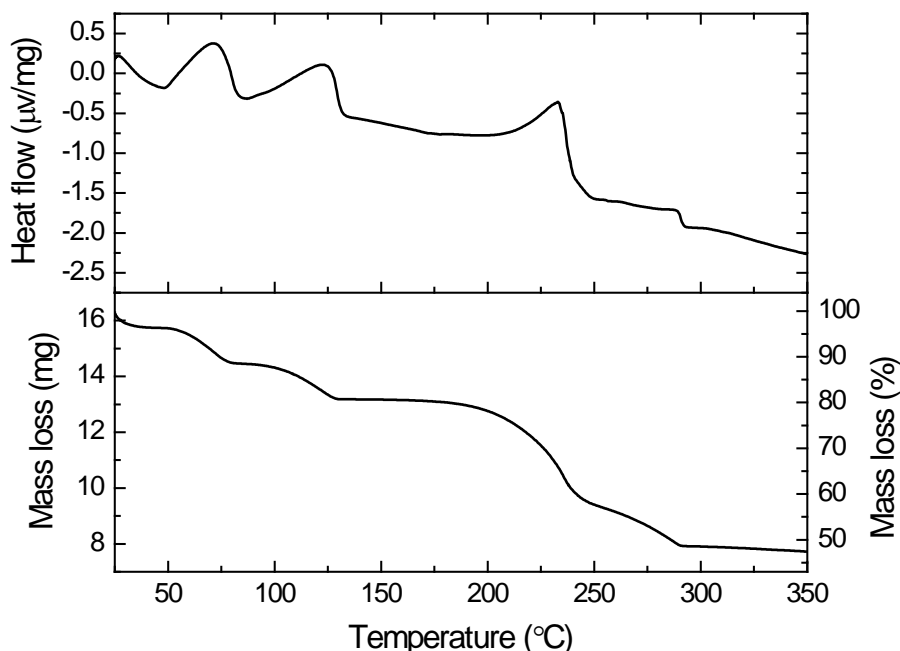
Figure 4.28 – Heat flow and mass change of CuBr$_2$(NH$_3$)$_x$ under a heating profile of 3 k/min.

The mass gain of the material relates to a coordination complex of CuBr$_2$(NH$_3$)$_{5.6}$ and again this probably relates to a coordination of six in the material, as this is a known coordination of CuBr$_2$ in an ammonia atmosphere (Distler & Vaughan, 1967). The same coordination was recorded for MgI$_2$, which gives confidence that the systematic errors in measurement are similar for all of the experiments. With the release of ammonia, shown in Figure 4.28, the CuBr$_2$ experiences a much more varied mass loss profile than that of its alkali earth halide counterparts. From the literature, a possible ammonia desorption process would be from CuBr$_2$(NH$_3$)$_6$ to CuBr$_2$(NH$_3$)$_5$ to CuBr$_2$(NH$_3$)$_2$ to CuBr$_2$(NH$_3$) to CuBr$_2$ (National Research Council, 2003) (Smith & Wendlandt, 1964). This would involve four mass loss stages, consistent with what is observed in Figure 4.28. However the mass loss percentages do not match what would be expected from this particular ammonia release process. CuBr$_2$(NH$_3$)$_6$ is known to be unstable under normal atmosphere, so it is expected that a large proportion of ammonia is released before the heating profile is started. Therefore it is believed that the starting product in Figure 4.28 is CuBr$_2$(NH$_3$)$_2$.
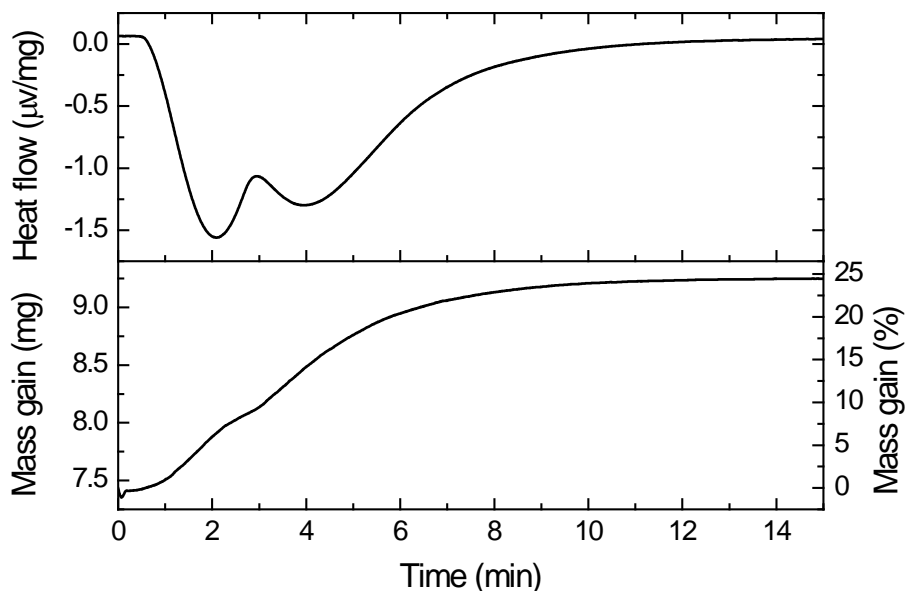
Figure 4.29 – Heat flow and mass change of CuI for sample weight and ammonia gas flow rate of 7.43 mg and 20 ml/min.

The first two mass loss events would then relate to $CuBr_2(NH_3)_2$ to $CuBr_2(NH_3)$ and then $CuBr_2(NH_3)$ to $CuBr_2$. $CuBr_2$ is known to decompose to $CuBr + \frac{1}{2}$ Br_2 at 160°C to 220°C (Nobuyuki & Masahiro, 1970), as seen in this experiment. The final mass loss event occurs after the decomposition of $CuBr_2$ and is most likely from ammoniated CuBr being released. The adsorption of CuI shows the most prominent double exothermic peak, as seen from Figure 4.29. This effect causes a noticeable change in the adsorption rate. The final calculated ammonia content of the adsorbed material is 2.75, i.e. less ammonia adsorbed per unit formula than the other materials tested. However, CuI has previously been reported to have a maximum coordination at STP of three (National Research Council, 2003) (Jolly, 1956). Unlike $CuBr_2$, the ammoniated CuI sample is stable after the ammonia is removed. However, as seen from the desorption profile in Figure 4.30, mass loss occurs marginally above room temperature. There are four mass loss events, as shown from the endothermic peaks in the DSC. The expected mass loss stages would be $CuI(NH_3)_3$ to $CuI(NH_3)_2$ to $CuI(NH_3)_1$ to $CuI(NH_3)_{1/2}$ to CuI, but this does not account for the first mass loss event is approximately a loss of a half rather than a third.
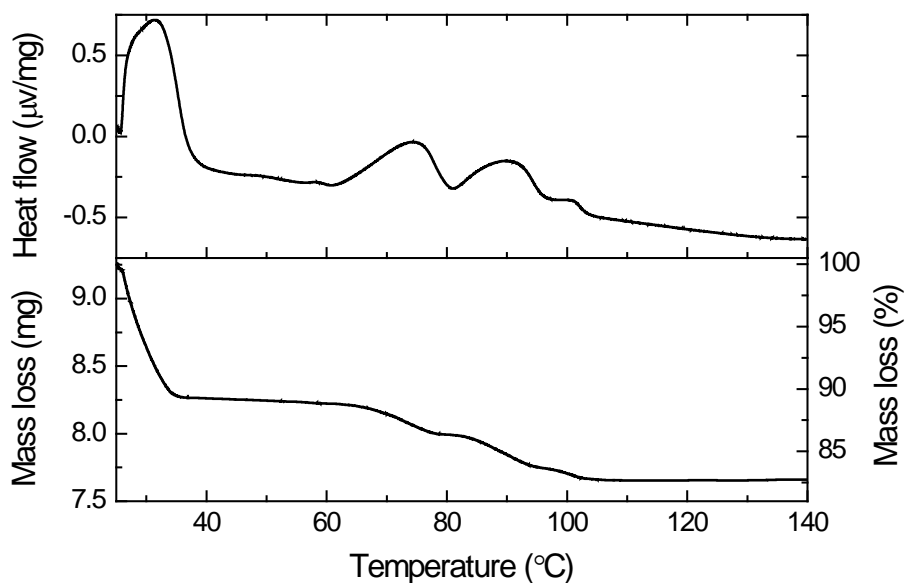
Figure 4.30 – Heat flow and mass change of $CuI(NH_3)_x$ under a heating profile of 3 k/min.

4.4.2 Dielectric results

A sample consisting of 1.5 g of powdered $CuBr_2$ was tested in the experimental setup detailed in section 4.1. The frequency shift in Figure 4.31 shows the same trends as for MgI_2 and $CaBr_2$, with the permittivity increasing as ammonia is adsorbed. The ammonia adsorption into the material saturates at 6.2 hrs.
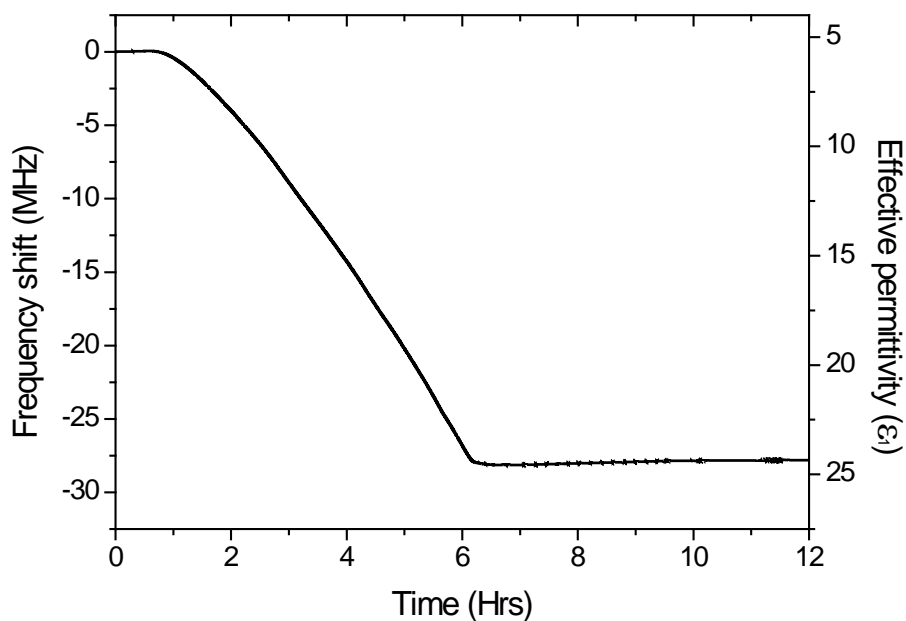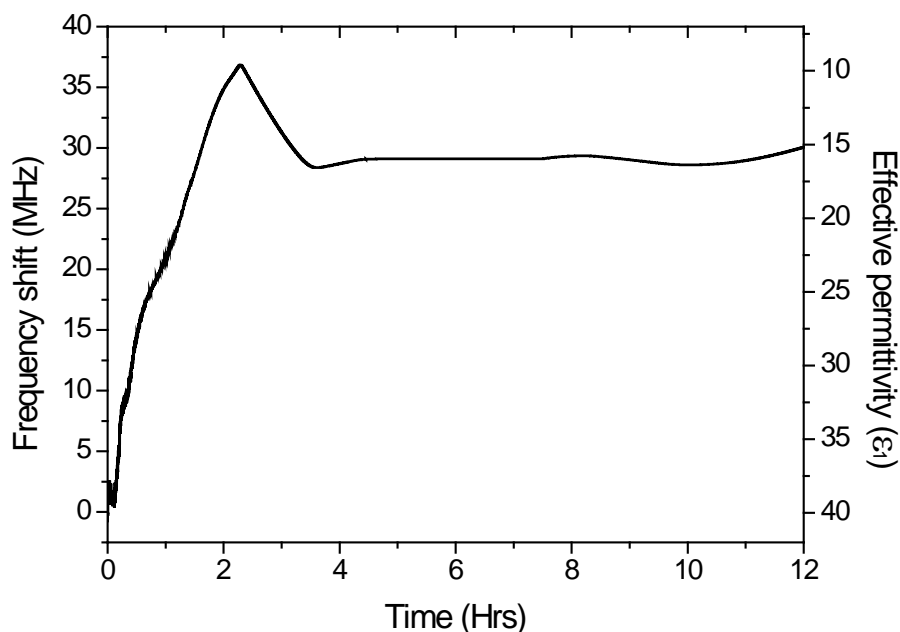

Figure 4.31 – Frequency shift and effective permittivity change of $CuBr_2$ for sample weight and ammonia gas flow rate of 1.5 g and 5 cm³/min.
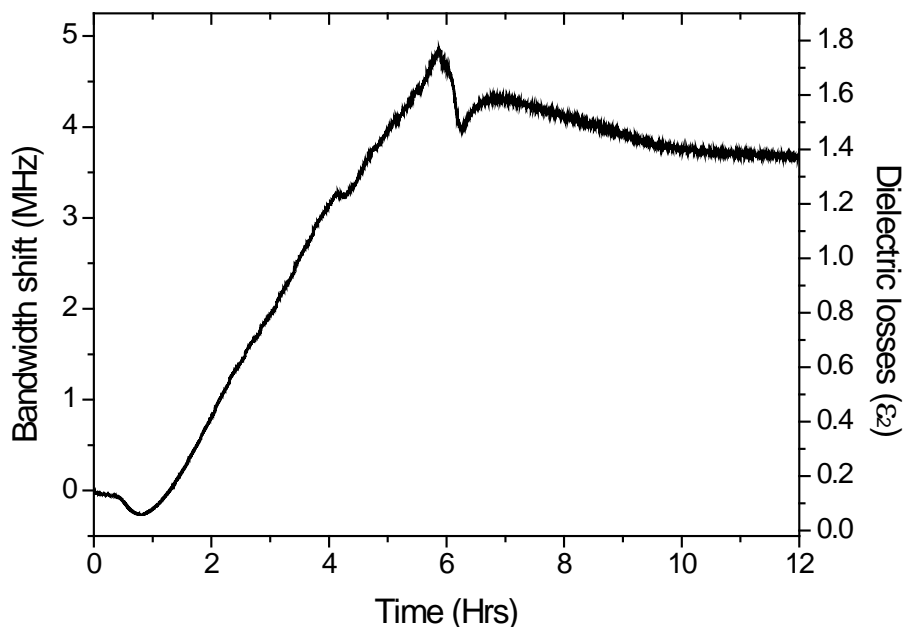
Figure 4.32 – Bandwidth shift and dielectric losses of CuBr$_2$ for sample weight and ammonia gas flow rate of 1.5 g and 5 cm^3/min.

This relates to 5.54 hrs of ammonia being adsorbed at 5 cm^3/min. From Equation 4.1 and Equation 4.2, the number of moles of ammonia adsorbed and ammonia per unit formula for CuBr$_2$ at saturation equate to 0.0477 and 7.07, respectively. At 9.5 hrs the ammonia gas flow was switched off, but argon was not reflowed over the sample. The sample remained in an ammonia atmosphere throughout the whole experiment and so it is not known how much of the ammonia adsorbed is due to physisorption. CuBr$_2$ does not have a known coordination complex of seven, so the most probable reason for this result is a coordination of six combined with some physisorbed ammonia. However, the frequency data by itself is not able to confirm this.

The change in bandwidth for this measurement is shown in Figure 4.32. This shows a general increase similar to the alkali earth halides and electrical resistivity measured in previous studies (Bendahan et al., 2003). The change in bandwidth shows a loss peak similar to the profile seen for CaBr$_2$ in Figure 4.19. This occurs later in the adsorption process, around the saturation in the material, and therefore would relate to changes in higher order complexes.

Figure 4.33 – Frequency shift and effective permittivity change of CuI for sample weight and ammonia gas flow rate of 1.5 g and 5 cm^3/min.

It is possible that this loss peak relates to the same effect of hydrogen bond reforming, which could suggest a phase change from $CuBr_2(NH_3)_5$ to $CuBr_2(NH_3)_6$ (Tomlinson & Hathaway, 1968). Also $CuBr_2(NH_3)_6$ is known to have stable cubic and tetragonal arrangements at room temperature and it is possible that this loss peak could relate a change from one of these structures to the other (Distler & Vaughan, 1967).

The results for CuI are very different to the other halide materials tested. The frequency shift in Figure 4.33 and the bandwidth shift in Figure 4.34 have essentially opposite responses compared with the other halide materials. Because of this the amount of ammonia adsorbed and ammonia per unit formula could not be determined. CuI has been promoted as an effective hole conductor given its band-gap, reported to be as low as 1.1 eV (Amalina & Rusop, 2013) (Grundmann et al., 2013), compared with $CuBr_2$ with a reported band gap of 7 eV and thus lower electrical conductivity (Altarawneh et al., 2015) (Summan, 1999). Permittivities of CuI have been reported as high as 100 (Villain et al., 1995), which accounts for the high starting permittivities and dielectric losses recorded in this experiment, which could be due to high intrinsic carrier densities owing to the low bandgap.
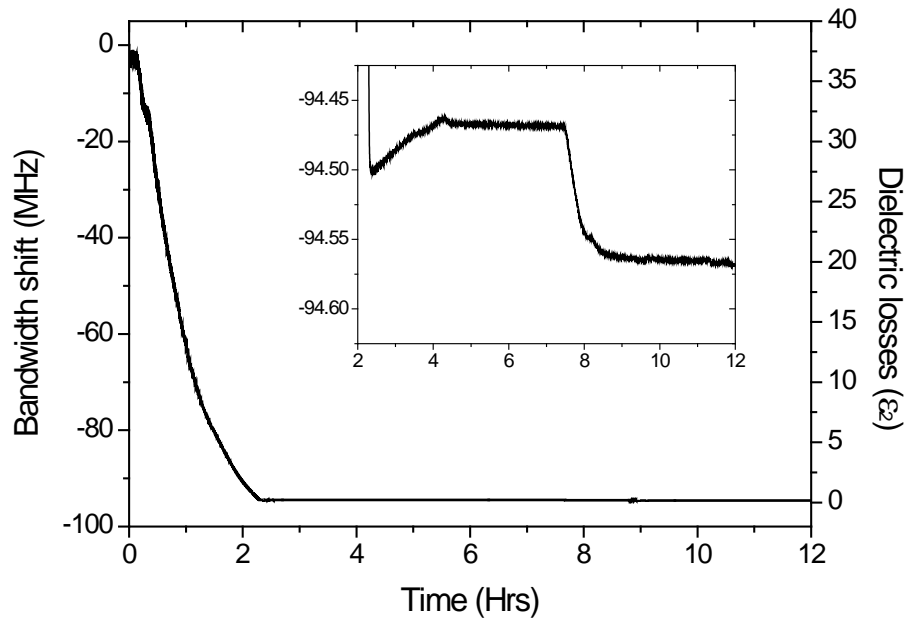
Figure 4.34 – Bandwidth shift and dielectric losses of CuI for sample weight and ammonia gas flow rate of 1.5 g and 5 cm^3/min.

Ammonia adsorption into CuI causes a decrease in the permittivity and dielectric losses. A plausible explanation for this is that the L-type bonding of ammonia donates two electrons, which will suppress the hole density and thus reduce the intrinsic conducting nature of the material. At 2.2 hrs the permittivity increases again. This may not be due to ammonia suppression of the hole density, but rather due to the sensor detecting an increase of ammonia in the measurement space.

The electrical conductance of a material has a high correlation with the bandwidth shifts and any effects after 2.2 hrs no major changes are apparent in the bandwidth data. However taking a closer look at the bandwidth shift after 2 hrs, Figure 4.34 shows a similar response to the MgI$_2$ sample in Figure 4.17, with a possible loss peak at 4.1 hrs. Argon was reflowed over the sample at 7.9 hrs and the bandwidth dropped. This trend is the same for the MgI$_2$ sample, when physisorbed ammonia might be being released from the sample.

4.4.3   Mass spectrometry and mass flow results

The mass spectrometry and mass flow results (shown in appendix 8.5) follow the same trends as the alkali earth halides in section in 4.3.3. Both $CuBr_2$, in Figure 4.35, and CuI in Figure 4.36, show the typical drop in argon content at 40 minutes, as ammonia is introduced into the system. Then nitrogen is observed in the out-gas composition, due to the equipment aspirating air to maintain pressure. At approximately 6.5 hrs for $CuBr_2$ and 4.2 hrs for CuI, ammonia is observed in the out-gas due to the materials saturation with ammonia. These times relate to the saturation times observed in the dielectric results, with an expected delay due to the MS being further down the gas line.
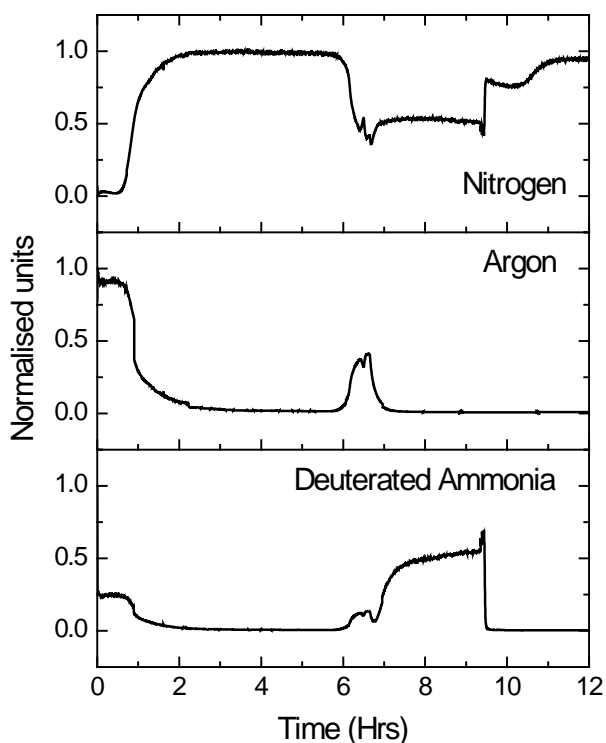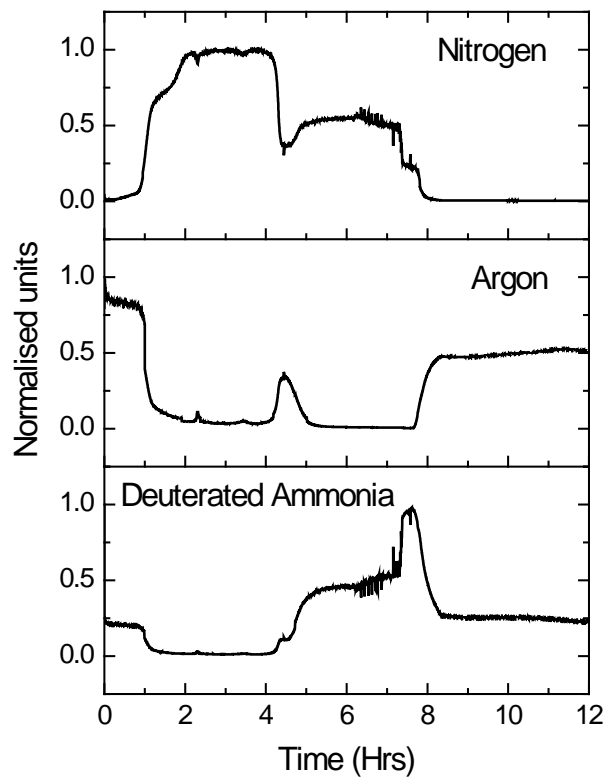

Figure 4.35 - Out-gas compositions of nitrogen, argon and ammonia of CuBr$_2$ for sample weight and ammonia gas flow rate of 1.5 g and 5 cm^3/min.

The plots differ after this, because the gas flow was switched off at 9.5 hrs for $CuBr_2$ and argon was reflowed at 7.9 hrs for CuI. Because of this, $CuBr_2$ returns to aspirating air and nitrogen is recorded in the out-gas, whereas CuI shows an excess of ammonia in the out-gas. This might be due to physisorbed ammonia being released from the sample and coordinated ammonia, as further discussed in sections 4.4.4 and 4.4.5. After this, argon is solely observed in the out-gas.

The calculated number of moles of gas adsorbed and ammonia per unit formula from Equation 4.3 and Equation 4.2 for $CuBr_2$ 0.0529 moles adsorbed and 7.88 moles per unit formula, for CuI 0.031 moles adsorbed and 3.94 moles per unit formula. Factoring in the released ammonia for CuI of 0.0061 moles, the final ammonia per unit formula equals 3.16. These results follow the same trends as seen in the TGA results and for $CuBr_2$ in the dielectric results. The mass flow results for both samples showed a drop in mass flow and pressure when ammonia was being adsorbed. When saturation occurred the mass flow and pressure increased.

Figure 4.36 – Out-gas compositions of nitrogen, argon and ammonia of CuI for sample weight and ammonia gas flow rate of 1.5 g and 5 cm^3/min.

4.4.4   Neutron powder diffraction results

As in section 4.3.4 the clearest results were found in the bank 4 (90°) detectors, with all the time resolved NPD patterns shown in appendix 8.6.2. The NPD profile for the ammoniation of $CuBr_2$ is shown in Figure 4.37. This shows the same constant aluminium peaks throughout the duration of the experiment, with new diffraction peaks evolving during the ammoniation process as seen in other studies of copper halides (Bandosz & Petit, 2009). The results for $CuBr_2$ have very similar responses to that of MgI_2 in Figure 4.23, with just one phase change arising from ammonia being adsorbed into the material. As with MgI_2, this was not expected from the TGA and DSC results in section 4.4.1. The lack of any other phases observed does suggest that the material goes straight to forming its maximum coordination complex and does not form the known possible intermediate phases.
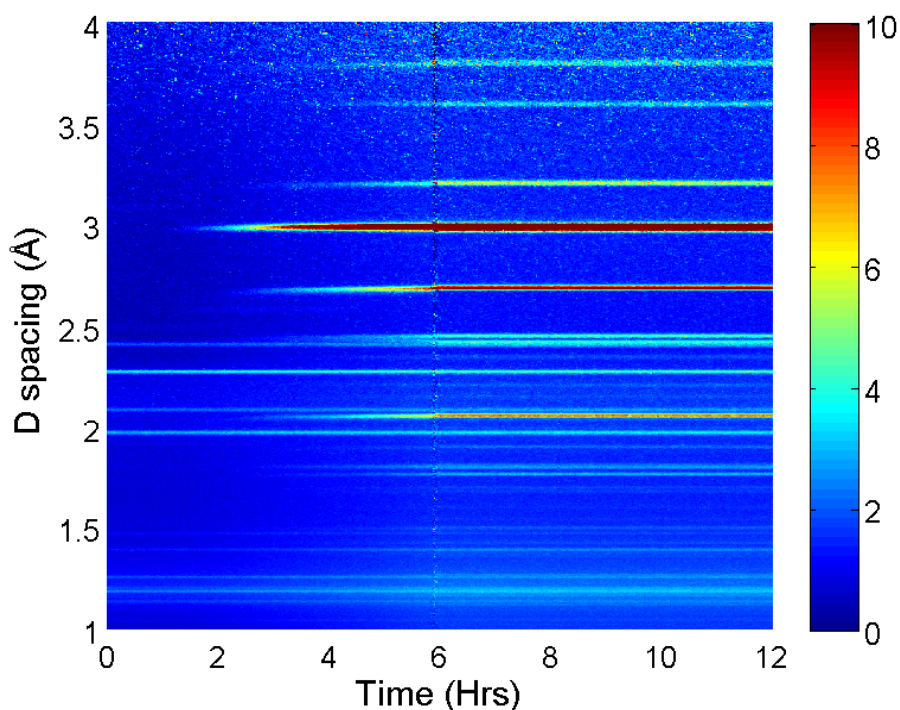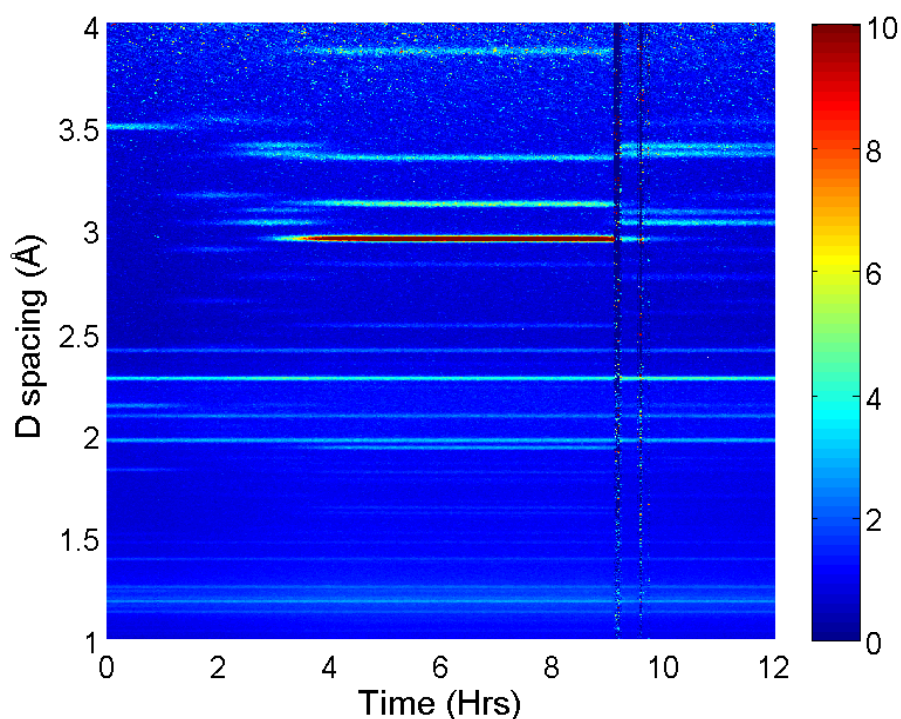

Figure 4.37 – Diffraction peaks from bank 4 (90° detectors), showing neutron count in colour intensity for $CuBr_2$ for sample weight and ammonia gas flow rate of 1.5 g and 5 cm^3/min.

The NPD results for CuI, shown in Figure 4.38, demonstrate a much more varied adsorption process to that of any of the other materials tested. Unlike the other halides tested, the base compound of CuI is visible at the start of the experiment. Therefore, it can be assumed CuI has a relatively high neutron scattering cross section compared to other halide materials. The results show three phase changes during the adsorption process and one phase change when the argon is reflowed over the sample. The diffraction peaks observed from 3-9 hrs period show a phase which is stable in an ammonia atmosphere, but which reverts back to the previous phase when the ammonia is removed. This phase could be $CuI(NH_3)_3$, which from the TGA results in Figure 4.30 is found to be unstable at temperatures just above room temperature. The experiment was conducted in the summer months and with no temperature control in the system it is possible that the ambient temperature was high enough to cause the sample to decompose to a lower coordination complex. The MS information does report a coordination approaching four when this phase is observed. Even though a coordination of four is not known to exist in the literature it is a possibility that $CuI(NH_3)_4$ occurs and then when argon is reflowed the material returns to a coordination of three.

Figure 4.38 – Diffraction peaks from bank 4 (90° detectors), showing neutron count in colour intensity for CuI for sample weight and ammonia gas flow rate of 1.5 g and 5 cm^3/min.

4.4.5 Correlation between MCR and NPD results

Taking the strongest diffraction peak from the NPD data and the frequency shift data from the MCR for $CuBr_2$, a strong correlation can be seen between the two, as shown in Figure 4.39. This correlation is similar to that shown in Figure 4.25 for the MgI_2 sample, where the diffraction intensity and frequency shift both correspond to the quantity of ammonia adsorbed into the material. In the $CuBr_2$ sample the point of saturation is more clearly defined than in the MgI_2 sample. Also the rate of change in the two measurement techniques follows more closely, suggesting a more direct process of the gaseous ammonia settling into a coordinated position than for the MgI_2 sample.

The MCR bandwidth did show a loss peak similar to the loss peak observed by the $CaBr_2$ sample in Figure 4.19. In $CaBr_2$ this loss peak related to structural changes in the material. However, in the $CuBr_2$ sample there was no observed structural change from the NPD data and so this must mean that the loss peak has to be attributed to another phenomenon occurring in the material.
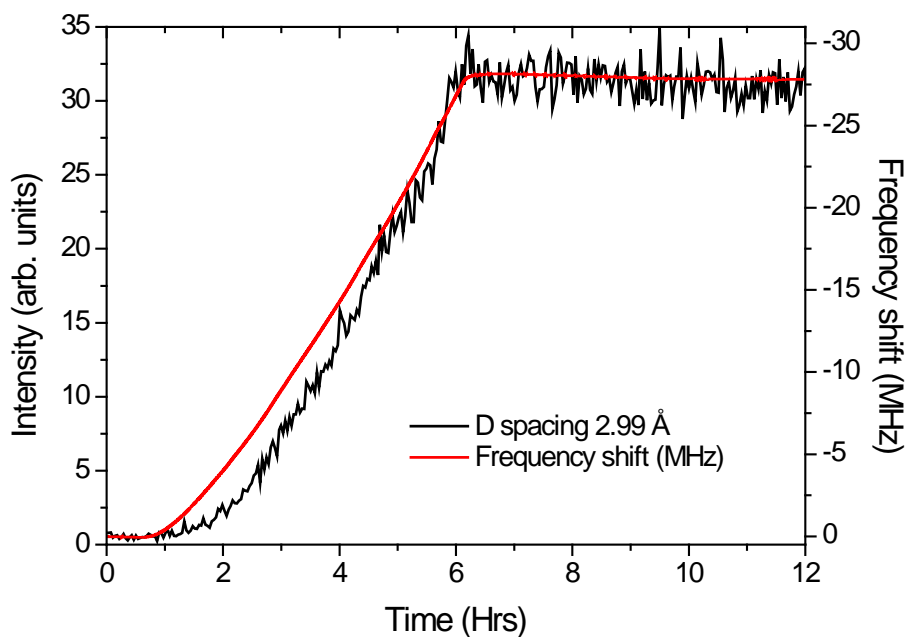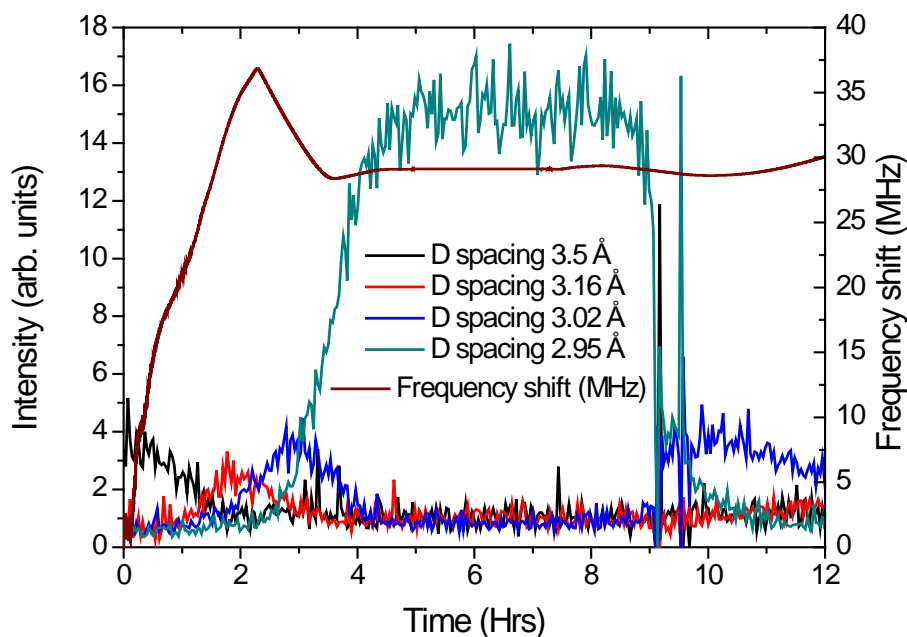

Figure 4.39 – Comparison between frequency shift of MCR and intensity in diffraction peak of PND in $CuBr_2$ for sample weight and ammonia gas flow rate of 1.5 g and 5 cm^3/min.

Dielectric changes in a material that are not related to structural changes, such as relaxation, depolarisation and ionic conduction processes, tend to cause the same changes in real and imaginary permittivity (Ngai et al., 1979). Because there is no change in the frequency data at the same time that the loss peak appears, changes cannot be explained by known dielectric phenomena.

The features in the frequency shift for CuI match up very well with the observed phase changes from the NPD, as shown in Figure 4.40. The initial change in frequency, due to the reduction in hole conduction, is directly correlated with the reduction in intensity of the starting phase CuI, as seen in the d spacing of 3.5 Å. This positive frequency shift ceases when the CuI is completely converted to the material's first ammoniated phase, as seen in the d spacing of 3.16 Å. The material then converts to its next ammoniated phase, with a d spacing of 3.02 Å, with frequency shifts showing the same trends as for the other materials tested. As with the previous phase, when the intensity reaches a maximum, (signifying the bulk material reaching the new ammoniated phase) the frequency stops decreasing.

Figure 4.40 – Comparison between frequency shift of MCR and intensity in diffraction peak of PND in CuI for sample weight and ammonia gas flow rate of 1.5 g and 5 cm^3/min.

The intensity of the final phase, having a d spacing of 2.95 Å, has the largest diffraction intensity, but has a minimal positive frequency shift. From the MS data, ammonia is still being adsorbed at this time so it would be expected that there would be a negative frequency shift. The reason for this positive shift might have something to do with the final phase not being as stable as the other phases, as seen when argon is reflowed. The frequency shift does return to its value at 3.2 hrs, when argon is reflowed and the material returns to its previous phase. However the bandwidth shift shows a greater reduction, which suggests ammonia is being released from the coordinated material and from physisorbed ammonia.

5 Simultaneous X–Ray diffraction and microwave measurement

The measurement of dielectric and XRD information has been shown to complement each other well in a host of experiments (Cuenca et al., 2015) (Naohiko et al., 1996). In this chapter we combine XRD and MCR measurements on alkali earth halides, as ammonia gas is introduced to the material, in the hope that simultaneous measurement can give a more detailed understanding of the processes involved. The MCR used in these experiments was a hairpin resonator. The design and measurement capabilities are detailed in section 3.2.

5.1 Integrated measurement system

Experiments were performed on the I11 beamline at the diamond light source (Thompson et al., 2009). The measurement system is designed to simultaneously measure time resolved structural information (from XRD), dielectric information (from MCR) and system pressure (from pressure sensor) of the ammonia adsorption processes. In the case of these experiments, all measurement artefacts and uncertainties were determined in post analysis rather than performing calibration measurements, as in section 4.1.3.

5.1.1 Experimental setup and procedure

Rather than using a continuous gas flow of ammonia, since there is no out-gas from the quartz sample capillary, a backpressure of ammonia was applied and then introduced to the sample. A diagram of the gas line and measurement equipment setup is shown in Figure 5.1. The vacuum pump is used to apply a vacuum to the gas lines prior to an experiment, to prevent the sample being exposed to air.

The samples tested were powders of $MgCl_2$ (98.9% purity, Sigma-Aldrich) and $CaCl_2$ (97% purity, Sigma-Aldrich), which were ground down in an inert environment to an intended grain size of less than 1 micron. These were placed into a quartz tube to a depth of about 2 cm, to ensure that the section between the hairpin plates was totally filled. The amount of sample material varied from experiment to experiment but in all cases occupied at least the volume within the hairpin, so that it was exposed to the incident X-ray beam. Quartz wool plugs were used to prevent the powder escaping when a vacuum was applied and the tube was glued to the low pressure gas cell. The cell was then connected to the goniometer for accurate positioning of the quartz capillary in the resonator (and hence X-ray beam). The hairpin resonator was connected by RF cables (not shown) to a microwave network analyser (Agilent Fieldfox N9912A) under computer control (National Instruments LabVIEW), which measures the transmitted microwave power as a function of frequency. The measurement setup has been discussed in more detail in section 3.3. The XRD beam was directed perpendicular to the quartz tube and between the hairpin's plates. The wavelength of the X-ray signal was set to 0.082577 nm and the time taken to complete a full XRD scan was approximately 3 minutes.
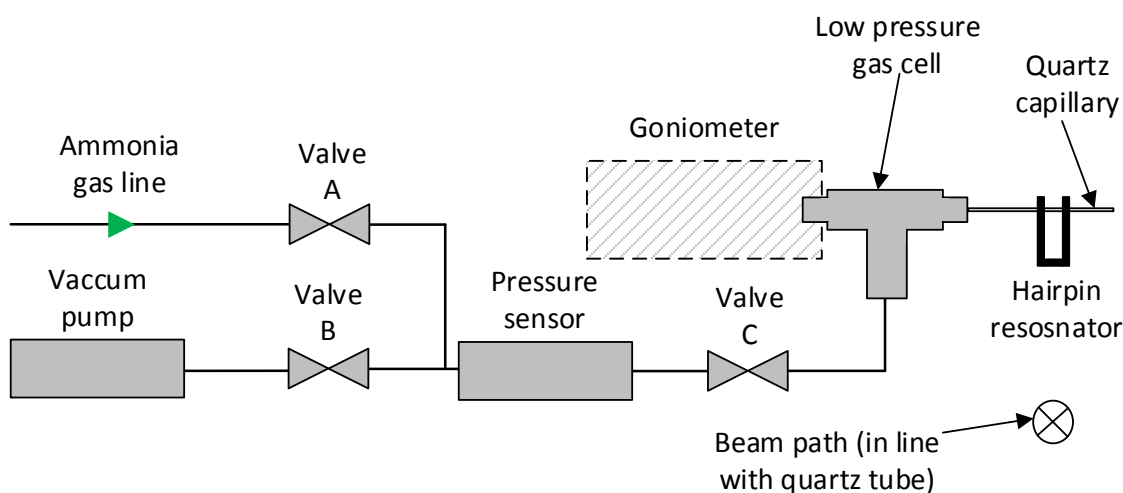
Figure 5.1 – System diagram of simultaneous X-ray diffraction and microwave measurement setup showing gas lines and measurement equipment.

A backpressure of approximately 1.5-2.0 bar was applied between the ammonia gas line and the valve C, where pressure of the system was periodically checked and recorded through the pressure sensor. The gas line was connected to a low pressure gas cell which itself connects to the quartz capillary within the hairpin resonator, as shown in Figure 5.2. A background measurement was first taken of the sample under vacuum by opening valves B and C to remove any argon (or air) from the gas cell. The two valves were then closed and valve A opened and a backpressure of approximately 1.5 bar was set up in the gas line, after which valve A was closed. Valve C was then opened again and ammonia was introduced to the sample. This is the zero point shown in the following results. When the pressure dropped to below 1 bar, the same procedure was repeated to top up the system pressure.
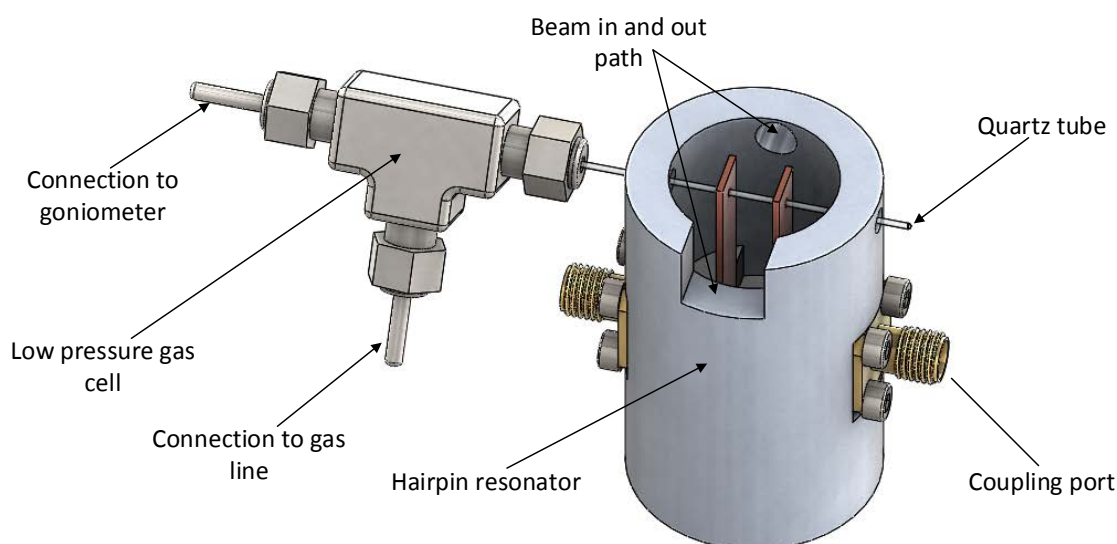
Figure 5.2 – Model of gas cell and hairpin resonator showing position of quartz tube relative to XRD and MCR measurement equipment.

5.1.2   Artificial features and measurement uncertainties

It was endeavoured to keep the sample materials in an inert environment during the preparation stage of the experiment. However, the gluing stage of the preparation had to be conducted in an air environment during which it could have been possible for air to reach the sample and in that time to have partially hydrated some of the material.

By reducing the amount of aluminium in the X-ray beam, the resulting pattern from the diffracted beam will have few features associated with aluminium. However, in the preparation the crystallite size of the powder samples was reduced to as small as possible to ensure that the resulting Deybe-Scherrer rings, discussed in section 2.3.2 are unaffected by large crystallites, which can otherwise give rise to errors in the intensities from diffraction patterns (He et al., 2003). Because of the unknown particle size distribution of the powdered samples after grinding, such errors in XRD intensities are unknown but are assumed to have been minimised.
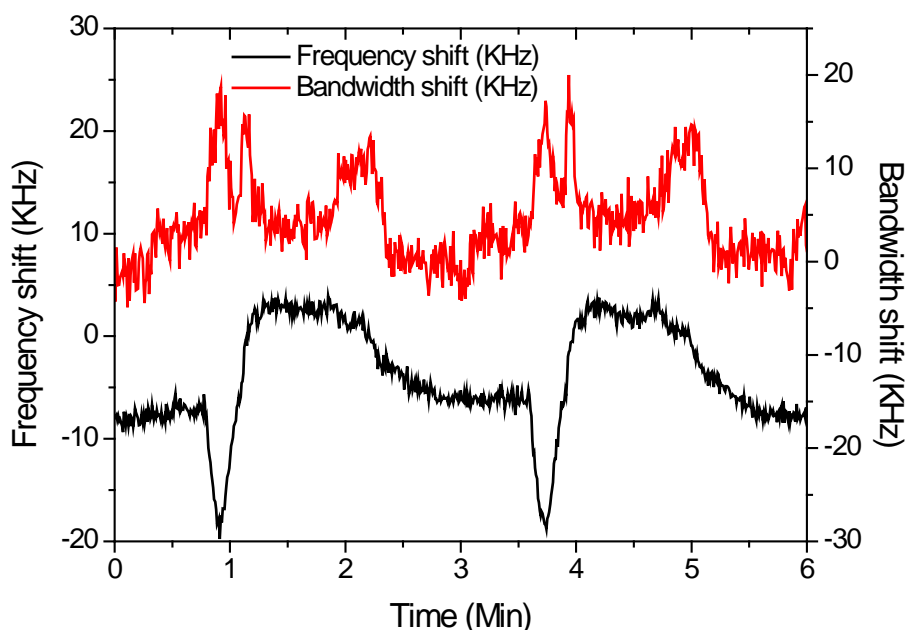
Figure 5.3 – Frequency shift and bandwidth shift of measurement due to rotation of XRD detectors showing periodic response.

There is a clear periodic artefact in both sets of dielectric property data which is associated with the diffractometer rotation, as shown in Figure 5.3. By necessity for the X-ray measurements, the ends of the hairpin are free of metal and this allows the microwave electric field to spill out and occupy a large volume outside the hairpin (i.e. it is not effectively screened by the aluminium shield). The artefacts in the data are due to the interaction of the hairpin's external electric field with the moving parts on the diffractometer. Aside from these artefacts, the only noticeable change in the dielectric data occurred at 1.52 hrs, after which there is a slow increase in frequency and a reduction in bandwidth. At this, and subsequent, time the system pressure was more frequently topped up. However, we have previously shown that ammonia adsorption into halide materials results in a decrease of resonant frequency and increase of bandwidth, so we do not believe that the measured changes are directly related to ammonia adsorption.

5.2 Results

Because of the smaller sample quantities in these measurements compared to previous experiments, there was reduced chance of the material breaking the quartz tube. For this reason $MgCl_2$ (98.9% purity from Sigma-Aldrich) and $CaCl_2$ (97% purity Sigma-Aldrich) were tested in the XRD. The area of sample space the hairpin measured 4.526 mm^3. However because the quartz capillary was orientated sideways the powder may not occupy the whole volume of the capillary. For this reason and the other large uncertainties in dielectric measurements, effective permittivities are not shown in this section.

5.2.1 System pressure results

The pressure of the system was measured at discrete points during the experiment. When the pressure drops to around 1 bar the pressure of the system is increased. This is shown in Figure 5.4 for $CaCl_2$ and Figure 5.5 for $MgCl_2$, where the bold solid line indicates the point at which the system pressure was increased.
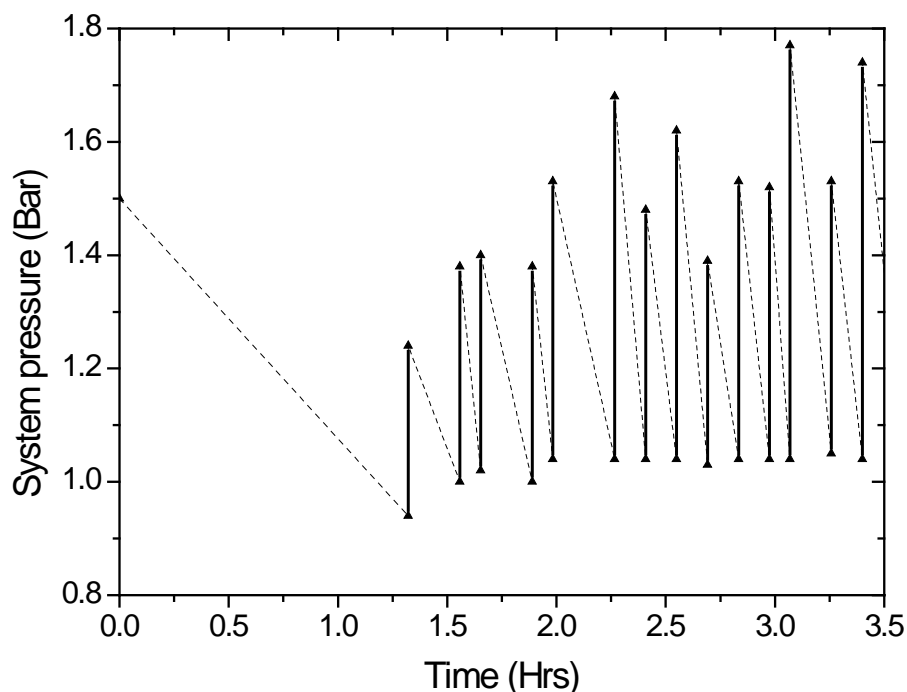
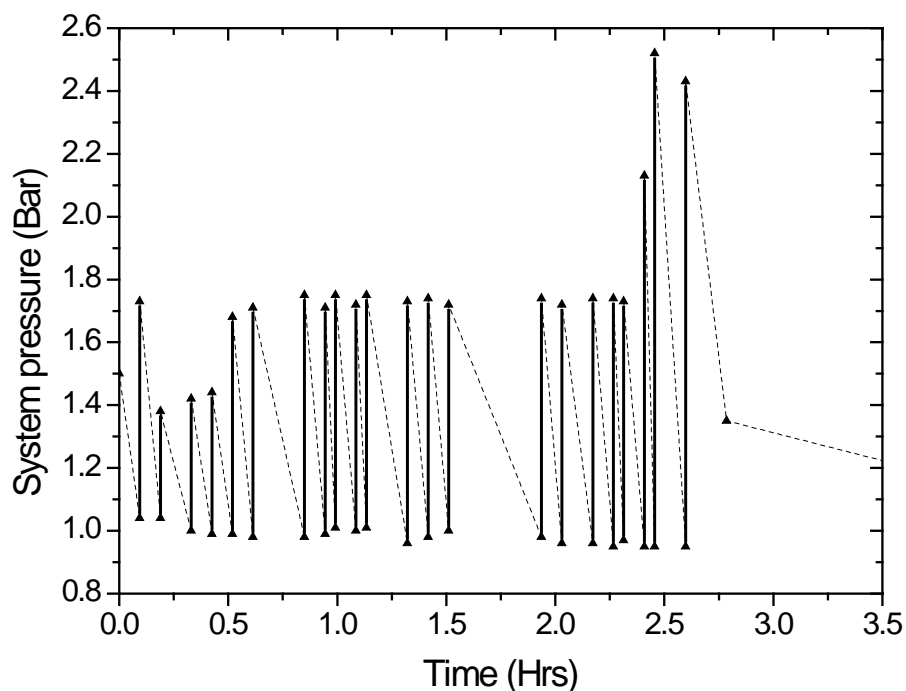**Figure 5.4 – System pressure of CaCl₂ under periodic exposure to ammonia gas, highlighting points at which ammonia was added to system.**

The dashed lines in the figures indicate the change between one pressure reading and the next. However, due to the material's propensity to adsorb ammonia rapidly, the change in pressure is expected to follow an exponential decay from larger pressure to smaller pressure.

For the $CaCl_2$ sample, it was observed that system pressure dropped back to 1 bar for the entire duration of the experiment. It can then be assumed that the bulk material did not saturate and reach its full coordination complex. In Figure 5.5 the $MgCl_2$ sample appears to adsorb all the ammonia exposed to it until 2.75 hrs when the recorded system pressure was above 1 bar. After this point the system pressure tends to drop at a reduced rate compared to the previous pressure differences. The pressure does drop back to 1 bar at approximately 4.5 hrs into the experiment and the pressure is increased back up to 1.5 bar, where the pressure continues to drop at the reduced rate. It can then be assumed that the kinetics of ammonia adsorption in the material changes at 2.75 hrs and the reasons for this are detailed in sections 5.2.2 and 5.2.3.

Figure 5.5 – System pressure of $MgCl_2$ under periodic exposure to ammonia gas, highlighting points at which ammonia was added to system.

5.2.2   Dielectric results

The resonant frequency results for the first resonant mode of the hairpin cavity are shown in this section. The results for $CaCl_2$ under ammonia exposure are shown in Figure 5.6. Apart from the periodic signal from the diffractometer rotation there is little change in resonance. The only noticeable change is at 1.52 hrs where the frequency slowly increases and the bandwidth decreases. The time of this event links with when the system pressure is more frequently topped up, as seen in Figure 5.4. However, ammonia adsorption into halide materials has shown that the resonant frequency decreases, not increases. Therefore we believe these changes are not directly related to ammonia adsorbed in the material. The hairpin measures 6 mm of the material in the quartz capillary and the capillary has been filled to a height of greater than 6 mm. Therefore, some (if not all) of the ammonia adsorption process goes unobserved by the hairpin resonator. We assume from the system pressure results that ammonia is being adsorbed and that ammonia adsorption in $CaCl_2$ is an exothermic process (Kubota et al., 2014). Therefore we could attribute the increase in frequency from the hairpin to heating from the exothermic reaction of ammonia adsorption in the quartz capillary, due to the increased rate of ammonia exposed to the sample from topping up the system pressure (Luiten et al., 1999) (Krupka et al., 1998). However we do not measure temperatures in this experiment and the changes in frequency could be from ambient temperature increases as shown in appendix 8.3.2.
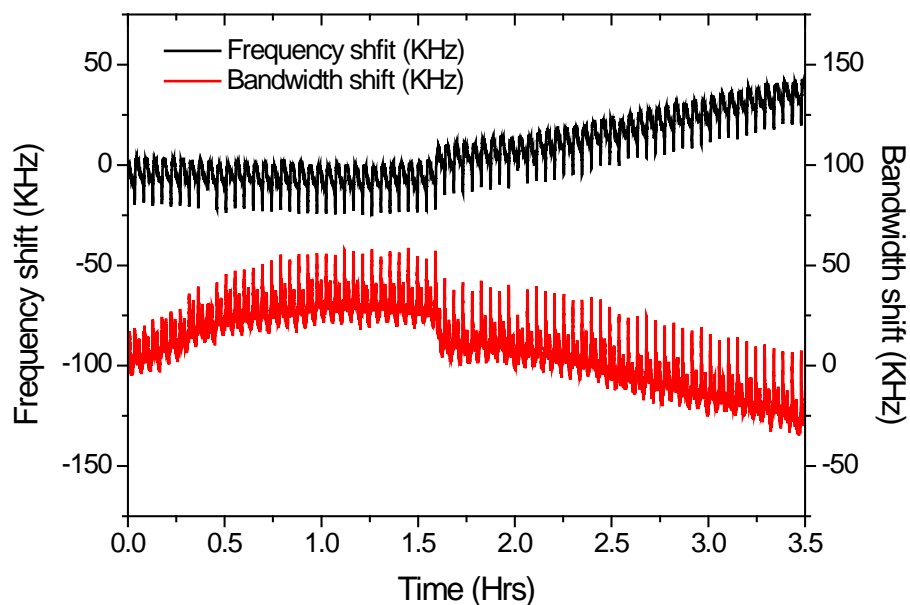
Figure 5.6 – Frequency and bandwidth shift of CaCl$_2$ under periodic exposure to ammonia gas.

To prevent the same mistake occurring as with the CaCl$_2$ sample having excess material before reaching the measurement space, the quartz capillary containing the MgCl$_2$ sample was positioned so that the material initially exposed would be very close to the beginning of the hairpin pins. The frequency and bandwidth for the MgCl$_2$ shows more features than those for the CaCl$_2$ sample, as seen in Figure 5.7. There is an initial change of 100 kHz in the frequency and 150 kHz bandwidth when ammonia is introduced to the sample. This change is believed to be from either temperature increases from the sample or the sudden change in pressure, thus redistributing the powder slightly within the measurement space. It can be seen from 0.2 to 0.7 hrs that there are spikes in the frequency shift. These spikes link up with the times when the pressure is increased from Figure 5.5. These features may correlate with ammonia being adsorbed into the material. However, it is unusual that these shifts are transient features and that later pressure increases do not invoke further spikes in the frequency shift.
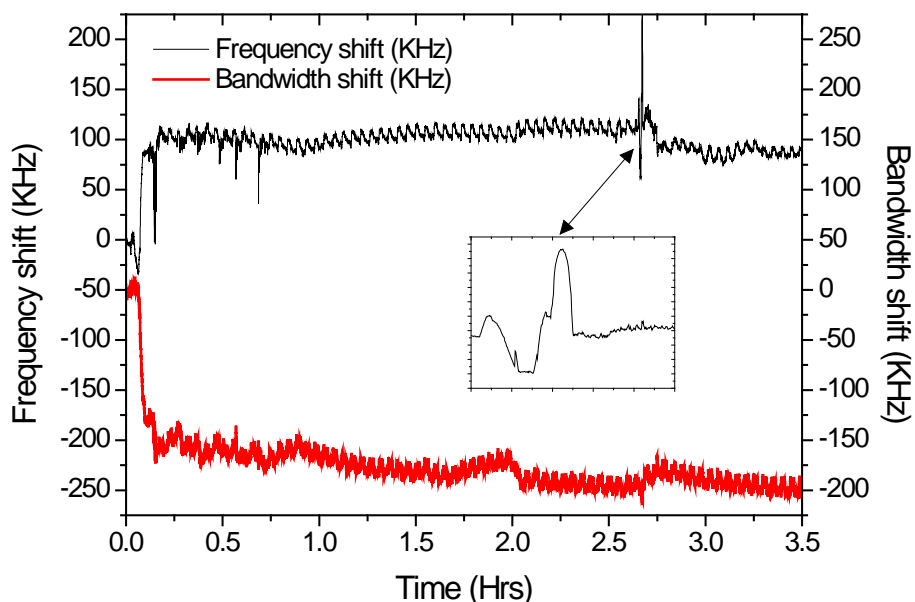
Figure 5.7 - Frequency and bandwidth shift of MgCl$_2$ under periodic exposure to ammonia gas.

The most notable feature from the dielectric results comes at 2.65 to 2.7 hrs and is highlighted in Figure 5.7. This feature occurs at the same time as the saturation of the material from the system pressure data. Therefore, this spike in the frequency shift relates to changes occurring at saturation. Dielectric changes at saturation have been previously observed in the measurements in chapter 4. However, these dielectric changes have been most prominent in the bandwidth information and in Figure 5.7 the bandwidth shift is minimal compared to the frequency shift. Sudden dielectric changes like those seen in Figure 5.7 have been observed in the literature (Jakubas et al., 1985) (Shportko & Venger, 2015). However, these changes are attributed to amorphous to crystalline, phase transitions or vice versa, whereas in these experiments crystalline to crystalline phase transitions are more likely.

5.2.3 X-ray powder diffraction results

In-situ XRD studies of uptake and release of hydrogen and ammonia from various materials have been studied with similar results to those shown in chapter 4, where diffraction peaks appear as ammonia is adsorbed (Nakagawa et al., 2007) (Meisner et al., 2006). Evolution of diffraction peaks was expected in the studies performed in these experiments. However very different responses occurred compared to the results in chapter 4.

The results from ammonia adsorption into $CaCl_2$ are shown in Figure 5.8 and it can be seen there is no appreciable change in the diffraction pattern during the experiment. This fits with the dielectric results in Figure 5.6 which also show no appreciable change. The reason for this, as with the dielectric results, is that the ammonia adsorption process is occurring outside the measured region of the sample.

For the $MgCl_2$ sample, shown in Figure 5.9, the results show a diffraction pattern for $MgCl_2$ at the start of the experiment. The diffraction pattern is relatively constant until 2.7 hours with the possibility of a new peak arising at a d spacing of 3.38 Å. At 2.7 hrs the signal dramatically changes. The time of this change occurs at the same time as pressure is retained in Figure 5.5 and the frequency spike observed in Figure 5.7. This change happened rapidly, as shown in Figure 5.7. Therefore the 3 minute scan time of the XRD was not fast enough to detect the transition process and any intermediate phases that may have occurred in that time. The new diffraction pattern from the change has diffraction peaks at much lower intensities compared with that of the original diffraction peak, around an order of magnitude less.
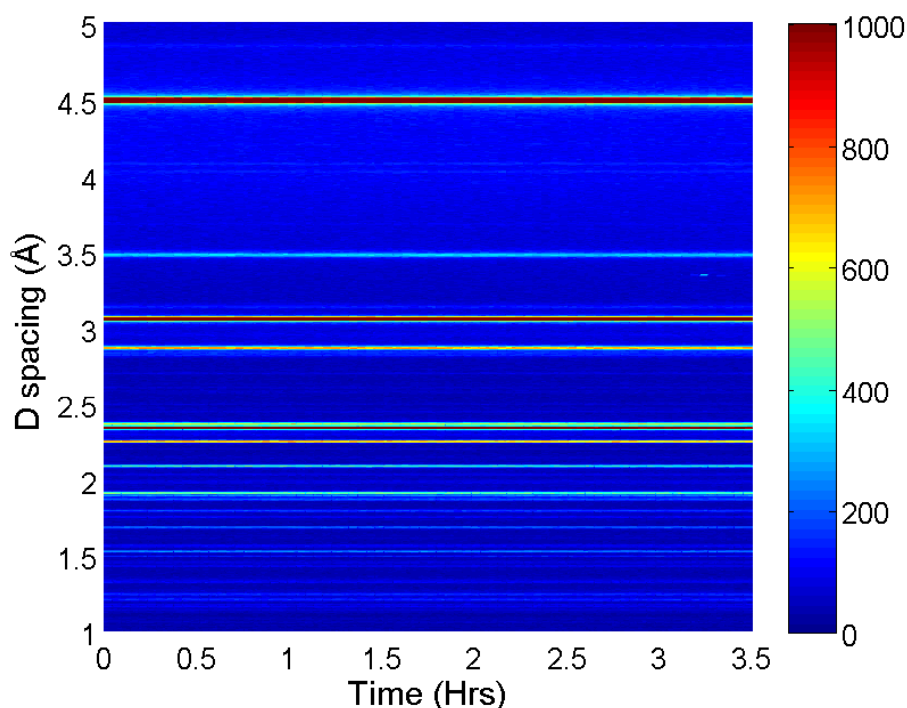
Figure 5.8 – X-ray diffraction peaks in colour intensity for $CaCl_2$ under periodic exposure to ammonia gas.
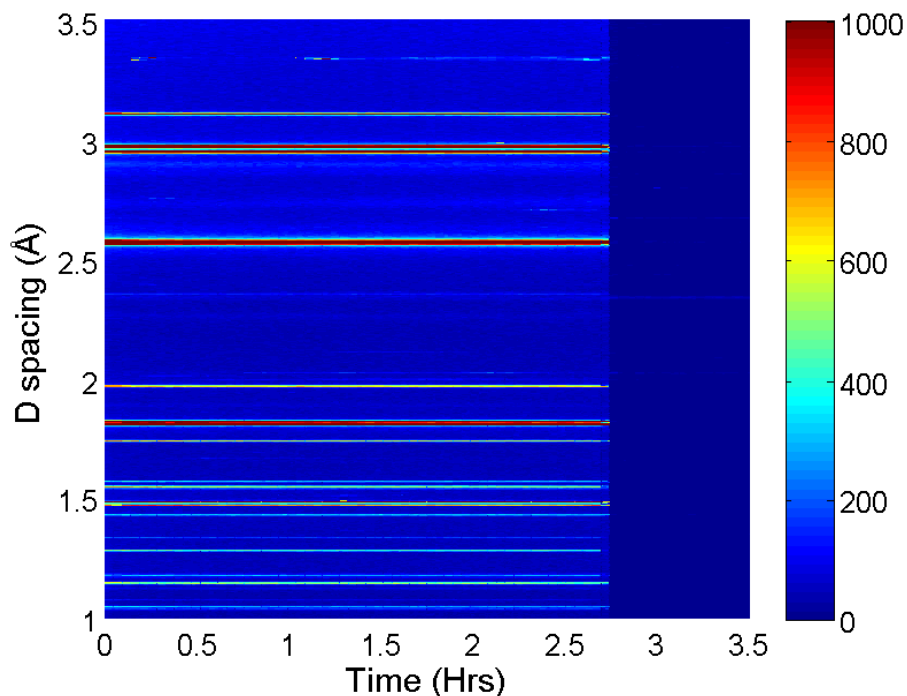
Figure 5.9 – X-ray diffraction peaks in colour intensity for MgCl₂ under periodic exposure to ammonia gas.

This effect of lowering intensity peaks have been observed in gas hydrogenation processes in other studies (Richardson et al., 2003). The diffraction peaks before and after these transitions are shown in Figure 5.10. The diffraction patterns between the two are clearly different, indicating a phase change in the material.
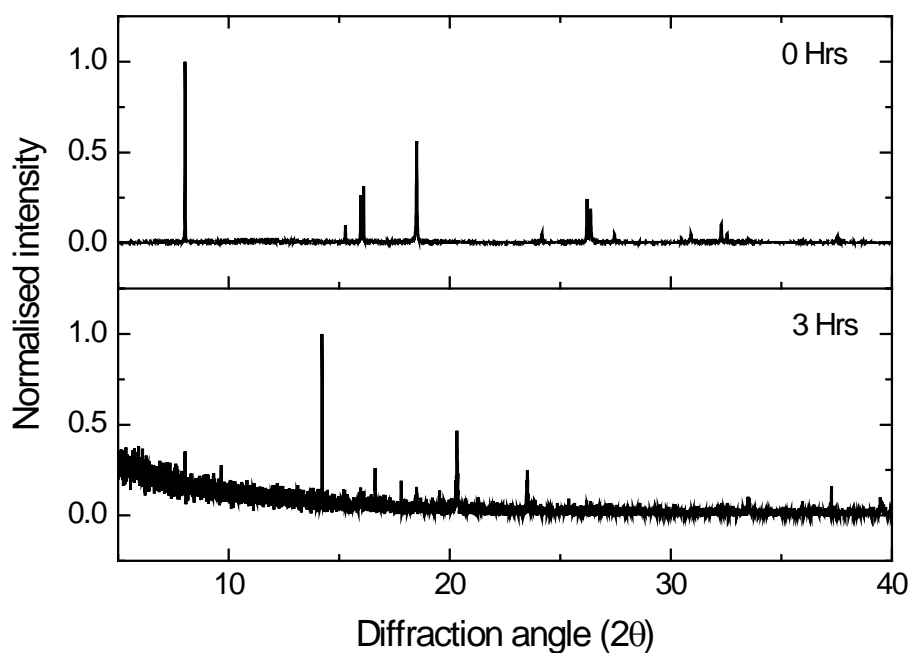

Figure 5.10 – Diffraction pattern for MgCl₂ under periodic exposure to ammonia gas showing before and after transition.

6 Conclusions and future work

6.1 Conclusions on simultaneous neutron diffraction and microwave measurement

The experimental setup used to measure dielectric and structural changes in ammonia adsorption simultaneously has proved to be able to measure a range of physical phenomena occurring in the material. With this information, the amount of ammonia adsorbed by the material can be obtained. If the material undergoes any phase changes during adsorption and if the ammoniated material is stable when ammonia atmosphere is removed, the percentage of chemisorbed to physisorbed ammonia can be inferred, and also changes in electrical properties can be observed with ammonia adsorption.

In the four halides tested, general repeatable trends are seen in the measured MCR data, such as a decrease in frequency and increase in bandwidth with ammonia adsorption. The NPD data show the appearance of new diffraction peaks due to diffracted deuterium from coordinated ammonia. Nitrogen content in the MS was used to infer adsorption in the material. Sections 4.3.5 and 4.4.5 have shown that features in the different measurement techniques can be related to each other and with the combined information from these multiple measurement techniques, features can be linked with physical phenomena. Some features do not show the same repeatable correlation between the dielectric and structural information, most notably the appearance of the dielectric loss peaks. In the $CaBr_2$ sample the loss peak relates very well to the diffraction data. In the CuI sample, where there are many phase changes, the bandwidth data does show changes which may indicate loss peaks, but these features are much smaller and it would be ambiguous to relate them to the diffraction data. On the other hand, the $CuBr_2$ shows an obvious loss peak in the dielectric data, but no structural changes were observed.

In conclusion the combined MCR and NPD techniques provide a wealth of information on the ammonia adsorption process in halide materials, but some features observed by these measurement techniques are still not fully understood and can lead to ambiguous analysis of the data.

6.1.1   Improvements and future work

On the system side, improvements to the MCR would include improving the SNR which would allow for larger and more varied samples to be tested. Methods have been implemented to improve this and are detailed in section 6.3. The other major improvement to the current system would be to run experiments at lower flow rates than 5 cm^3/min, but the current mass flow controller is unable to do this. A lower flow rate would give more capture time for the NPD to measure the intermediate phases and features that occur. To prevent the sample blocking the quartz tube a secondary material could be included that acts as a spacer into the measurement space. However, this material would have to be relatively insensitive to neutrons, microwaves and be unreactive with the sample material. Using quartz beads is one of the only possible solutions to this.

To improve the analysis of ammonia adsorption measurements, structural refinement analysis can be performed on the materials. This can give information on the ammonia coordination of the phases observed and the resulting crystal structures. Other ex-situ measurement techniques can be used like TGA to give added information on ammonia adsorption, most notably, techniques that can give insight into the freedom and bonding mechanisms of the hydrogen atoms within the coordinated material. To achieve this, the use of Raman spectroscopy or infrared adsorption studies can be performed to observe the intermolecular and intramolecular hydrogen bonding in ammoniated halide materials (Triggs & Valentini, 1992) (Bertin et al., 1957).

6.2   Conclusions   on   simultaneous   X-ray   diffraction   and   microwave measurement

The results presented in chapter 5 are of lower quality and accuracy compared to those of NPD (Chapter 4), mainly due to the measurement problems explained in section 4.1.3. The results did, however, show clear dielectric and structural changes for $MgCl_2$. It would be unproductive to attempt to make comparisons between the XRD and NPD results owing to the very different experimental configuration, notably the gas delivery systems that give very different dynamics of ammonia adsorption. It is believed by this author that, even with the improvements mentioned in the next section, XRD will always be inferior to NPD in its ability to study the dynamics of ammonia adsorption.

6.2.1   Improvements and future work

The experiment was able to measure simultaneous dielectric and structural changes on ammonia adsorption, but only for the $MgCl_2$ sample. No changes were measured for the $CaCl_2$ sample, which is most likely due to the ammonia adsorption region being outside the active region for both the dielectric and XRD characterisation. Periodic artefacts were observed in the dielectric measurement data due to the movement of the diffractometer. Hence, the data presented here should be treated as preliminary and improvements to the system are necessary before further XRD experiments are attempted. In summary, these are to:

(i)   Reduce the interference between the resonator and the diffractometer by using a microwave resonator with a less exposed structure.

(ii)   Adopt a microwave resonator with a higher quality (Q) factor and lower mode volume, thus increasing the resolution for dielectric property measurement (i.e. greater cavity perturbation in terms of resonant frequency and bandwidth for a fixed, small sample volume). This is inherently linked to (i) above, so we propose a split cavity resonator (Krupka et al., 1996) (Janezic & Baker-Jarvis, 1999) that will also allow entry of the incident X-ray beam, and exit of the diffracted beams, both without obstruction.

(iii)   Develop a gas flow system for greater control of the material phase changes so that they occur more gradually, allowing them to be tracked by the XRD system.

(iv)   Build in the capability of rocking the sample to reduce effects of large grain size, mosaic spread and inhomogeneity on the XRD measurements.

6.3   Future work on integrating heating capabilities to measurement setup

The criteria that determines a commercially viable hydrogen fuel source shown in section 2.1 notes two measures which have not yet been addressed in this thesis. These are a recoverable amount of hydrogen: 90% and cycle life: 500 times (requirements for the physical properties of storage material) (Ross, 2006). To assess these material parameters, the ammonia storage material must be measured under ammoniation and unammoniation processes. The method to release ammonia from materials such as halides and MOF's is to heat them up, as with the TGA experiments conducted in this project (Miki et al., 1995). In this chapter a system is devised to perform ammonia uptake and release while measuring the dielectric and structural properties. In doing so the cyclic properties of the material can be assessed (Ikeda et al., 2008).

6.4   Experimental design

The design of this experimental setup builds on the current experimental setup in sections 3.1 and 4.1.1. However, the application of heating the sample adds new design considerations that are tackled in this section. The first question that determines the subsequent design decisions is the type of heating applied. Microwave heating would be very easy to implement, due to the cavity structure already being integrated into the system. Microwave heating would also be a more efficient heating method than conventional heating and would alleviate problems with heating the cavity structure (Bykov et al., 2000). However, the dielectric properties of the material are expected to change significantly during heating, as implied from the experiments conducted in this thesis. This will give highly nonlinear heating rates and this non-linearity will vary from material to material. Therefore control of the sample's temperature is expected to be very different to manage from sample to sample during experiments. For this reason alone it was concluded to use conventional heating methods should be used to heat the samples.

6.4.1 Mechanical construction

As in section 3.1.1, the aim is to have Q factor of the resulting cavity as high as possible and the neutron scattering cross section as low as possible. The solution to the neutron scattering cross section is the same as before where a 2 cm band section of thinned aluminium is machined into the cavity walls to reduce interference.

The solution to retaining high Q factor becomes more difficult, because heating of the cavity walls will cause surface resistance to increase and thus the Q factor will reduce. Aluminium also has a melting point of 660 °C and will deform at lower temperatures. For these reasons general heating of the entire structure is not desired. Any heating element cannot be placed within the cavity structure because it will disrupt the resonant fields within the cavity. So a solution to apply heater tapes above and below the cavity structure to the quartz tube would need to be used. This is shown in Figure 6.1 and to reduce heating of the cavity further, a thermal insulator will be placed between the cavity and heater tape. This will be made out of Macor, due to its good thermal insulating properties and easy machinability, and this is detailed further in section 6.4.4. Copper tape will be placed between the heater tape and the quartz tube to increase the thermal connection between the two materials.

An improvement on the previous MCR design is to have the cavity made out of two pieces rather than three. This will improve the Q factor of the cavity by minimising the current flow across a mechanical join between metal surfaces. The bolts used in the cavity are helicoil bolts so as not to impede the neutron beam. The cavity design is shown in Figure 6.1 and appendix 8.2.4, this will fit into an experimental rig almost identically as the one shown in Figure 4.2 (left), with only the changes in dimensions to the rig and quartz tube being proportional to the change in cavity dimensions.
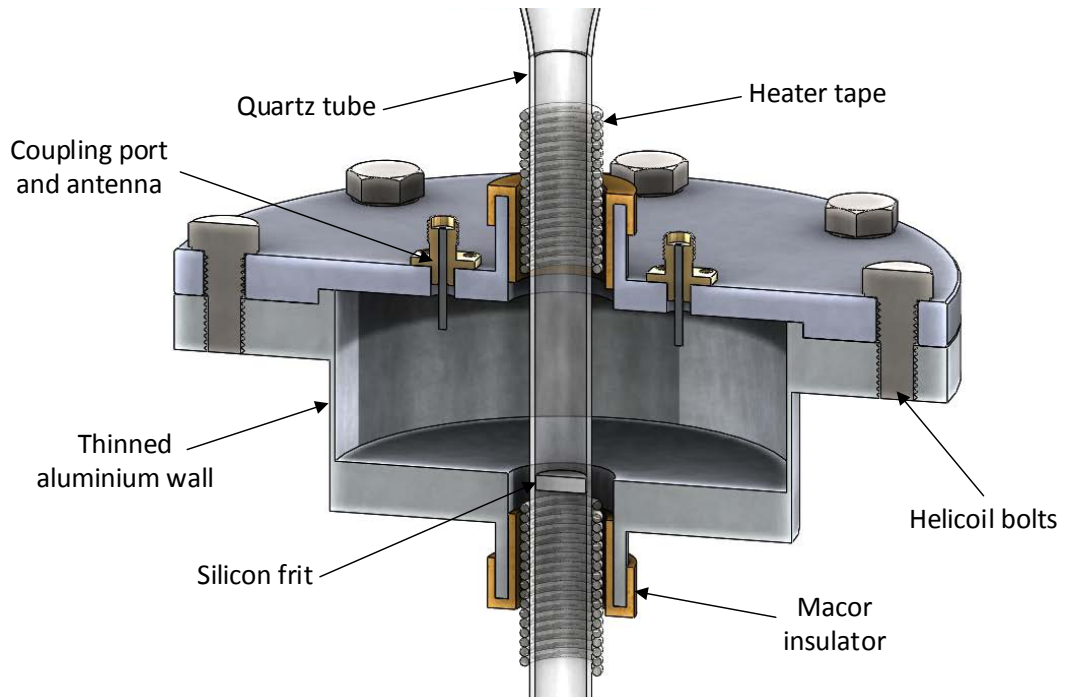
Figure 6.1 – Microwave cavity design for use in simultaneous heating and neutron diffraction showing insulating and heating parts.

6.4.2 Electromagnetic design

The electromagnetic design follows the same processes as detailed in section 3.1.2, with the internal radius and height of the cavity determining the electromagnetic properties. To heat the sample effectively the heater tapes need to be as close to the sample as possible. Because the tapes cannot be within the cavity space as detailed in section 6.4.4 they have to be above and below the cavity space. Due to this, the cavity height is intended to be as short as possible, while maintaining the 2 cm neutron beam window. As the cavity height does affect the frequencies of the cavity modes of interest, TM_{010} and TM_{210}, the radius was kept close to its previous value and was chosen to be 45 mm. This gives a theoretical operating frequency of TM_{010} for the empty cavity of 2.55 GHz from Equation 3.2.
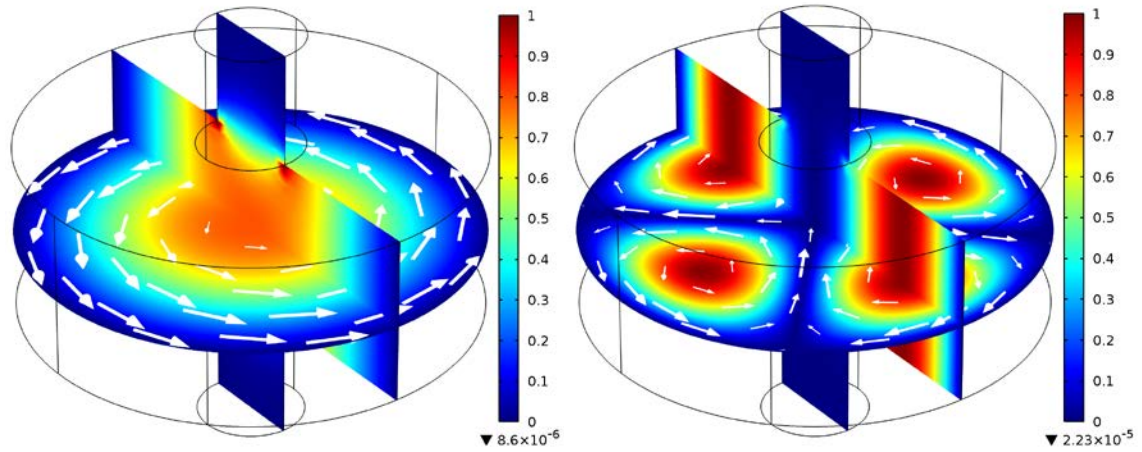
Figure 6.2 – COMSOL field distribution of TM$_{010}$ (left) and TM$_{210}$ (right) showing normalised electric filed distribution (colour scale) and magnetic field distribution (arrows).

The cavity also has the same dimensions of RF chokes as the previous design. The minimum internal cavity height to retain the 2 cm neutron beam window was found to be 3.4 cm, owing to the height needed to fit the structure for clamping the two pieces of the cavity structure together, as shown in appendix 8.2.4. The field distributions of the two desired modes are shown in Figure 6.2, with no appreciable differences to that shown in Figure 3.2. A major difference in changing the cavity dimensions is the mode distribution shown in Table 6.1. The smaller cavity height pushes up the resonant frequency of many unwanted TE and TM modes. Therefore the spectrum is sparse and modes like TM$_{020}$ are more viable to be used in measurement, as there is less possibility for other modes to interfere with it. Theoretically, the smaller cavity dimensions would yield a lower Q factor than that of the previous design, but as shown in section 6.4.3 this is not the case due to the use of two aluminium plates rather than three, which offsets this reduction in Q.

Table 6.1 – Theoretical mode distribution across the frequency spectrum for proposed MCR, labelled resonant modes of interest.
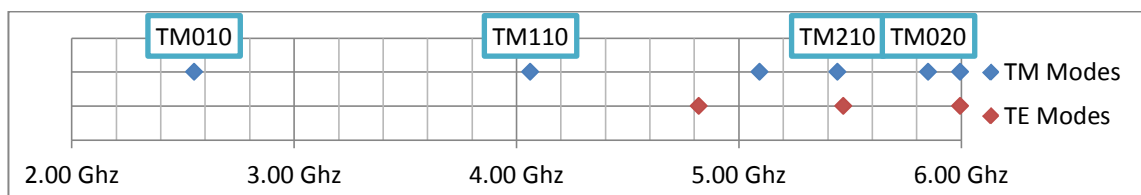
6.4.3 Calibration

As in section 3.1.4, important properties of the cavity for dielectric measurement (such as effective volume) are attained through calibration methods and are shown in Table 6.2. The resonant frequency measured was slightly higher than in simulations, most likely due to tolerances in construction. The predicted Q factor from Equation 3.1 was 12549, less than that of the original cavity discussed in section 3.1. However the measured Q factor of TM_{010} of this cavity was 7676, higher than the other cavity. This is due to having only two plates rather than three. The effective volume of the cavity was calculated to be 5.82×10^{-5} m^3 for the TM_{010} mode. The measured effective cavity volume by the metal ball calibration method, shown in appendix 8.3.3, was found to be higher than that calculated.

The frequency and bandwidth shift per degree is an important factor to account for in this cavity due to the wide range of temperatures that the cavity will experience. Therefore the range of the temperature ramp was larger than that of the other cavities, 30 to 230 °C. The frequency and bandwidth shift over temperature was for the most part linear, as seen in appendix 8.3.3. However it was found that there was a slight hysteresis between the heating and cooling of the cavity. Also the bandwidth shift shows some non-linear effects around 180 °C.

Table 6.2 – Measured operating properties of MCR modes TM_{010} and TM_{210}.

	TM_{010}	TM_{210}
Resonant frequency (GHz)	2.5729	5.4257
Resonant bandwidth (KHz)	335.1	1090.1
Insertion loss (dB)	17.39	5.32
Q factor	7676	4979
Effective volume (m^3)	6.094×10^{-5}	N/A
Frequency shift per degree (KHz)	59.097	124.60
Bandwidth shift per degree (KHz)	0.4164	1.8141

The hysteretic effect is much less prominent than that of the previous MCR in section 3.1. This is probably due to smaller differences between the thermal expansion of steel to aluminium and from nylon to aluminium.

6.4.4   Sample heating setup

From the TGA experiments performed in sections 4.3.1 and 4.4.1, the temperatures required to reach full unammoinated products in all the materials tested would need to approach 400 °C. This would be the preferred outcome of the sample heating setup, but a wide range of materials with lower ammonia release temperatures could still be tested if the experimental setup is unable to reach 400 °C (Klerke et al., 2008) (Huang et al., 2010).

The heating equipment used in this setup is a 62H36A5X-1131 Watlow coiled cable heater. The coil gives a surface area to the quartz tube of 13.9 cm^2 and with a recommended sheath watt density of 4.65 W/cm^2 to 11.62 W/cm^2 both of the heaters can provide a combined power of 129.3 W to 323 W. It is yet unknown what percentage of this energy will be transferred to the sample, due to the many variables in the heat transfer process. There is a 1 mm gap between the outside of the heater tape to the thermal insulation and the insulation is 1.5 mm thick. The insulation is intended to be made out of Macor to reduce the heat transfer to the aluminium cavity, due to its low thermal conductivity 1.46 W/mK to aluminium's 236 W/mK (Corning incorporated, 2012) (Kaye & Laby, 1995). As previously stated, the heater tape cannot be placed within the cavity structure. However, as shown from Figure 3.3 the electric field strength reduces dramatically along the length of the RF chokes. This means the heater tape can be placed within the RF choke region without diminishing the dielectric measurement. Figure 6.3 shows the heater tape depth into the RF chokes and its effect on the resonance. From these data a depth of 15 mm was chosen for the heater tape postion because any further depth nearer the cavity space causes adverse effects of insertion loss and reduced Q factor.
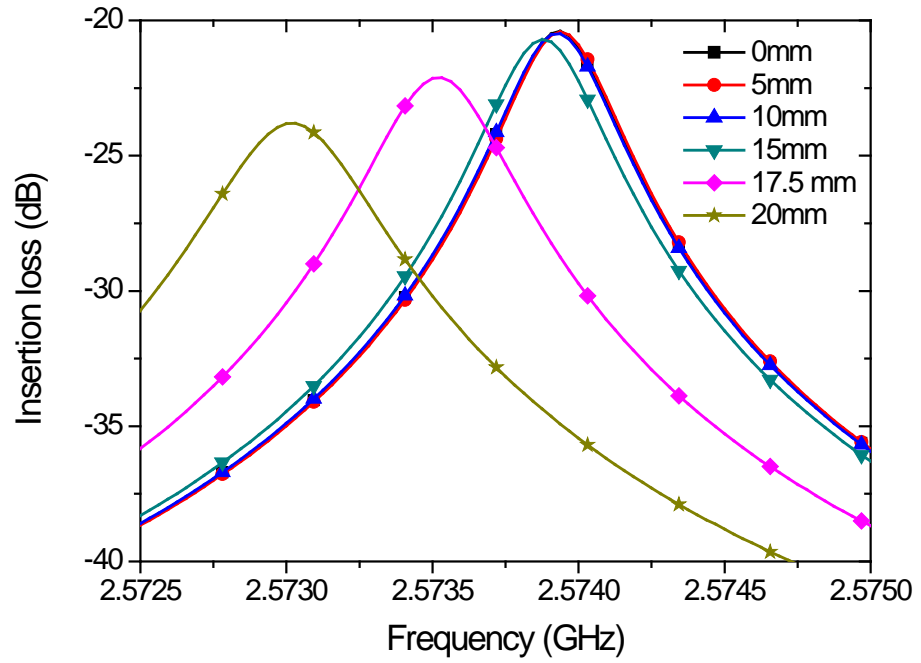
Figure 6.3 – Effect of heater position within the RF chokes (0 mm top of RF choke) on the performance of MCR.

6.5 Capabilities and expected outcomes

In terms of quality of measurement, neutron diffraction should have no change to that seen in chapter 4, due to the same amount of aluminium in the path of the beam and the formation of dual peaks, as shown in Figure 4.4. The quality of dielectric results is expected to improve, due to the improved Q factor. This will improve the SNR and give more freedom on types and quantity of samples that can be tested.

The types of measurement that can be conducted are the same ammonia adsorption experiments as detailed in previous chapters, but now also in situ heating can be performed to the ammoniated samples prior to measurement (Tamimi & McIntosh, 2014). By heating, two important pieces of information can be determined. Firstly, if there is appropriate calibration of the heating profile. The sample can be heated to specific temperatures and the structural and dielectric properties can be attained for the various coordination complexes of the materials (Sitepu et al., 2002). Secondly, experiments can be conducted in cyclic uptake and release of ammonia (Makepeace et al., 2014). This will give information on how much of the ammonia is recoverable from the material and if subsequent ammoniation of the material yields lower adsorbed ammonia. The out-gas mass spectrometry can also be used to determine if there are any decomposed products from the heating of the material.

In conclusion, the new application of integrated heating will be able to provide a more comprehensive measurement of ammonia storage methods. This experimental setup could be used for measuring a wide range of gas adsorption and release processes.

7   Works Cited

Air Liquide, 2013. *Air Liquide gas encylopedia*. [Online] (1) Available at: http://encyclopedia.airliquide.com/encyclopedia.asp?LanguageID=11 [Accessed 25 march 2015].

Akutagawa, T., Takeda, S., Hasegawa, T. & Nakamura, T., 2004. Proton transfer and a dielectric phase transition in the molecular conductor (HDABCO+)2(TCNQ)3. *Journal of the American Chemical Society*, 126(1), pp.291-94.

Alamo, R. & Mandelkern, L., 2003. Origins of endothermic peaks in differential scanning calorimetry. *Journal of Polymer Science Part B*, 24(9), pp.2087-105.

Altarawneh, M., Marashdeh, A. & Dlugogorski, B., 2015. Structures, electronic properties and stability phase diagrams for copper(i / ii) bromide surfaces. *Phys. Chem. Chem. Phys.*, 17(14), pp.9341-51.

Amalina, M. & Rusop, M., 2013. The Properties of P-type Copper (I) Iodide (CuI) as a Hole Conductor for Solid-State Dye Sensitized Solar. In *Micro and Nanoelectronics (RSM), 2013 IEEE Regional Symposium*. Langkawi, 2013. IEEE.

Ammitzbóll, A. et al., 2013. Surface adsorption in strontium chloride ammines. *The Journal of Chemical Physics*, 138(16), p.164701.

Aoki, T., Ichikawa, T., Miyaoka, H. & Kojima, Y., 2014. Thermodynamics on Ammonia Absorption of Metal Halides and Borohydrides. *Journal of Physical Chemistry*, 118, pp.18412-16.

Atkins, P., 1990. *Physical Chemistry*. 4th ed. Oxford: Oxford University Press.

Bandosz, T. & Petit, C., 2009. On the reactive adsorption of ammonia on activated carbons modified by impregnation with inorganic compounds. *Journal of Colloid and Interface Science*, 338(2), pp.329-45.

Bauschlicher, C., Langhoff, H. & Partridge, H., 1995. The binding energies of Cu + –(H2O) n and Cu + –(NH3) n (n = 1 – 4). *The Journal of Chemical Physics*, 94, pp.2068-71.

Bendahan, M. et al., 2003. Development of an ammonia gas sensor. *Sensors and Actuators B: Chemical*, 95, pp.170-76.

Bertin, E. et al., 1957. Infrared Absorption Studies of Inorganic Coordination Complexes. XIII. Hexamminecobalt(I1) Halides and Diamminemercury(I1) Halides. *J. Am. Chem. Soc*, 80(3), p.525–527.

Bialy, A. et al., 2015. Solid solution barium–strontium chlorides with tunable ammonia desorption properties and superior storage capacity. *Journal of Solid State Chemistry*, 221, pp.32-36.

Billaud, G. & Demortler, A., 1975. Dielectric Constant of Liquid Ammonia from -35 to +50C and its Influence on the Association between Solvated Electrons and Cation. *The Journal of Phyiscal Chemistry*, 76(26), pp.3053-55.

Bone, S., Gascoyne, P. & Pethig, R., 1977. Dielectric Properties of Hydrated Proteins at 9.9 GHz. *J. Chem. Soc*, 73, pp.1605-11.

Bourdel, E., Pasquet, D., Denorme, P. & Roussel, A., 2000. Measurement of the Moisture Content with a Cylindrical Resonating Cavity in TM010 Mode. *IEEE Transactions on Instrumentation and Measurement*, 49(5), pp.1023-28.

Bragg, W.L., 1913. The Diffraction of Short Electromagnetic Waves by a Crystal. *Proceedings of the Cambridge Philosophical Society*, 17, pp.43-57.

Breitschwerdt, K. & Schmidt, W., 1970. Permittivity and Dielectric Relaxations in Liquid-Ammonia Solutions. *Z.Naturforsch*, 25(a), pp.1467-71.

Britt, D., Tranchemontagne, D. & Yaghi, O., 2008. Metal-organic frameworks with high capacity and selectivity for harmful gases. *PNAS*, 105(33), p.11623–11627.

Brown, M., 2001. *Introduction to Thermal Analysis: Techniques and Applications*. 2nd ed. Dordrecht: Kluwer Academic.

Brown, T., Lemay, H. & Bursten, B., 1991. *Chemistry: The Central Science*. 5th ed. Prentice Hall.

Bykov, Y., Rybakov, K. & Semenov, V., 2000. High-temperature microwave processing. *J. Phys. D: Appl Phys*, 34, pp.55-75.

Chan, W., 1999. Binding of ammonia to small copper and silver clusters. *Chemical Physics Letters*, 315, pp.257-65.

Chieux, P. & Bertagnolli, H., 1984. Deuterated Llquid Ammonia and 7LZ.4ND, Solution. A Neutron Scattering Investigation. *J. Phys. Chem*, 88, pp.3726-30.

Choi, H. et al., 2014. Design of Continuous Non-Invasive Blood Glucose Monitoring Sensor Based on a Microwave Split Ring Resonator. In *RF and Wireless Technologies for Biomedical and Healthcare Applications (IMWS-Bio), 2014 IEEE MTT-S International Microwave Workshop Series on*. London , 2014. IEEE.

Christensen, C. et al., 2005. Metal ammine complexes for hydrogen storage. *Journal of Materials Chemistry*, 15(38), pp.4106-08.

Coats, A. & Redfern, J., 1963. Thermogravimetric Analysis. *Analyst*, 88, pp.906-24.

Collins, D. & Zhou, H., 2007. Hydrogen storage in metal–organic frameworks. *Journal of Materials Chemistry*, 17(30), pp.31-54.

Corning incorporated, 2012. *Macore Machinable Glass Ceramic For Industrial Applications*. Data sheet. New york: Corning Incorporated.

Credendino, R. et al., 2009. Periodic DFT modeling of bulk and surface properties of MgCl2. *Physical chemistry chemical physics*, 11(30), pp.6525-32.

Cuenca, J. et al., 2015. Microwave determination of sp2 carbon fraction in nanodiamond powders. *Carbon*, 81, pp.174-78.

Cumaranatunge, L. et al., 2007. Ammonia is a hydrogen carrier in the regeneration of Pt/BaO/Al2O3 NOx traps with H2. *Journal of Catalysis*, 246(1), pp.29-34.

Dankov, P., Stefanov, P., Gueorguiev, V. & Ivanov, T., 2010. Hairpin-resonator probe design and measurement considerations. In *Journal of Physics: Conference Series 207.*, 2010. IOP.

Darkrim, F., Malbrunot, P. & Tartaglia, G.P., 2002. Review of hydrogen storage by adsorption in carbon nanotubes. *International Journal of Hydrogen Energy*, 27(2), pp.193-202.

Davies, M., 1954. Dielectric Absorption. *Q. Rev. Chem. Soc*, 8, pp.250-78.

Desiraju, G. & Steiner, T., 1999. *The Weak Hydrogen Bond*. 1st ed. Oxford: Oxford University Press.

Distler, T. & Vaughan, P., 1967. The Crystal Structures of the Hexaamminecopper(I1) Halides. *Inorganic Chemistry*, 6(1), pp.126-29.

Dorrepaal, J., 1984. Revised crystal data for magnesium dichloride, MgCl2. *Journal of Applied Crystallography*, 17(6), p.483.

EDF energy, 2015. *How secure are UK gas supplies*. [Online] Available at: https://www.edfenergy.com/energyfuture/energy-gap-security/gas-and-the-energy-gap-security [Accessed 24 march 2015].

Eichelbaum, M. et al., 2012. The microwave cavity perturbation technique for contact-free and in situ electrical conductivity measurements in catalysis and materials science. *Physical Chemistry Chemical Physics : PCCP*, 14(3), pp.1302-12.

Elmøe, T. et al., 2006. A high-density ammonia storage/delivery system based on Mg(NH3)6Cl2 for – in vehicles. *Chemical Engineering Science*, 61(8), pp.2618-25.

Ewing, M. & Royal, D., 2002. A highly stable cylindrical microwave cavity resonator for the measurement of the relative permittivities of gases. *J.chem. Thermodynamics*, 34, pp.1073-88.

Fischer, H.E., Barnes, A.C. & Salmon, P.S., 2006. Neutron and x-ray diffraction studies of liquids and glasses. *Reports on Progress in Physics*, 69(1), pp.233-99.

Fish, K., Miller, R. & Smyth, C., 1958. Microwave Absorption and Molecular Structure in Liquids. XXIV. The Dielectric Relaxation of Liquid Ammonia. *The Journal of Chemical Physics*, 29(4), p.745.

Fröhlich , H., 1948. General theory of the static dielectric constant. *Trans. Faraday Soc*, 44, pp.238-43.

Getty, A. & Schlapbach, L., 2009. Hydrogen-fuelled vehicles. *Nature*, 460(13), pp.809-11.

Gillespie, L. & Gerry, H., 1931. Densities, and partial molal volumes of ammonia, for the ammines of calcium and barium chlorides. *J. Am. Chem. Soc*, 53, pp.3962-68.

Giron, D., 1994. thermochimica acta Thermal analysis characterisation and calorimetric of polymorphs methods in the and solvates. *Thermochimica. Acta*, 248(94), pp.1-59.

Gregory, A. & Clarke, R., 2006. A Review of RF and Microwave Techniques for Dielectric Measurements on Polar Liquids. *IEEE transactions on dielectrics and electrical inslulation*, 13(4), pp.727-43.

Grundmann, M. et al., 2013. Cuprous iodide - A p-type transparent semiconductor: History and novel applications. *Physica Status Solidi (A)*, 210(9), pp.1671-703.

Halevi, E., Haran, E. & Ravid, B., 1967. Dipole moment and polarizability differences between NH3 and ND3. *Chemical physics letters*, 1, pp.475-76.

Hartley, J., Porch, A. & Jones, M., 2015. A non-invasive microwave method for assessing solid-state ammonia storage. *Sensors & Actuators: B. Chemical*, 210, pp.726-30.

Hatakeyama, T. & Quinn, F., 1999. *Thermal Analysis*. 2nd ed. Chichester: John Wiley & Sons Ltd.

Hattenbach, R., 2006. *Transportation & Delivery of Anhydrous Ammonia*. [PDF] Chemical marketing services Available at: http://nh3fuelassociation.org/events-conferences/2006-nh3-fuel-conference/ [Accessed 26 march 2015].

He, B., Preckwinkel, U. & Smith, K., 2003. Comparison Between conventional and Two-Dimensional XRD. In *Denver X-Ray Conference*. Denver, 2003. ICDD.

Hohne, G., Hemminger, W. & Flammersheim, H., 2003. *Differential Scanning Calorimetry*. 2nd ed. New York: Springer.

Hoppe, J. et al., 2014. Open parallel-plate dielectric resonator passive torque sensing. In *Multi-Conference on Systems, Signals & Devices (SSD), 2014 11th International*. Barcelona, 2014. IEEE.

Horowitz, H. & Metzger, G., 1963. A new analysis of thermogravimetric traces. *Analytical chemistry*, 35(10), pp.1464-68.

Huang, Z. et al., 2010. Li2B12H12·7NH3: a new ammine complex for ammonia storage or indirect hydrogen storage. *Journal of Materials Chemistry*, 20(14), pp.2743-45.

Hubbell, J. & Seltzer, S., 1996. *Tables of X-Ray Mass Attenuation Coefficients and Mass Energy-Absorption Coefficients from 1 keV to 20 MeV for Elements Z = 1 to 92 and 48 Additional Substances of Dosimetric Interest**. U.S. DEPARTMENT OF COMMERCE.

Hull, S. et al., 1992. The Polaris powder diffractometer at ISIS. *Physica B: Condensed Matter*, 180-181(2), pp.1000-02.

Ikeda, S., Kuriyama, N. & Kiyobayashi, T., 2008. Simultaneous determination of ammonia emission and hydrogen capacity variation during the cyclic testing for LiNH2-LiH hydrogen storage system. *International Journal of Hydrogen Energy*, 23(21), pp.6201-04.

Iwata, R. et al., 2014. Reaction kinetics of ammonia absorption/desorption of metal salts. *Applied Thermal Engineering*, 72(2), pp.244-49.

Jakubas, R., Galewski, Z., Sobczyk, L. & Matuszewski, J., 1985. Dielectric properties and phase transitions in (CH3NH3)3Sb2Br9. *J. Phys. C: Solid State Phys*, 18, pp.857-60.

Janezic, M. & Baker-Jarvis, J., 1999. Full-wave analysis of a split-cylinder resonator for nondestructive permittivity measurements. *IEEE Transactions on Microwave Theory and Techniques*, 47(10), pp.2014-20.

Johnsen, R., Jensen, P., Norby, P. & Vegge, T., 2014. Temperature- and Pressure-Induced Changes in the Crystal Structure. *Journal of physical chemistry*, 118, pp.24349-56.

Jolly, W., 1956. The Cu-Cu + -Cuff Equilibrium in Liquid Ammonia. *J. Am. Chem. Soc*, 78(19), p.4849.

Jones, M.O., Royse, D.M., Edward, P.P. & David, W.I., 2013. The structure and desorption properties of the ammines of the group II halides. *Chemical Physics*, 427, pp.38-43.

Jonscher, A., 1992. Relaxation of Polarisation. *Applied Physics A*, 55, pp.135-38.

Kaatze, U., 2010. Techniques for measuring the microwave dielectric properties of materials. *Metrologia*, 47(2), pp.91-113.

Kajfez, D., Chebolu, S., Kishk, A. & Abdul-Gaffoor, M., 2001. Temperature dependence of composite microwave cavities. *IEEE Transactions on Microwave Theory and Techniques*, 49(1), pp.80-85.

Kajifez, D., Chebolu, S. & Kishk, A., 1999. Uncertainty analysis of the transmission-type measuremnt of q factor. *IEEE Transactions on Microwave Theory and Techniques*, 47(3), pp.367-71.

Kaye & Laby, 1995. Tables of Physical & Chemical Constants. *Hygrometry*, 16.

Kirby, R., 1956. Thermal Expansion of Polytetrafluorothylene (Teflon) From -190 to +300 C. *Journal of Research of the National Bureau of Standards*, 57(2), pp.91-94.

Klerke, A., Christensen, C., Norskov, J. & Vegge, T., 2008. Ammonia for hydrogen storage:challenges and opportunities. *Journal of Materials Chemistry*, 18, pp.2304-10.

Krupka, J., Derzakowski, K. & Riddle, B., 1998. A dielectric resonator for measurements of complex permittivity of low loss dielectric materials as a function of temperature. *Meas. Sci. Technol*, 9(10), pp.1751-56.

Krupka, J., Geyer, R., Baker-Jarvis, J. & Cermuga, J., 1996. Measurements of the complex permittivity of microwave circuit board substrates using split dielectric resonator and reentrant cavity techniques. In *Dielectric Materials, Measurements and Applications, Seventh International Conference on (Conf. Publ. No. 430)*. Bath, 1996. IET.

Kubota, M., Matsuo, R., Yamanouchi, R. & Matsuda, H., 2014. Absorption and Desorption Characteristics of NH3 with Metal Chlorides for Ammonia Storage. *Journal of Chemical Engineering of Japan*, 47(7), pp.542-48.

Langford, J. & Louert, D., 1996. Powder diffraction. *Rep. Prog. Phys*, 59, pp.131-234.

Langmi, H.W. et al., 2003. Hydrogen adsorption in zeolites A, X, Y and RHO. *Journal of Alloys and Compounds*, 357, pp.710-15.

Lan, R., Irvine, J. & Tao, S., 2012. Ammonia and related chemicals as potential indirect hydrogen storage materials. *International Journal of Hydrogen Energy*, 37(2), pp.1482-94.

Leineweber, A., Friedriszik, M. & Jacobs, H., 1999. Preparation and Crystal Structures of Mg (NH 3) 2 Cl 2 , Mg (NH 3) 2 Br 2 , and Mg (NH 3) 2 I 2. *Journal of Solid State Chemistry*, 147, pp.229-34.

Leineweber, A. & Jacobs, H., 2000. Preparation and Crystal Structures of Ni(NH3)2Cl2 and of Two Modifications of Ni(NH3)2Br2 and Ni(NH3)2I2. *Journal of Solid State Chemistry*, 152(2), pp.381-87.

Leybold, 2014. *Debye-Scherrer photography: determining the lattice plane spacings of polycrystalline powder samples*. [Online] Available at: http://www.leybold-shop.com/vp7-1-2-3.html [Accessed 14 November 2014].

Li, S., Akyel, C. & Bosisio, R., 1981. Precise Calculations and Measurements on the Complex Dielectric Constant of Lossy Materials Using TM010 Cavity Perturbation Techniques. *Microwave Theory and Techniques*, 29(10), pp.1041-48.

Lin, M., Wang, Y. & Afsar, M., 2005. Precision measurement of complex permittivity and premeability by microwave cavity perturbation technique. *Spectroscopy and Material Properties*, 1(5), pp.62-63.

Lovell, R., 1974. Application of Kramers-Kronig relations to the interpretation of dielectric data. *J. Phys. C: Solid State Phys*, 7, pp.4378-84.

Lui, C. & Aika, K., 2004. Ammonia Absorption into Alkaline Earth Metal Halide Mixtures as an Ammonia Storage Material. *Industrial & Engineering Chemistry Research*, 43(23), pp.7484-91.

Luiten, A., Mann, A. & Blair, D., 1999. High-resolution measurement of the temperature-dependence of the Q, coupling and resonant frequency of a microwave resonator. *Measurement Science and Technology*, 7(6), pp.949-53.

Makepeace, J. et al., 2014. In situ X-ray powder diffraction studies of hydrogen storage and release in the Li-N-H system. *Physical Chemistry Chemical Physics : PCCP*, 16(9), pp.4061-70.

Mantas, P., 1999. Dielectric response of materials: extension to the Debye model. *Journal of the European Ceramic Society*, 19, pp.2079-86.

Marand, E., Baker, K. & Graybeal, J., 1992. Comparison of reaction mechanisms of epoxy resins undergoing thermal and microwave cure from in situ measurements of microwave dielectric properties and infrared spectroscopy. *Macromolecules*, 25, pp.2243-52.

Marsland, T. & Evans, S., 1987. Dielectric measurements with an open-ended coaxial probe. *IEE Proceedings H Microwaves, Antennas and Propagation*, 134(4), pp.341-49.

Maxwell, J.C., 1873. *A Treatise on Electricity and Magnetism*. 1st ed. Oxford: Clarendon Press.

Mcintosh, S. et al., 2006. Oxygen Stoichiometry and Chemical Expansion of Ba0.5Sr0.5Co0.8Fe0.2O3-δ Measured by in Situ Neutron Diffraction. *Chem. Matter*, 18(8), pp.2187-93.

Meisner, G. et al., 2006. Hydrogen release from mixtures of lithium borohydride and lithium amide: A phase diagram study. *Journal of Physical Chemistry B*, 110(9), pp.4186-92.

Miki, N., Naonobu, K., Masahiko, S. & Yuichi, M., 1995. Temperature-Programmed Desorption of Ammonia with Readsorption Based on the Derived Theoretical Equation. *J. Phys. Chem.*, 99(21), pp.8812-16.

Milburn, R., Baranov, V., Hopkinson, A. & Bohme, D., 1998. Sequential Ligation of Mg+, Fe+, (c-C5H5)Mg+, and (c-C5H5)Fe+ with Ammonia in the Gas Phase: Transition from Coordination to Solvation in the Sequential Ligation of Mg+. *J. Phys. Chem*, 102, pp.9803-10.

Nakagawa, T. et al., 2007. Observation of hydrogen absorption/desorption reaction processes in Li-Mg-N-H system by in-situ X-ray diffractmetry. *Journal of Alloys and Compounds*, 430(1), pp.217-21.

Naohiko, Y., Hidehiro, O. & Shigeto, A., 1996. Dielectric Properties and Phase Transitions of Ba (Ti 1- xSnx) O 3 Solid Solution. *J. Appl. Phys*, 35, pp.5099-103.

National Research Council, 2003. *International critical tables of Numerical data, Physics, Chemistry and Technology*. 1st ed. New york: Knovel.

Neilson, G.W., Mason, P.E., Ramos, S. & Sullivan, D., 2001. Neutron and X-ray scattering studies of hydration in aqueous solutions. *Phil. Trans. R. Soc. Lond*, 359(A), pp.1575-91.

NETZSCH Group, 2014. *Polymers — Polyethylene terephthalate (PET)*. [Online] (1) Available at: http://www.netzsch-thermal-analysis.com/en/materials-applications/polymers/polymers-polyethylene-terephthalate-pet.html [Accessed 09 march 2015].

Ngai, K., Jonscher, A. & White, C., 1979. On the origin of the universal dielectric response in condensed matter. *Nature*, 277, pp.185-89.

Nobuyuki, T. & Masahiro, K., 1970. The Thermal Decomposition of CuBr2·2NH3 and CuBr2. *Bulletin of the Chemical Society of Japan*, 43(11), pp.3468-71.

O'Neill, J., 1966. Measurement of Specific Heat Functions by Differential Scanning Calorimetry. *Analytical chemistry*, 38(10), pp.1331-36.

Patil, K. & Secco, E., 1971. Metal Halide Ammines. 1. Thermal Analyses, Calorimetry, and Infrared Spectra of Cadmium Halide (Cl, Br, I) Derivatives. *Canadian Journal of Chemistry*, 49, pp.3831-35.

Peng, B. & Chen, J., 2008. Ammonia borane as an efficient and lightweight hydrogen storage medium. *Energy environ Sci*, 1, pp.479-83.

Piejak, R. et al., 2004. The hairpin resonator: A plasma density measuring technique revisited. *Journal of Applied Physics*, 95(7), pp.3785-91.

Poonia, N. & Bajaj, A., 1979. Coordination Chemistry of Alkali and Alkaline Earth Cations. *American Chemical Society*, 79(5), pp.389-445.

Pozar, M., 1998. *Microwave engineering*. Chichester: Wiley & sons.

Pynn, R., 1990. Neutron scattering: a primer. *Los Alamos Science*, 19, pp.1-31.

Ramo, S., Whinnery, J. & Duzer, T., 1994. *Fields and Waves in Communication Electronics*. 3rd ed. John Wiley & Sons.

Rauch, D., Albrecht, G., Kubinski, D. & Moos, R., 2015. A microwave-based method to monitor the ammonia loading of a vanadia-based SCR catalyst. *"Applied Catalysis B, Environmental"*, 165(2), pp.36-42.

Reardon, H. et al., 2012. Ammonia Uptake and Release in the MnX2–NH3 (X = Cl, Br) Systems and Structure of the Mn(NH3)nX2 (n = 6, 2) Ammines. *Crystals*, 2(4), pp.193-212.

Reed, D. & Book, D., 2011. Recent applications of Raman spectroscopy to the study of complex hydrides for hydrogen storage. *Current Opinion in Solid State and Materials Science*, 15(2), pp.62-72.

Richardson, T. et al., 2003. X-ray absorption spectroscopy of transition metal-magnesium hydride thin films. *Journal of Alloys and Compounds*, 356(2), pp.204-07.

Rietveld, H.M., 1967. Line profiles of neutron powder-diffraction peaks for structure refinement. *Acta Cryst*, 22, pp.151-52.

Rietveld, H.M., 1969. A Profile Refinement Method for Nuclear and Magnetic Structures. *J. Appl. Cryst*, 2, pp.65-71.

Roessler, D., 1965. Kramers-Kronig analysis of reflection data. *J. Appl. Phys*, 16, pp.1119-23.

Ross, D., 2006. Hydrogen storage: The major technological barrier to the development of hydrogen fuel cell cars. *Vacuum*, 80(10), pp.1084-89.

S.H.I Examination & Inspection LTD, 2014. *Cyclotron application technology*. [Online] (1) Available at: https://www.shiei.co.jp/english/cyclotron_nrt.html [Accessed 17 November 2014].

Śanchez-Andújar, M. et al., 2010. Characterization of the order-disorder dielectric transition in the hybrid organic-inorganic perovskite-like formate Mn(HCOO)3[(CH 3)2NH2]. *Inorganic Chemistry*, 49(4), pp.1510-16.

Schlapbach, L. & Züttel, A., 2001. Hydrogen-storage materials for mobile applications. *insight review articles*, 414, pp.353-58.

Schubnell, M., 2000. Temperture and heat flow calibration of a DSC-instrument in the temperture range between - 100 and 160 ° C. *Journal of Thermal Analysis and Claorimetry*, 61, pp.91-98.

schuth, F., palkovits, R., Schlogl, R. & Su, D., 2011. Ammonia as a possible element in an energy infrastructure: catalysts for ammonia decomposition. *Energy & Enviromental Science*, pp.6278-89.

Sears, F., 1992. Special Feature Neutron scattering lengths and cross section. *Neutron news*, 3(3), pp.26-37.

Sheen, J., 2009. Comparisons of microwave dielectric property measurements by transmission/reflection techniques and resonance techniques. *Measurement Science and Technology*, 20(4), p.12.

Shportko, K. & Venger, E., 2015. Influence of the local structure in phase-change materials on their dielectric permittivity. *Nanoscale Research Letters*, 10(1), pp.8-11.

Sihvola, A., 1999. *Electromagnetic Mixing Formulas and Applications*. 47th ed. Padstow: IEE.

Sitepu, H. et al., 2002. Neutron diffraction phase analysis during thermal cycling of a Ni-rich NiTi shape memory alloy using the Rietveld method. *Scripta Materialia*, 46(7), pp.543-48.

Siva, D.S., 2011. *Elementary scattering theory for X-ray and neutron users*. Oxford: Oxford university press.

Smith, R., Hull, S. & Armstrong, A., 1994. The POLARIS Powder Diffractometer at ISIS Proceedings of the Third European Powder Diffraction Conference (EPDIC-3). *Mater. Sci. Forum*, pp.166-169, 251-256.

Smith, J. & Wendlandt, W., 1964. The Thermal Decompostion of Metal Complexes-XII. *J. Inort. Nucl. Chem*, 26, pp.1157-63.

Sørensen, R.Z. et al., 2008. Indirect, reversible high-density hydrogen storage in compact metal ammine salts. *Journal of the American Chemical Society*, 130(27), pp.8660-8.

Speakman, S.A., 2014. *Basics of X-Ray Powder Diffraction - MIT*. [PDF] massachusetts institute of technology (1) Available at: http://prism.mit.edu/xray/oldsite/Basics%20of%20X-Ray%20Powder%20Diffraction.pdf [Accessed 13 November 2014].

Stancliff, R. & Dunsmore, J., 2007. *The Evolution of RF/Microwave Network Analyzers*. Aglient technologies journal.

Stodghill, S., 2010. *Thermal Analysis – A Review of Techniques and Applications in the Pharmaceutical Sciences*. [Online] (13) Available at: http://www.americanpharmaceuticalreview.com/Featured-Articles/36776-Thermal-Analysis-A-Review-of-Techniques-and-Applications-in-the-Pharmaceutical-Sciences/ [Accessed 09 march 2015].

Stuchly, S. & Bassey, C., 1998. Microwave coplanar sensors for dielectric measurements. *Meas Sci Technol*, 9, pp.1324-29.

Summan, A., 1999. Electrical Conductivity of Heat Treated Polyacrylonitrile and its Copper Hailde Complexes. *J. Polym. Sci A*, 37, pp.3057-62.

Tamimi, M. & McIntosh, S., 2014. High temperature in situ neutron powder diffraction of oxides. *Journal of Materials Chemistry A*, 2(17), pp.6015-26.

TED PELLA INC, 2015. *PELCO® Technical Notes*. [Online] Available at: https://www.tedpella.com/technote_html/619%20TN.pdf [Accessed 07 may 2015].

Thomas, M., 2009. Adsorption and desorption of hydrogen on metal-organic framework materials for storage applications: comparison with other nanoporous materials. *Dalton transactions (Cambridge, England : 2003)*, (9), pp.1487-505.

Thomas, G. & Parks, G., 2006. *Potential Roles of Ammonia in a Hydrogen Economy*. Study. U.S. Department of energy.

Thompson, S. et al., 2009. Beamline I11 at Diamond: A new instrument for high resolution powder diffraction. *Rev. Sci. Instrum*, 80(7), pp.75-109.

Ting, V. et al., 2009. In situ neutron powder diffraction and structure determination in controlled humidities. *Chemical communications*, 1(48), pp.7527-29.

Toda, A., Tomita, C., Hikosaka, M. & Saruyama, Y., 1997. An application of temperature modulated differential scanning calorimetry to the exothermic process of poly(ethylene terephthalate) crystallization. *polymer communications*, 38(11), pp.2849-52.

Tomlinson, A. & Hathaway, B., 1968. The electronic properties and stereochemistry of the copper(II) ion. Part III. Some penta-ammine complexes. *J. Chem. Soc. A*, pp.1905-09.

Topsoe, N., Topsoe, H. & Dumesic, J., 1995. Vanadia/Titania Catalysts for Selective Catalytic Reduction (SCR) of Nitric-Oxide by Ammonia: I. Combined Temperature-Programmed in-Situ FTIR and On-line Mass-Spectroscopy Studies. *Journal of Catalysis*, 151(1), pp.226-40.

Triggs, N. & Valentini, J., 1992. An Investigation of Hydrogen Bonding In Amides Using Raman Spectroscopy. *J. Phys. Chem*, 96(17), pp.6922-31.

Turner, J., 2004. Sustainable Hydrogen Production. *Science*, 305, pp.972-75.

University of Liverpool, 2000. *Matter*. [Online] (1) Available at: http://www.matter.org.uk/diffraction/x-ray/powder_method.htm [Accessed 14 November 2014].

Villain, S. et al., 1995. Electrical properties of CuI and the phase boundary Cu ¦ CuI. *Solid State Ionics*, 76, pp.229-35.

Von Ardenne, M., Musiol, G. & Klemradt, U., 1990. *Effekte der Physik. Deutsch*. Harri Deutsch.

Waldron, R.A. & Inst, A.P., 1960. Perturbation theory of resonant cavities. *Institution Monograph*, (373), pp.272-74.

Wallace, W.E., R. F. Karllcek, J. & Imamura, H., 1979. Mechanism of Hydrogen Absorption by LaNi5. *Journal of Physical Chemistry*, 83(13).

Walton, R. et al., 2001. Real Time Observation of the Hydrothermal Crystallization of Barium Titanate Using in Situ Neutron Powder Diffraction. *J. Am. Chem. Soc*, 123(1), pp.12547-55.

Wang, F., Shi, Z. & Chen, K., 2011. Research of coupling coefficient extraction of a cavity resonator. In *Microwave conference proceedings*. Hangzhou, 2011. IEEE.

Weast, R.C., Astle, M.J. & Beyer, W.H., 1983. *CRC Handbook of Chemistry and Physics*. Boca Raton: CRC Press.

Wendlandt, W. & Gallagher, P., 1981. Instrumentation. In E. Turi, ed. *Thermal Characterization of Polymeric Materials*. 1st ed. London: Academic Press. pp.3-86.

Werner, A., 1913. On the constitution and configuration of higher-order compounds. *Nobel Lecture*, pp.257-69.

Westman, S., Werner, P., Schuler, T. & Raldow, W., 1981. X-Ray Investigations of Ammines of Alkaline Earth Metal Halides. I. The Structures of CaCl2(NH3)8, CaCl2(NH3)2 and the Decomposition Product CaClOH. *Acta Chemica Scandinavica*, 35, pp.467-72.

Xueping, Z. et al., 2007. Effect of catalyst LaCl3 on hydrogen storage properties oflithiumalanate(LiAlH4). *International Journal of Hydrogen Energy*, 32, pp.4957-60.

Yue, Z. et al., 2006. Chemically activated carbon on a fiberglass substrate for removal of trace atrazine from water. *J. Mater. Chem*, 16, pp.3375-80.

Zaluska, A., Zaluski, L. & Ström–Olsen, J., 1999. Nanocrystalline magnesium for hydrogen storage. *Journal of Alloys and Compounds*, 288(1), pp.217-25.

Zhou, L., 2005. Progress and problems in hydrogen storage methods. *Renewable and Sustainable Energy Reviews*, 9(4), pp.395-408.

Zhu, H. et al., 2009. Large-Scale Synthesis of MgCl 2 · 6NH 3 as an Ammonia Storage Material. *Ind. Eng. Chem. Res*, 48, pp.5317-20.

Zittel, Wurster, W.&., Bolkow, R.&. & Ludwig, 1996. Advantages and Disadvantages of Hydrogen. Hydrogen in the Energy Sector. *Systemtechnik Gmbitt*.

Zou, C., Fothergill, J. & Rowe, S., 2008. The effect of water absorption on the dielectric properties of epoxy nanocomposites. *Dielectrics and Electrical Insulation*, 15(1), pp.106 - 117.

Züttel, A., 2003. Materials for hydrogen storage. *Materials Today*, 6(9), pp.24-33.

8 Appendices

8.1 Derivations

8.1.1 S_{21} derivation of coupled microwave cavity structure

S_{21} from an ABCD transfer matrix for a coupled resonator is shown in Equation 8.1 and the transfer matrix representing the coupling structure (derived from a two port network representation of Figure 2.16) is shown in Equation 8.2.

$$S_{21} = \frac{2}{a + \left(\frac{b}{Z_0}\right) + cZ_0 + d}$$

Equation 8.1

$$\begin{pmatrix} a & b \\ c & d \end{pmatrix} = \begin{pmatrix} \dfrac{m_1}{m_2} & 0 \\ \dfrac{Z}{\omega^2 m_1 m_2} & \dfrac{m_2}{m_1} \end{pmatrix}$$

Equation 8.2

Where Z is the impedance the microwave cavity structure and can be related to resonant frequency.

$$Z = R + j\omega L + \frac{1}{j\omega C}$$

Equation 8.3

$$\omega_0 = \frac{1}{\sqrt{LC}}$$

Equation 8.4

$$Z = R + j\omega_0 L \left(\frac{\omega}{\omega_0} - \frac{\omega_0}{\omega}\right)$$

Equation 8.5

Writing $\Delta\omega = \omega - \omega_0$, for frequencies close to resonance (i.e. $\Delta\omega \ll \omega - \omega_0$, an almost exact approximation for a high Q resonator).

$$Q_0 = \frac{\omega_0 L}{R}$$

Equation 8.6

$$Z \approx R \left(1 + 2jQ_0 \left(\frac{\omega - \omega_0}{\omega}\right)\right)$$

Equation 8.7

Therefore the transfer matrix elements from Equation 8.2 are as shown.

$$a = \pm \frac{m_1}{m_2} \quad b = 0$$

<div align="right">**Equation 8.8**</div>

$$c = \pm \frac{R}{\omega^2 m_1 m_2} \left(1 + 2jQ_0 \left(\frac{\omega - \omega_0}{\omega}\right)\right) \quad d = \pm \frac{m_2}{m_1}$$

Substituting the transfer elements into Equation 8.1 gives the parameters that determine S_{21} in a microwave cavity resonator.

$$S_{21} = \frac{2}{\frac{m_1}{m_2} + \frac{R}{\omega^2 m_1 m_2} \left(1 + 2jQ_0 \left(\frac{\omega - \omega_0}{\omega}\right)\right) Z_0 + \frac{m_2}{m_1}}$$

<div align="right">**Equation 8.9**</div>

8.1.2   Q factor derivation microwave cavity resonator

Q factor is most simply defined in Equation 8.10. Energy stored is defined by the volume integral of the cavity and energy dissipated is defined by the surface integral of the cavity walls.

$$Q = \omega \frac{energy\ stored}{energy\ dissipated} = \omega \frac{U}{P_1 + P_2}$$

<div align="right">**Equation 8.10**</div>

Energy stored is defined as.

$$U = \mu_0 \int_0^d \int_0^{2\pi} \int_0^a H^2 . r\ d_r d_\phi d_z$$

<div align="right">**Equation 8.11**</div>

Energy dissipated in top and bottom plates.

$$P_1 = 2R_s \int_0^{2\pi} \int_0^a H^2 . r\ d_r d_\Phi$$

<div align="right">**Equation 8.12**</div>

Energy dissipated in curved wall.

$$P_2 = R_s \int_0^d \int_0^{2\pi} H^2 . a\ d_\phi d_z$$

<div align="right">**Equation 8.13**</div>

$$Q = \omega \frac{\mu_0 \pi a^2 d H^2}{2\pi a^2 R_s H^2 + 2\pi a R_s d H^2}$$

<div align="right">**Equation 8.14**</div>

$$Q = \frac{\omega \mu_0}{2R_s} \frac{ad}{a + d}$$

<div align="right">**Equation 8.15**</div>

$$Q = \frac{\omega \mu_0}{2R_s \left(\frac{1}{a} + \frac{1}{d}\right)}$$

<div align="right">**Equation 8.16**</div>

8.1.3 Q factor deviation hairpin resonator

Q factor is most simply defined in appendix 8.8. Energy stored is defined by the volume integral of the cavity and energy dissipated is defined by the surface integral of the cavity walls.

$$Q = \omega \frac{energy\ stored}{energy\ dissipated}$$

<div align="right">**Equation 8.17**</div>

Energy stored in hairpin.

$$U = \mu_0 \int_0^l \int_0^w \int_0^d H^2 \, d_x d_y d_z$$

<div align="right">**Equation 8.18**</div>

Energy dissipated in two side plates of hairpin.

$$P_1 = 4R_s \int_0^l \int_0^w H^2 \, d_y d_z$$

<div align="right">**Equation 8.19**</div>

Energy dissipated in bottom plate of hairpin.

$$P_2 = 2R_s \int_0^w \int_0^d H^2 \, d_x d_y$$

<div align="right">**Equation 8.20**</div>

$$Q = \omega \frac{\mu_0 lwd H^2}{4lw R_s H^2 + 2wd R_s H^2}$$

<div align="right">**Equation 8.21**</div>

$$Q = \frac{\omega \mu_0 ld}{2R_s (2l + d)}$$

<div align="right">**Equation 8.22**</div>

$$Q = \frac{\omega \mu_0}{4R_s \left(\frac{1}{2l} + \frac{1}{d}\right)}$$

<div align="right">**Equation 8.23**</div>

8.2 Schematic diagrams

All dimensions are in mm.

8.2.1 Quartz tube schematic
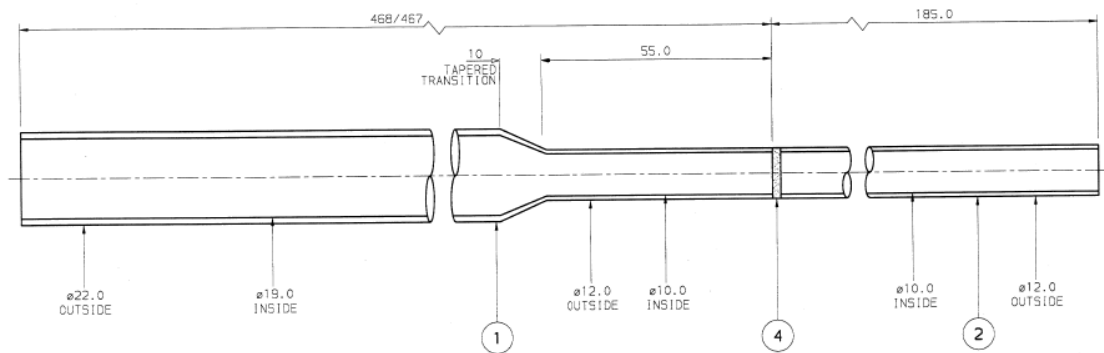
appendix 8.1 – Schematic diagram of quartz tube.

8.2.2 MCR schematic for Simultaneous neutron and microwave measurement
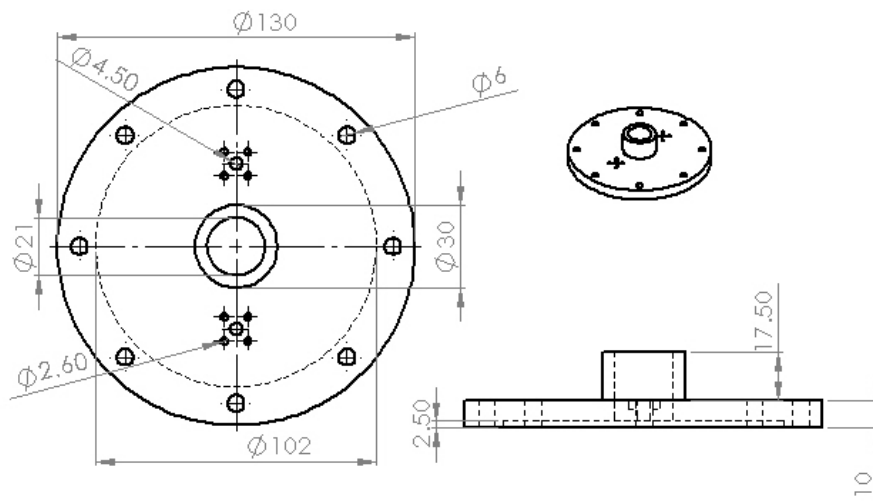
appendix 8.2 – Schematic diagram for top plate for the MCR.
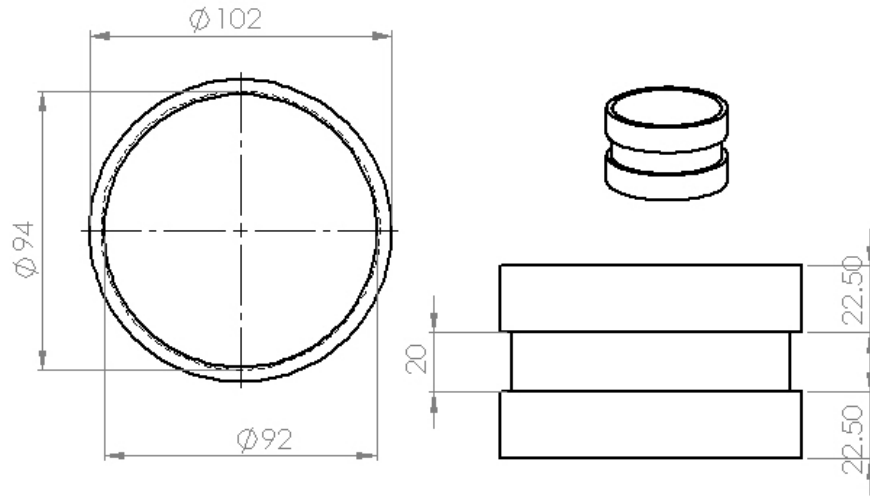
appendix 8.3 – Schematic diagram for middle plate for the MCR.
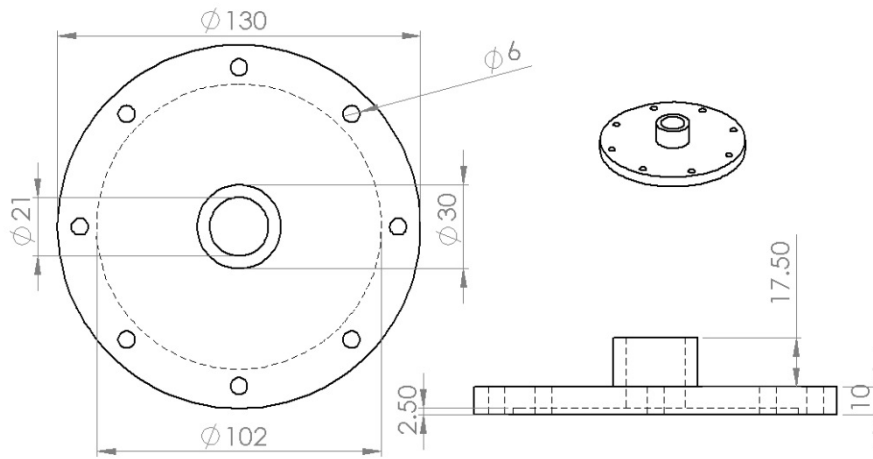
appendix 8.4 – Schematic diagram of bottom plate for the MCR.

8.2.3 Hairpin resonator schematic for Simultaneous XRD and cavity resonance
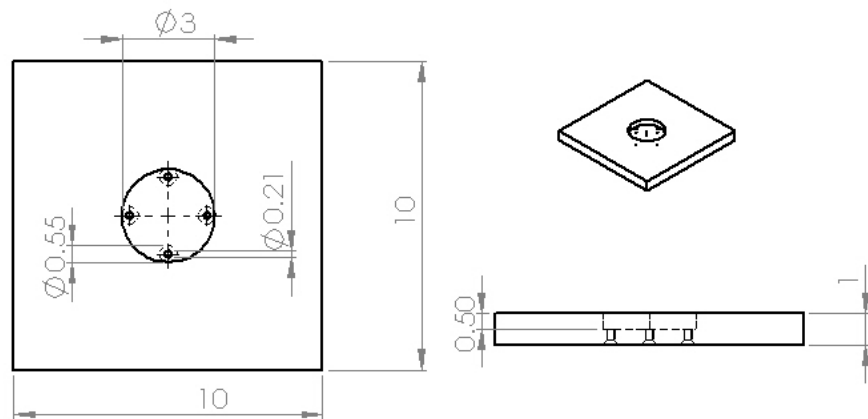
appendix 8.5 – Schematic diagram of base plate for the hairpin resonator.
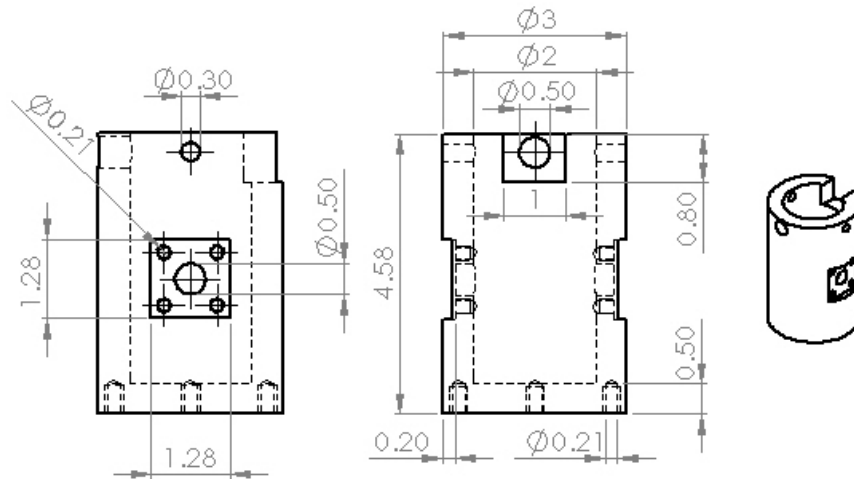
appendix 8.6 – Schematic diagram of enclosure for the hairpin resonator.
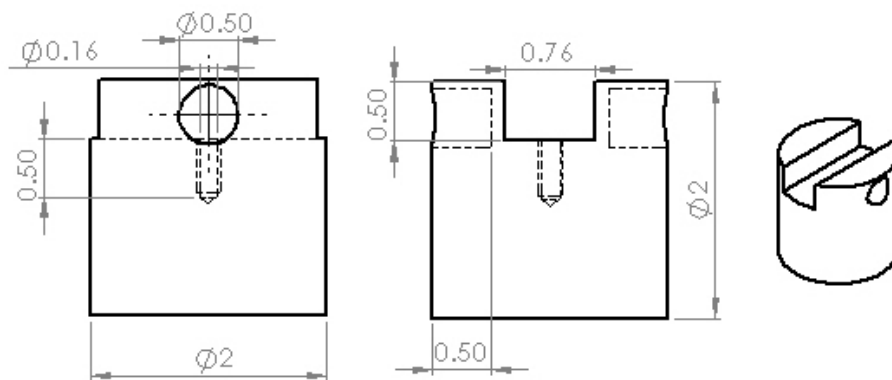
appendix 8.7 – Schematic diagram of PTFE post for the hairpin resonator.
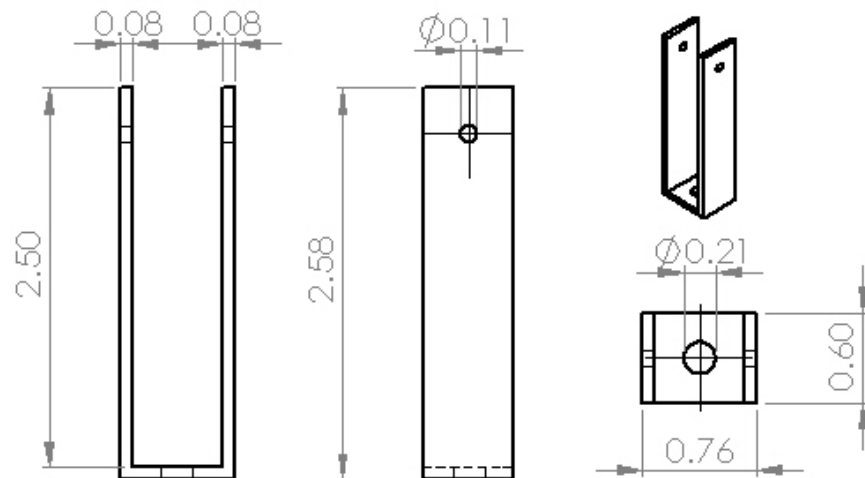
appendix 8.8 – Schematic diagram of hairpin for the hairpin resonator.

8.2.4 MCR schematic for Simultaneous Heating, NPD and cavity resonance
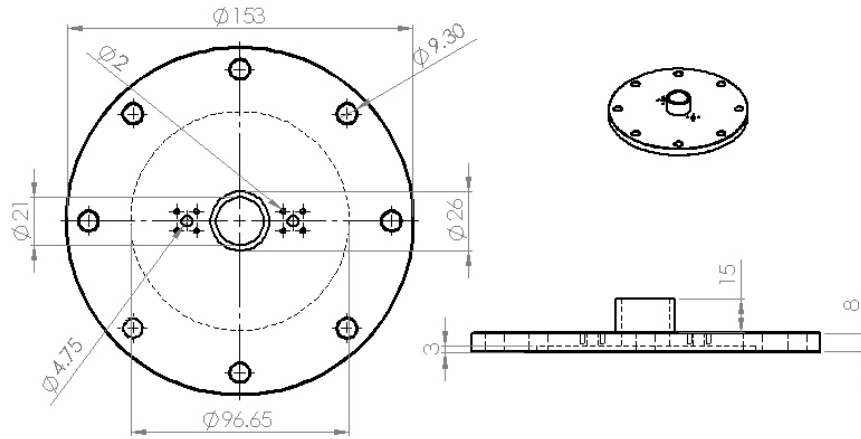
appendix 8.9 – Schematic diagram for top plate for the MCR.
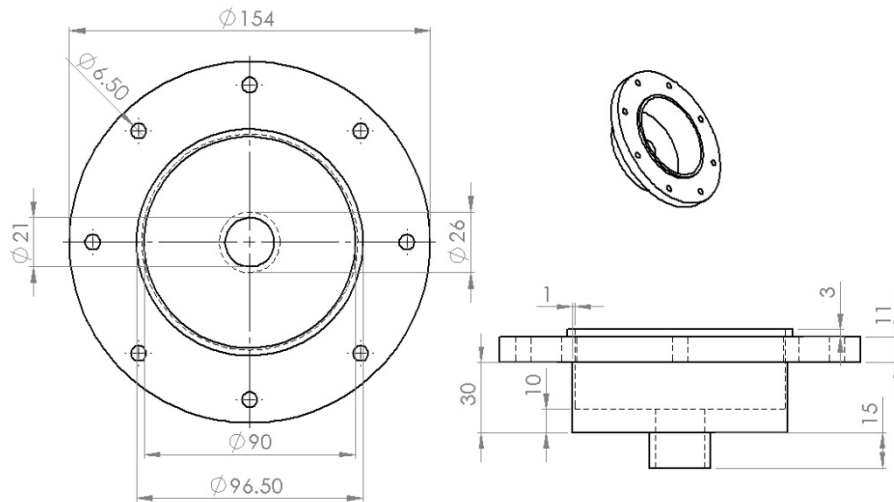
appendix 8.10 – Schematic diagram of bottom plate for the MCR.
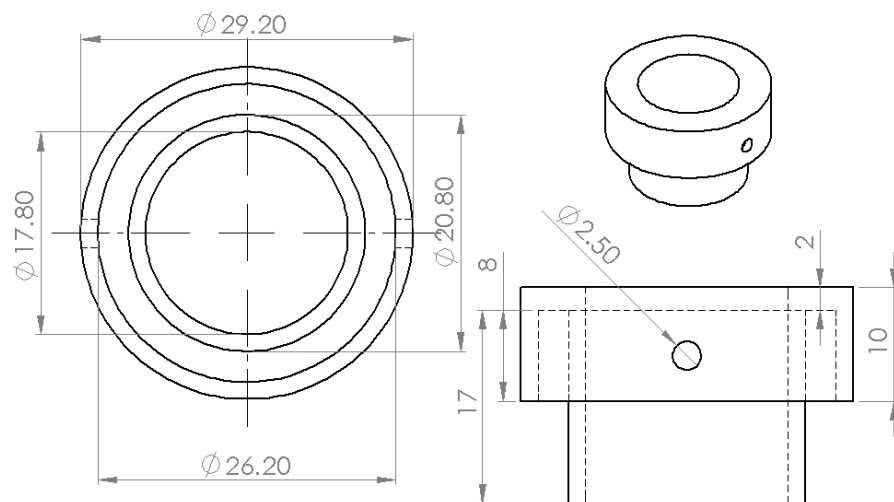
appendix 8.11 – Schematic diagram of insulator.

8.3 Microwave resonator calibration graphs

8.3.1 Microwave cavity resonator for NPD
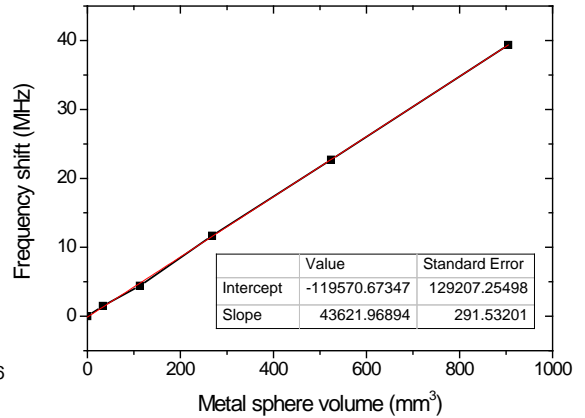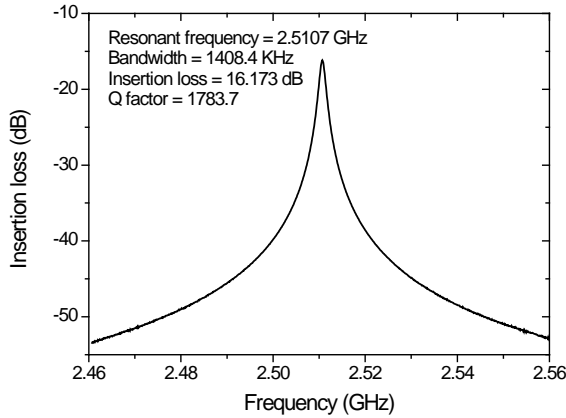
appendix 8.12 – S$_{21}$ trace (left) and calibration for effective volume (right) for mode TM$_{010}$.
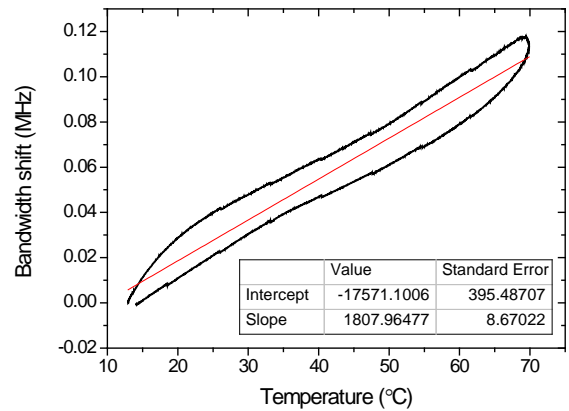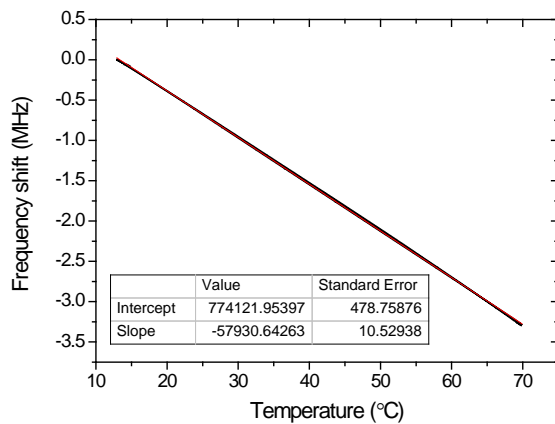
appendix 8.13 – Frequency shift (left) and bandwidth shift (right) of mode TM$_{010}$ under varying temperature.

8.3.2 Hairpin resonator for XRD
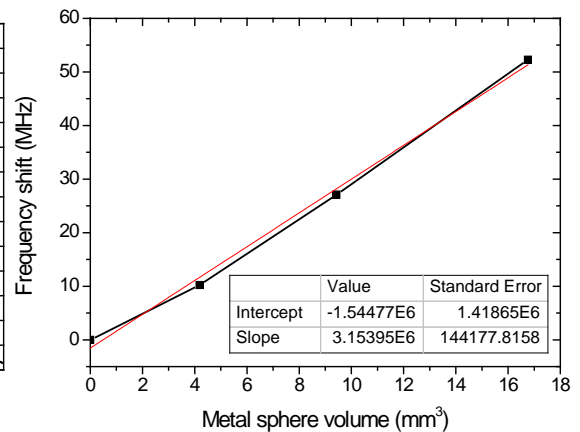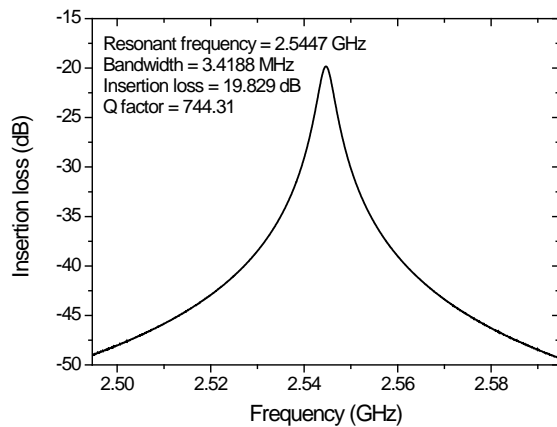
appendix 8.14 – S$_{21}$ trace (left) and calibration for effective volume (right) for mode TM$_{010}$.
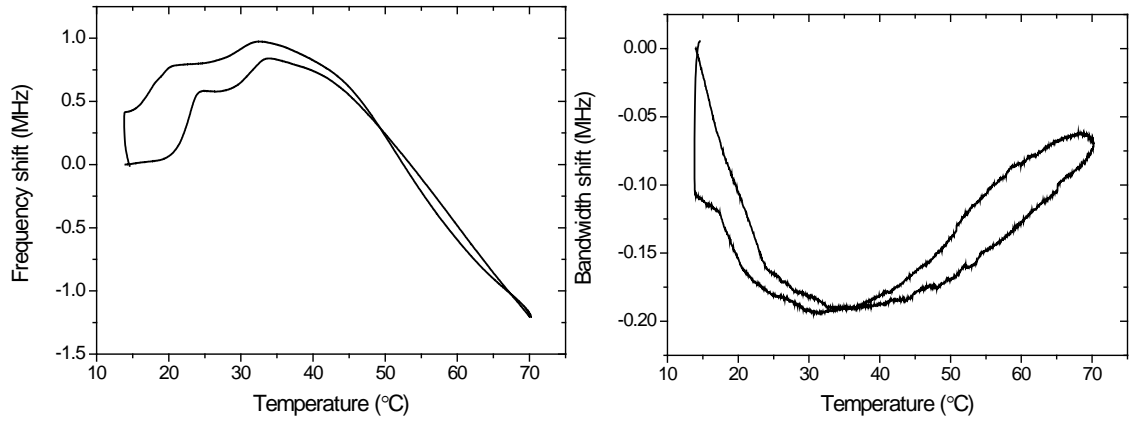
appendix 8.15 – Frequency shift (left) and bandwidth shift (right) of first resonant mode under varying temperature.

8.3.3 Microwave cavity resonator for Heating
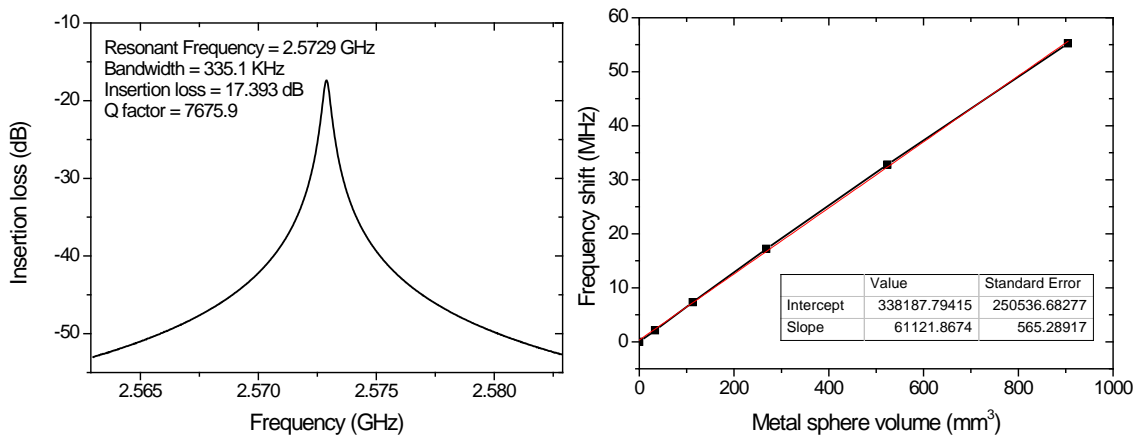
appendix 8.16 – S21 trace (left) and calibration for effective volume (right) for mode TM_{010}.
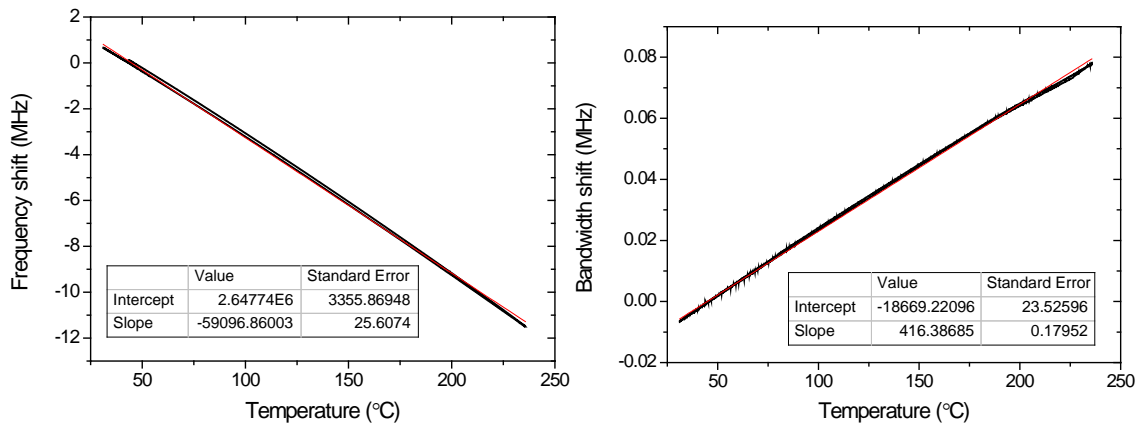
appendix 8.17 – Frequency shift (left) and bandwidth shift (right) of mode TM_{010} under varying temperature.

8.4 Supplementary microwave cavity resonator results

8.4.1 Blood congealing
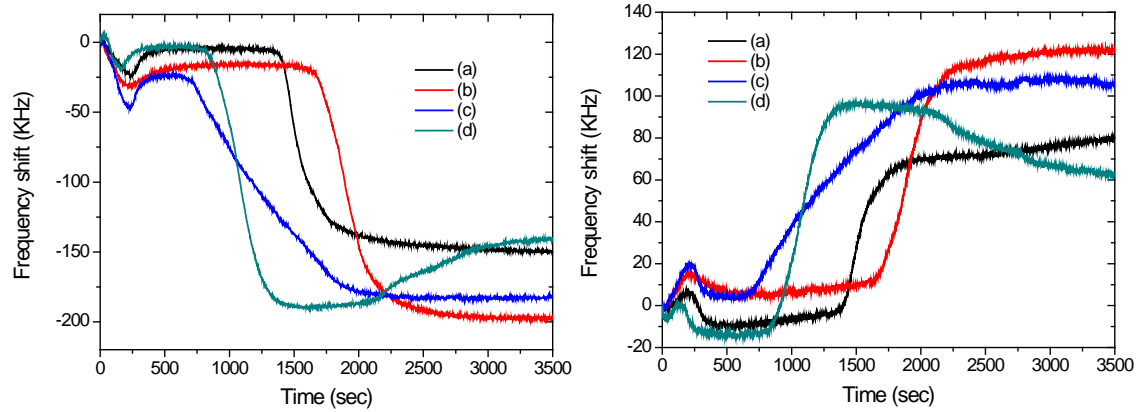
appendix 8.18 – Frequency shift (left) and bandwidth shift (right) of congealing blood in a quartz capillary.

8.4.2 Gas composition changes [1]
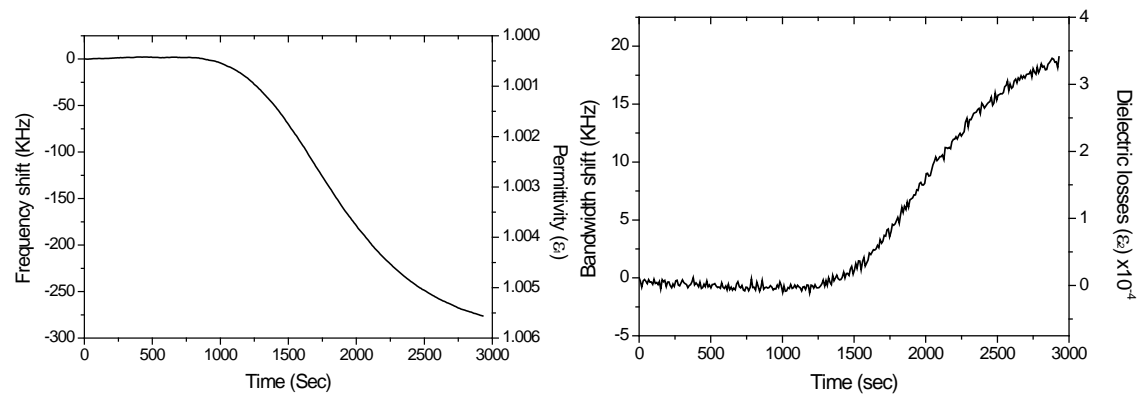
appendix 8.19 – Frequency shift (left) and Bandwidth shift (right) of changing gas composition from Argon to ammonia at gas flow of 10cm³/min.
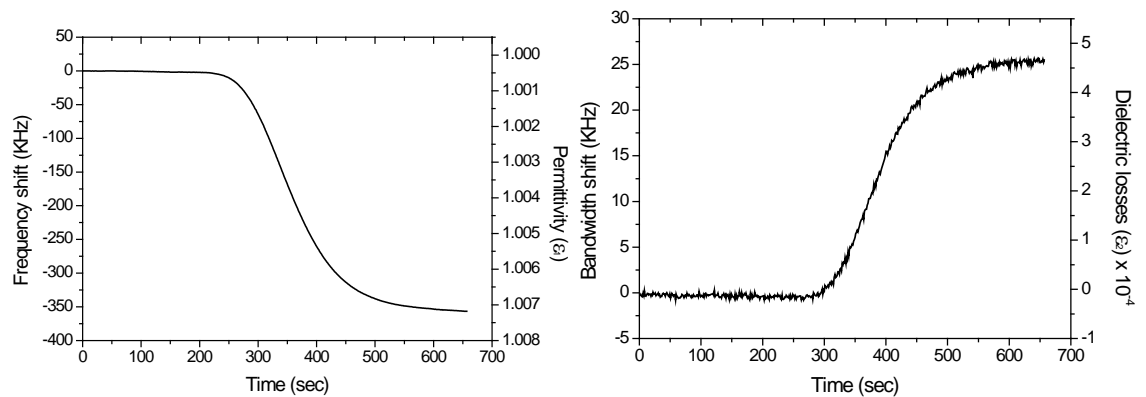
appendix 8.20 – Frequency shift (left) and Bandwidth shift (right) of changing gas composition from Argon to ammonia at gas flow of 40cm³/min.

---

[1] The dielectric losses of initial gases could not be attained therefore values of ε_2 will have an offset error equal to the initial loss in the system.
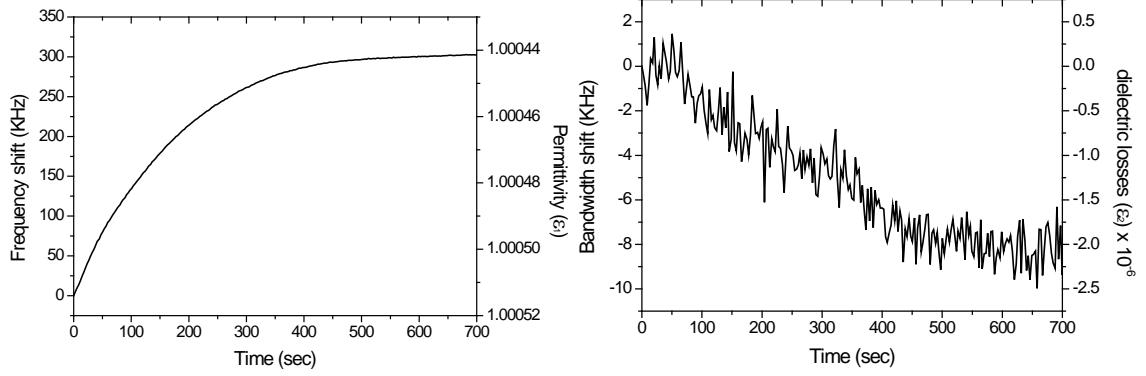
appendix 8.21 – Frequency shift (left) and Bandwidth shift (right) of changing gas composition from air to vacuum under vacuum pump in the POLARIS Vacuum chamber.

8.4.3 Alkali earth halides
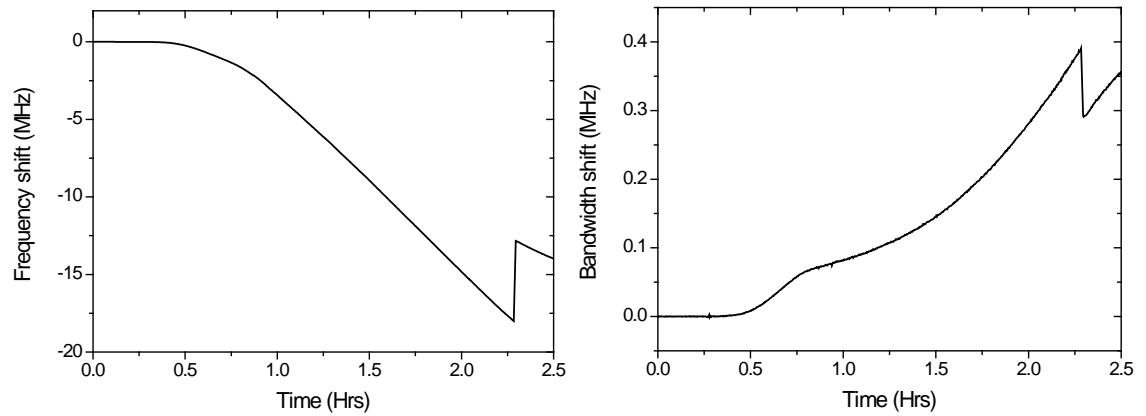
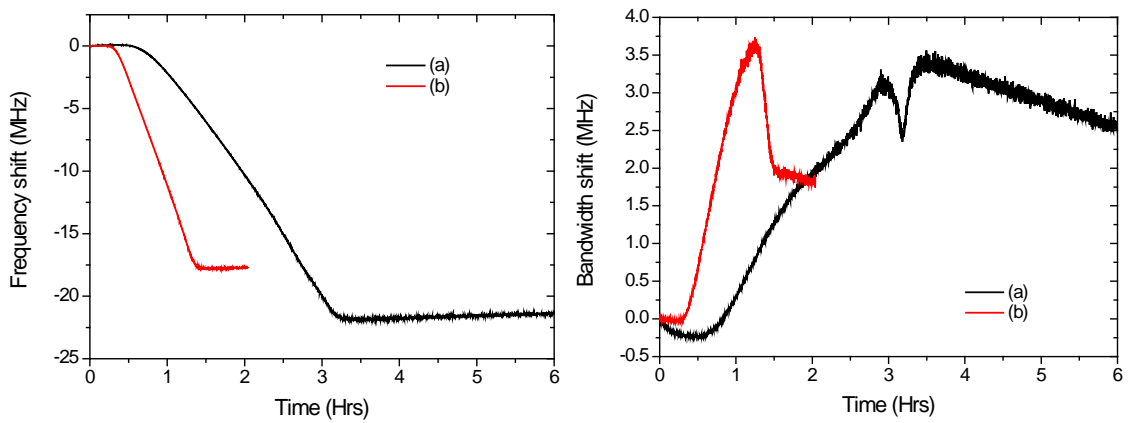**appendix 8.22 – Frequency shift (left) and Bandwidth shift (right) of MgCl$_2$ (unknown quantity) under ammonia gas flow of 10cm^3/min.**
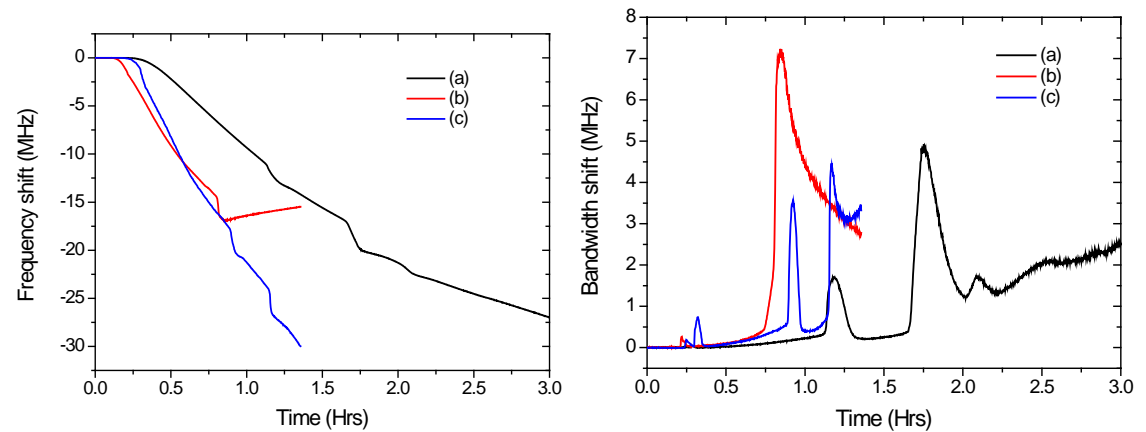
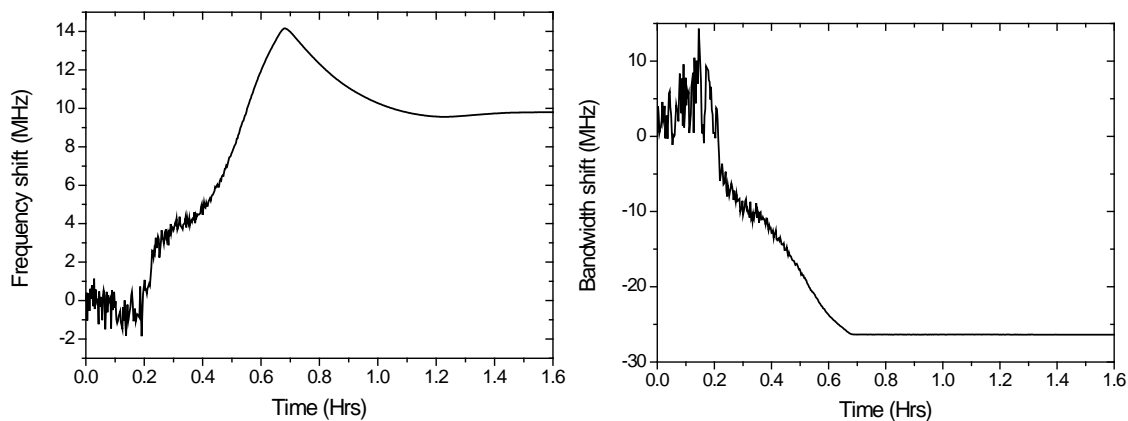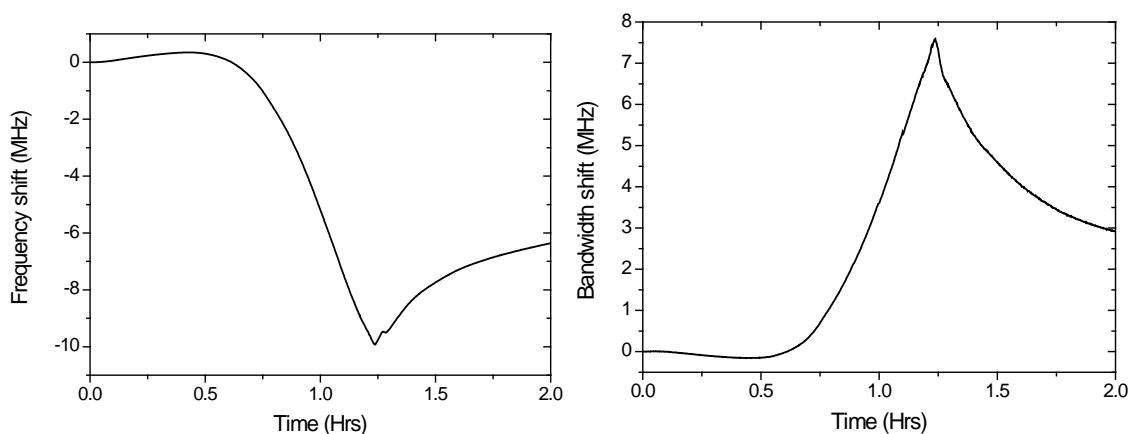**appendix 8.23 – Frequency shift (left) and Bandwidth shift (right) of MgBr$_2$ at sample quantity and ammonia gas flow rate of 2g and 10cm^3/min (a) 1g and 20cm^3/min (b) 2g and 20cm^3/min (c).**
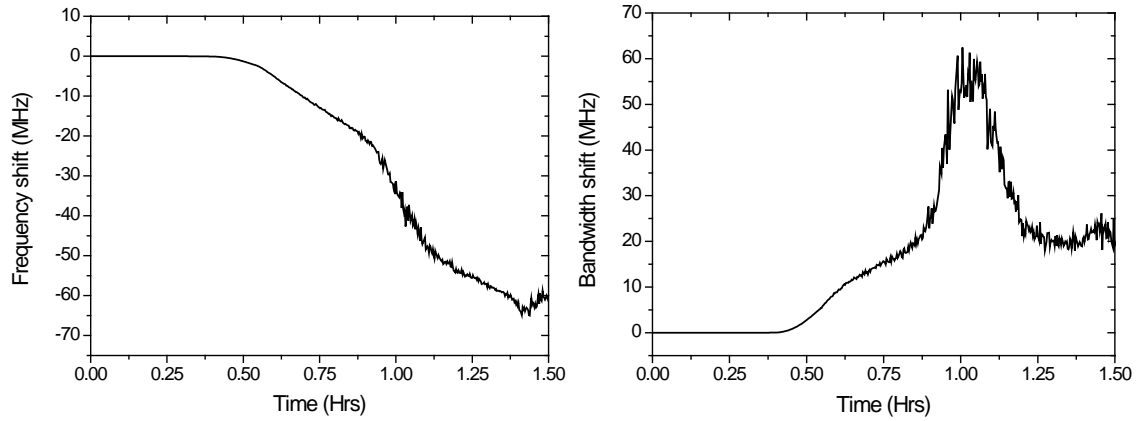
appendix 8.24 – Frequency shift (left) and Bandwidth shift (right) of MgBr$_2$(H$_2$O)$_6$ (unknown quantity) under ammonia gas flow of 10cm^3/min.
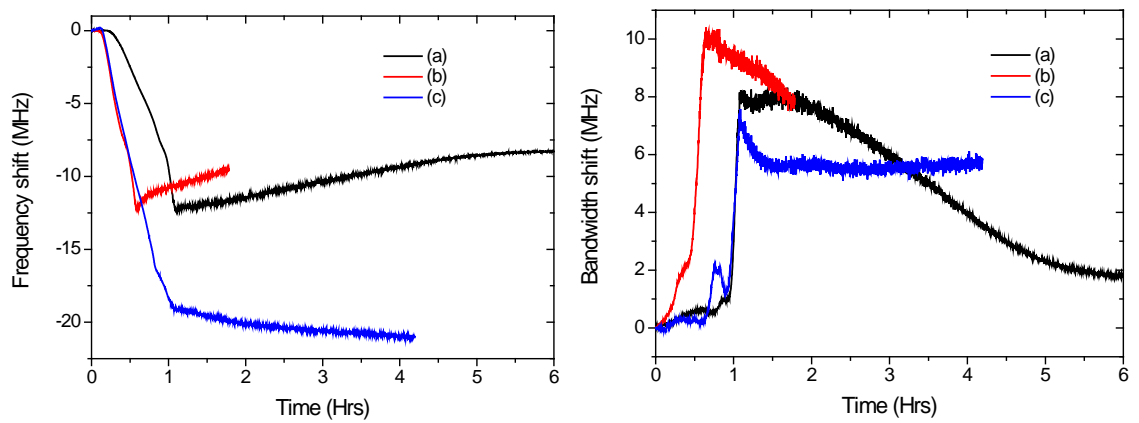
appendix 8.25 – Frequency shift (left) and Bandwidth shift (right) of MgI$_2$ at sample quantity and ammonia gas flow rate of 1g and 10cm^3/min (a) 1g and 20cm^3/min (b) 2g and 20cm^3/min (c).
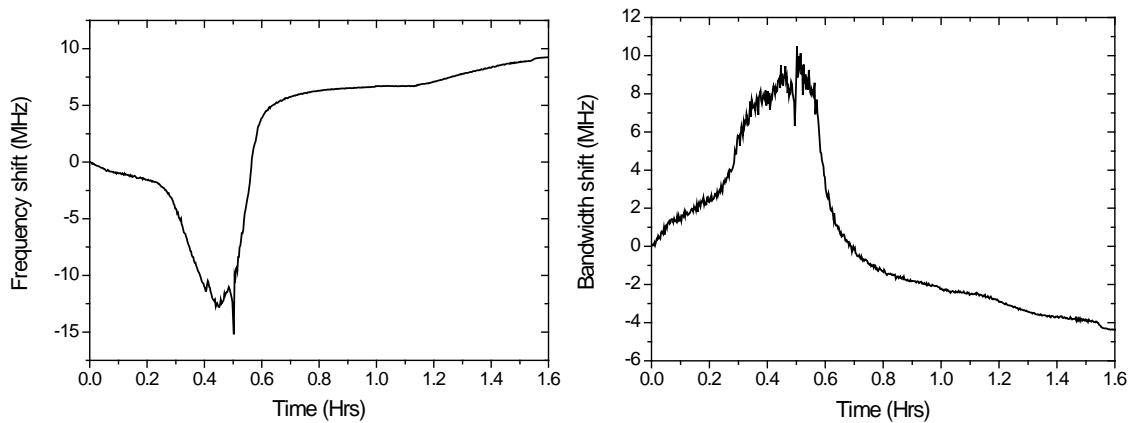
appendix 8.26 – Frequency shift (left) and Bandwidth shift (right) of CaCl$_2$(H$_2$O)$_6$ (unknown quantity) under ammonia gas flow of 10cm^3/min.
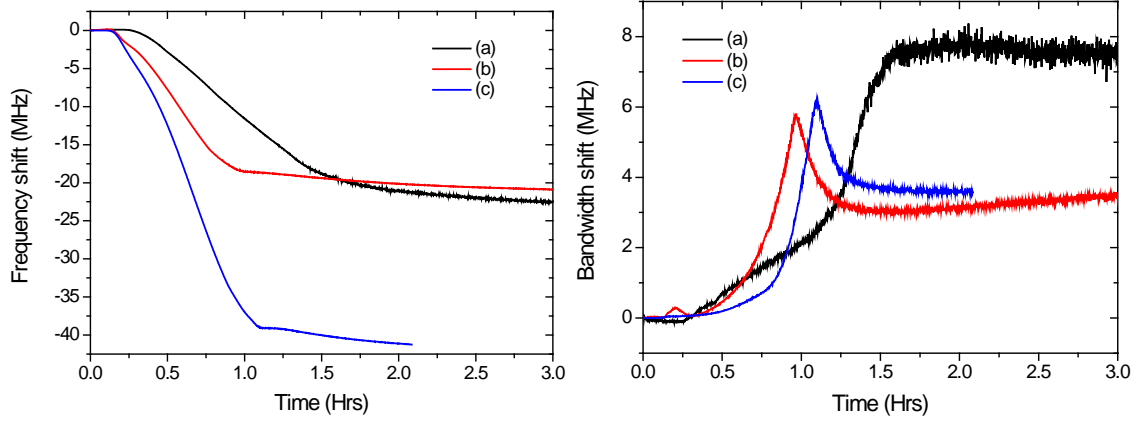
appendix 8.27 – Frequency shift (left) and Bandwidth shift (right) of $CaBr_2$ at sample quantity and ammonia gas flow rate of 1g and 10cm^3/min (a) 1g and 20cm^3/min (b) 2g and 20cm^3/min (c).
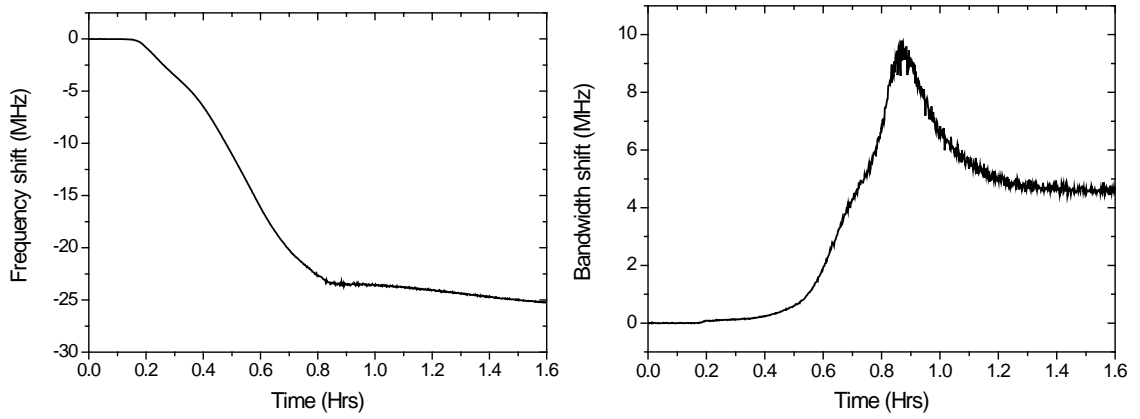
appendix 8.28 – Frequency shift (left) and Bandwidth shift (right) of $CaBr_2(H_2O)_6$ 1g of sample under ammonia gas flow of 20cm^3/min.
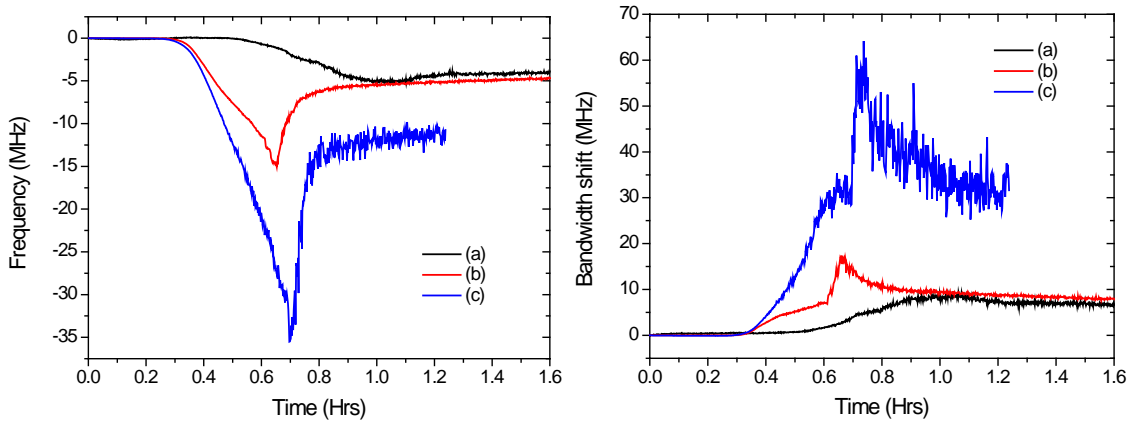
appendix 8.29 – Frequency shift (left) and Bandwidth shift (right) of $CaI_2(H_2O)_6$ at sample quantity and ammonia gas flow rate of 0.5g and 5cm^3/min (a) 0.5g and 10cm^3/min (b) 1g and 10cm^3/min (c).
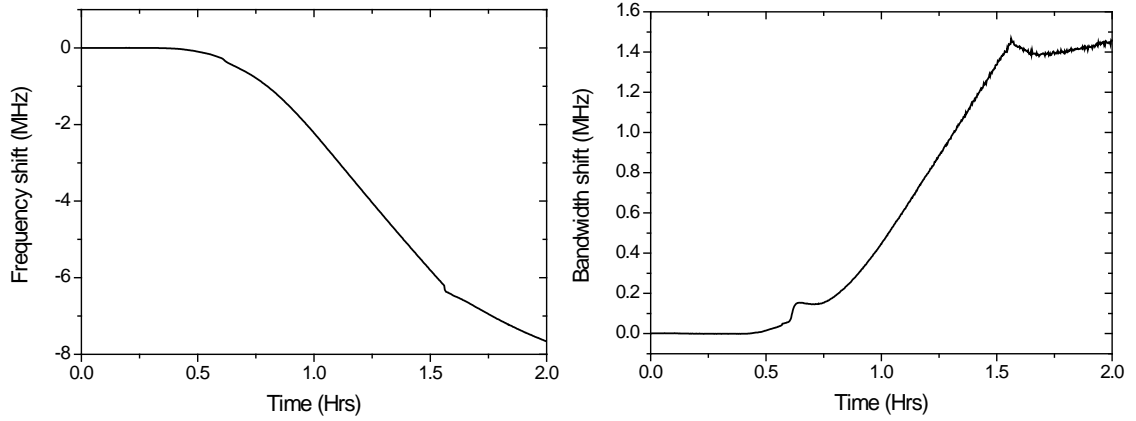
appendix 8.30 – Frequency shift (left) and Bandwidth shift (right) of SrCl$_2$ (unknown quantity) under ammonia gas flow of 10cm^3/min.

8.4.4   Transition metal halides
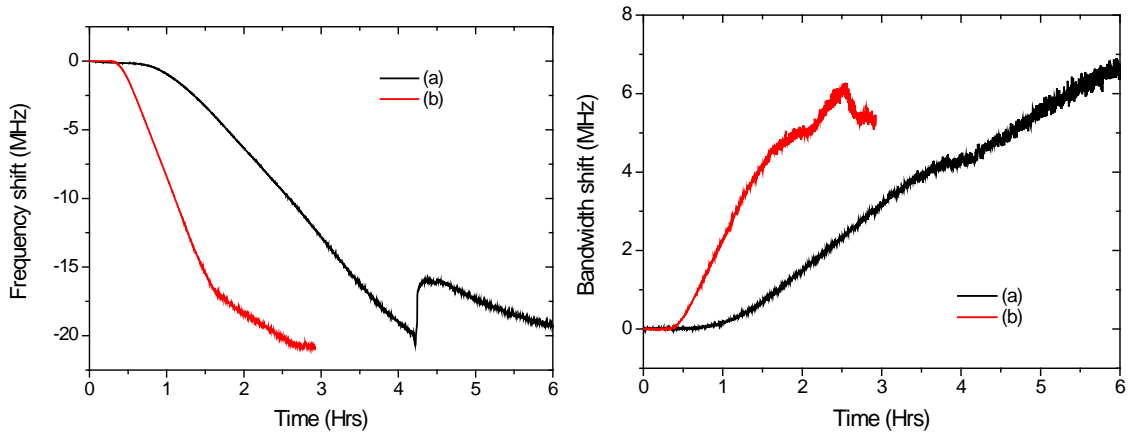
appendix 8.31 – Frequency shift (left) and Bandwidth shift (right) of CuCl$_2$ at sample quantity and ammonia gas flow rate of 1g and 5cm^3/min (a) 1g and 10cm^3/min (b).

appendix 8.32 – Frequency shift (left) and Bandwidth shift (right) of CuBr$_2$ at sample quantity and ammonia gas flow rate of 1g and 5cm^3/min (a) 1g and 10cm^3/min (b).

appendix 8.33 – Frequency shift (left) and Bandwidth shift (right) of CuI 1g of sample under ammonia gas flow of 10cm^3/min.

8.4.5 Metal organic frameworks

appendix 8.34 – Frequency shift (left) and Bandwidth shift (right) of MOF HKUST-1 0.5g of sample under ammonia gas flow of 5cm^3/min.
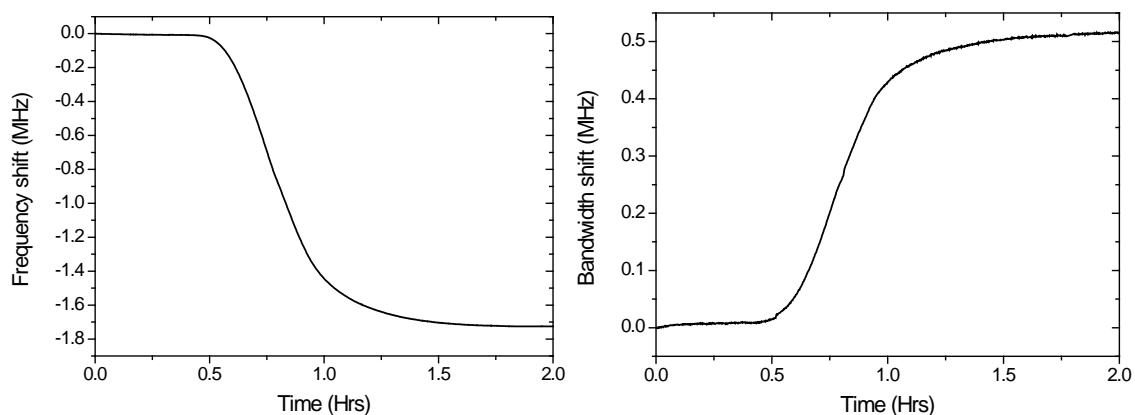
appendix 8.35 – Frequency shift (left) and Bandwidth shift (right) of MOF UIO-67 0.5g of sample under ammonia gas flow of 5cm^3/min.
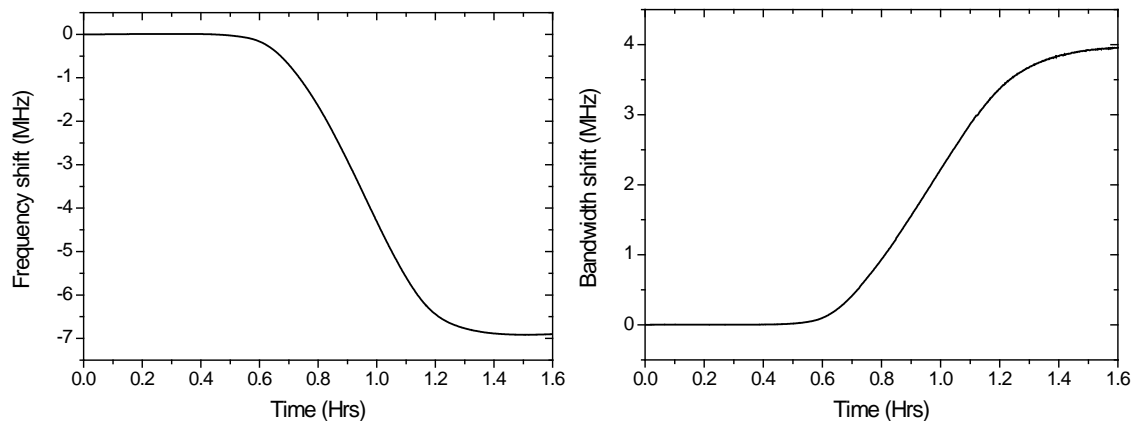
appendix 8.36 – Frequency shift (left) and Bandwidth shift (right) of MOF CPO-27 0.5g of sample under ammonia gas flow of 5cm^3/min.
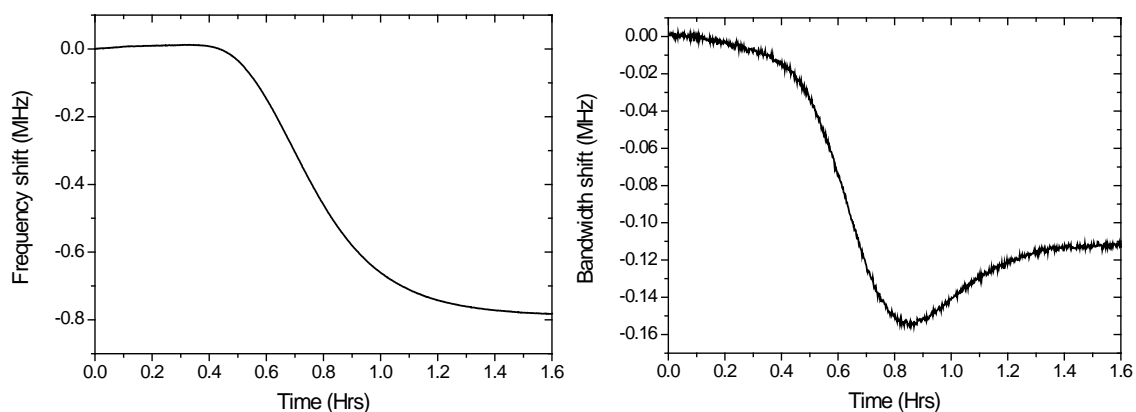
appendix 8.37 – Frequency shift (left) and Bandwidth shift (right) of MOF ZIF-8 0.5g of sample under ammonia gas flow of 5cm^3/min.

8.5 Supplementary mass flow data

8.5.1 Transition metal halides
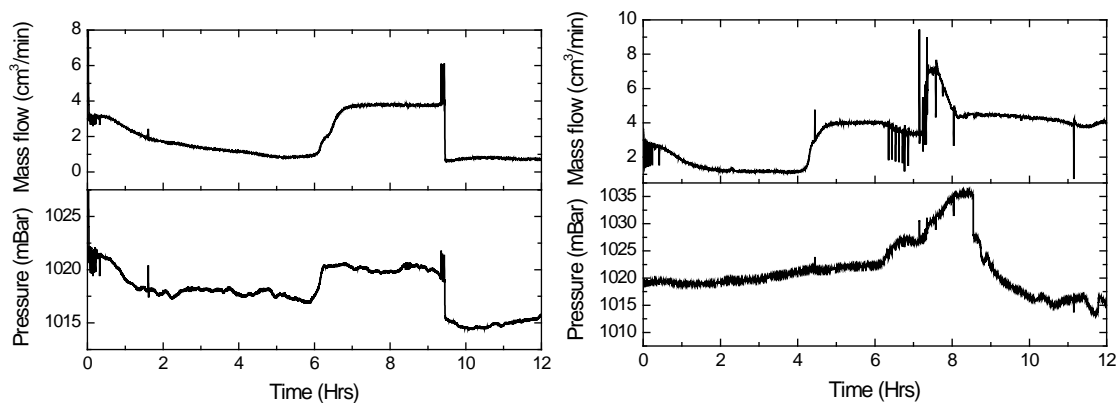
appendix 8.38 – Mass flow and system pressure of CuBr$_2$ (left) and CuI (right) at sample quantity and ammonia gas flow rate of 1.5g and 5cm^3/min.

8.6 Supplementary neutron diffraction results
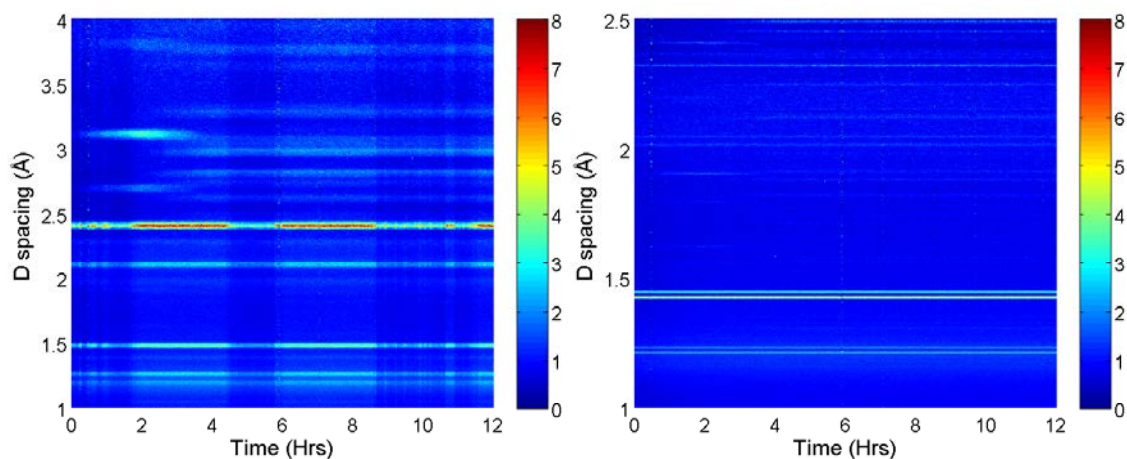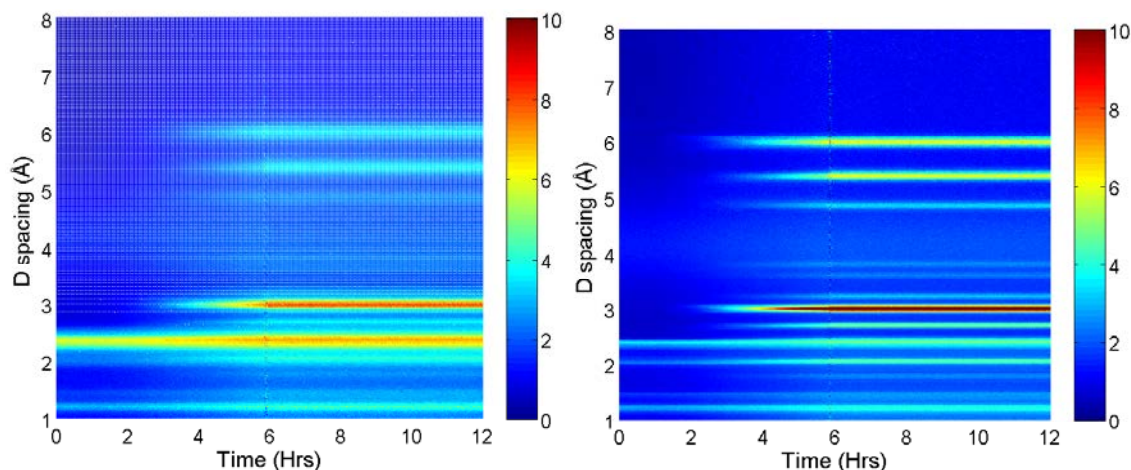
8.6.1 Alkali earth halides
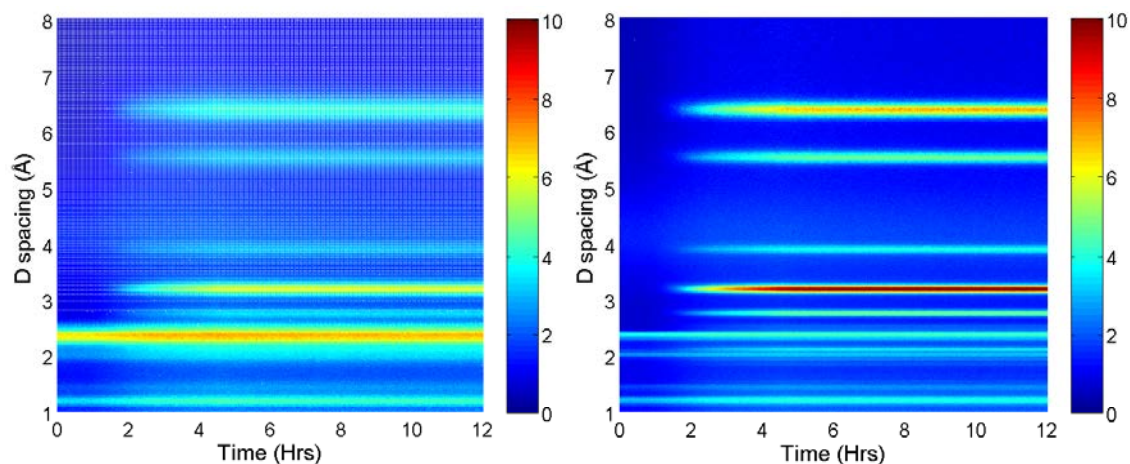
appendix 8.39 – Diffraction peaks from bank 1 (very low angle detectors)(left) and bank 2 (low angle detectors)(right), showing neutron count in colour intensity for MgI$_2$ at sample quantity and ammonia gas flow rate of 1.5g and 5cm^3/min.
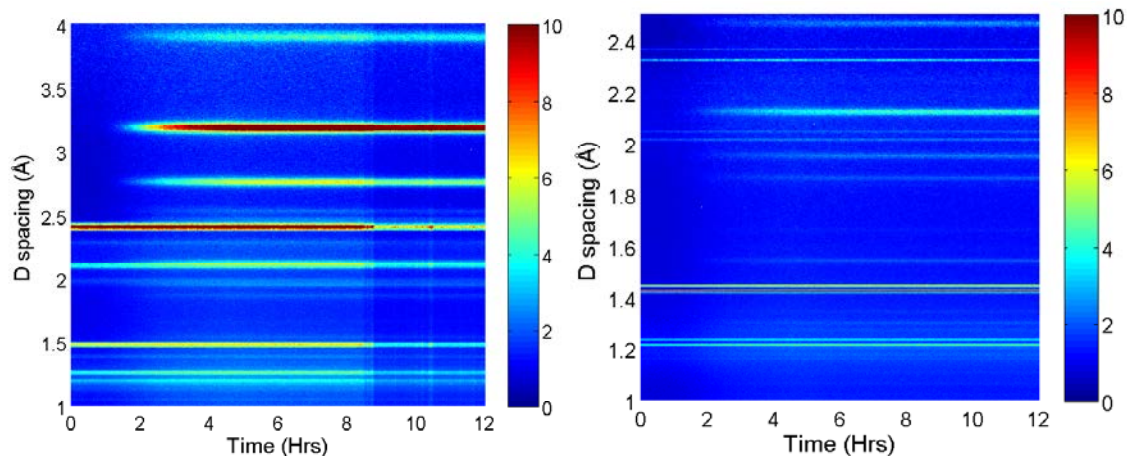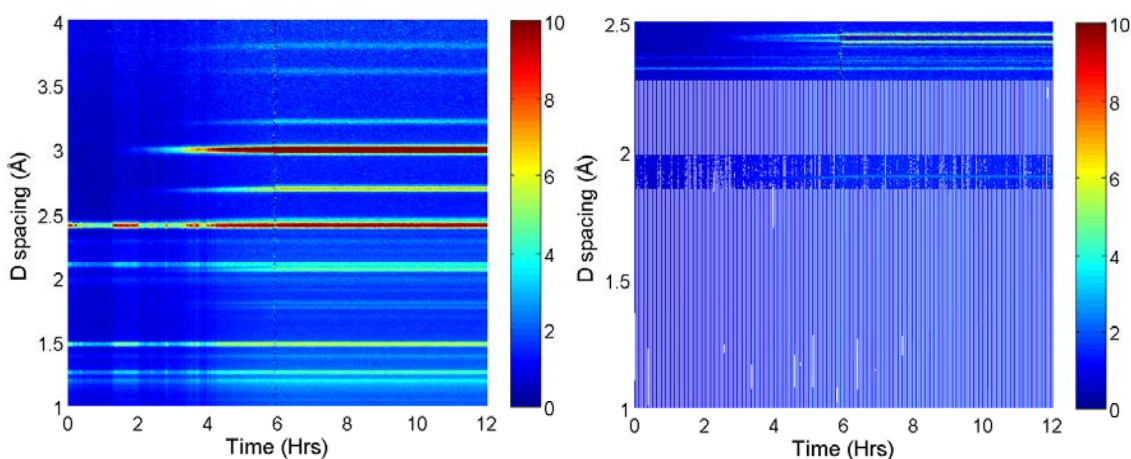
appendix 8.40 – Diffraction peaks from bank 3 (90° detectors)(left) and bank 5 (back scattering detectors)(right), showing neutron count in colour intensity for MgI$_2$ at sample quantity and ammonia gas flow rate of 1.5g and 5cm^3/min.
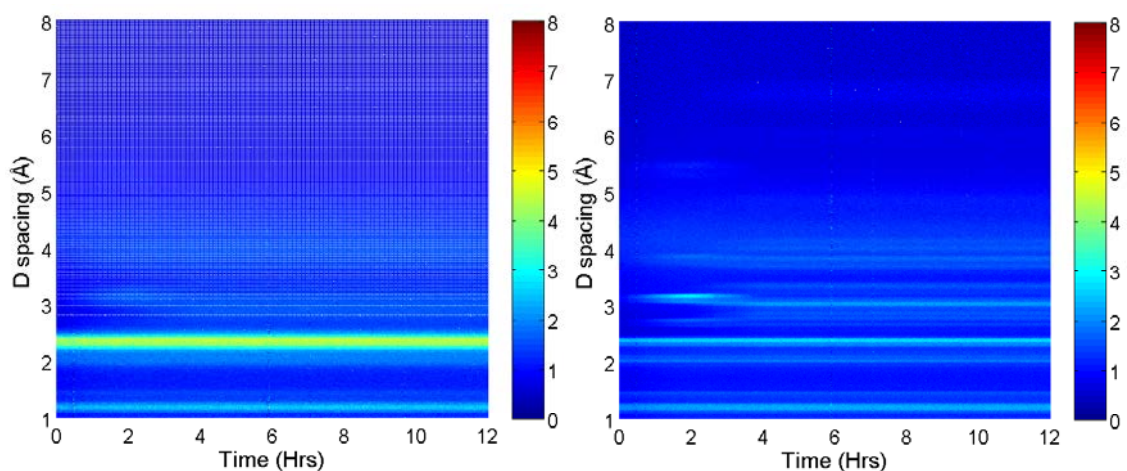
appendix 8.41 – Diffraction peaks from bank 1 (very low angle detectors)(left) and bank 2 (low angle detectors)(right), showing neutron count in colour intensity for CaBr$_2$ at sample quantity and ammonia gas flow rate of 1.5g and 5cm^3/min.

appendix 8.42 – Diffraction peaks from bank 3 (90° detectors)(left) and bank 5 (back scattering detectors)(right), showing neutron count in colour intensity for CaBr$_2$ at sample quantity and ammonia gas flow rate of 1.5g and 5cm^3/min.
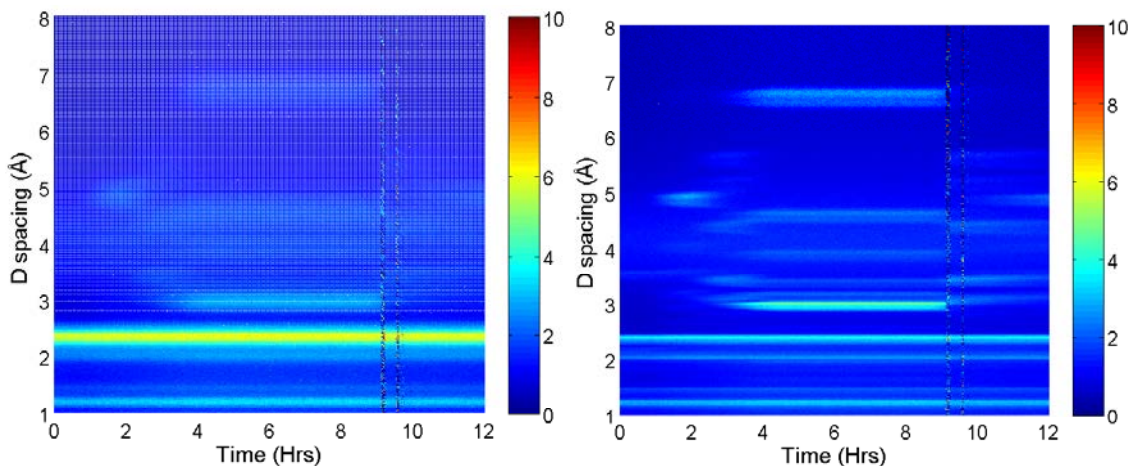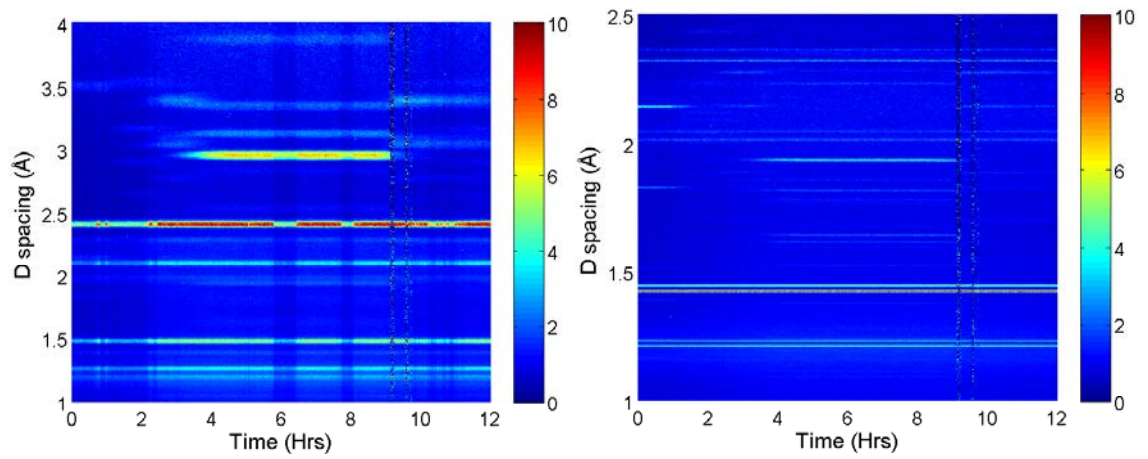
8.6.2   Transition metal halides

appendix 8.43 – Diffraction peaks from bank 1 (very low angle detectors)(left) and bank 2 (low angle detectors)(right), showing neutron count in colour intensity for $CuBr_2$ at sample quantity and ammonia gas flow rate of 1.5g and 5cm^3/min.

appendix 8.44 – Diffraction peaks from bank 3 (90° detectors)(left) and bank 5 (back scattering detectors)(right), showing neutron count in colour intensity for $CuBr_2$ at sample quantity and ammonia gas flow rate of 1.5g and 5cm^3/min.

appendix 8.45 – Diffraction peaks from bank 1 (very low angle detectors)(left) and bank 2 (low angle detectors)(right), showing neutron count in colour intensity for CuI at sample quantity and ammonia gas flow rate of 1.5g and 5cm^3/min.

appendix 8.46 – Diffraction peaks from bank 3 (90° detectors)(left) and bank 5 (back scattering detectors)(right), showing neutron count in colour intensity for CuI at sample quantity and ammonia gas flow rate of 1.5g and 5cm^3/min.